MEMS-enabled reconfigurable reflectarray for terahertz beam steering

Von der Fakultät für Ingenieurwissenschaften,
Abteilung Elektrotechnik und Informationstechnik
der Universität Duisburg-Essen

zur Erlangung des akademischen Grades

Doktor der Ingenieurwissenschaften

genehmigte Dissertation

von

Xuan Liu
aus
Shan Dong

Gutachter: Prof. Dr.-Ing. Andreas Czylwik
Gutachter: Prof. Dr.-Ing. Rolf Jakoby
Tag der mündlichen Prüfung: 24. 05. 2024

DOI: 10.17185/duepublico/82013
URN: urn:nbn:de:hbz:465-20240611-084405-8

PREFACE

In the summer of 2017, I concluded my master thesis at the chair of communication systems (NTS), marking the completion of master's study. Professor Andreas Czylwik offered me a scholarship to participate in the collaborative research center MARIE (Mobile Material Characterization and Localization by Electromagnetic Sensing). Following a year of effort, I transitioned to the role of a research associate, contributing to project S01, focusing on high-speed beamforming concepts for terahertz frequencies.

During the MARIE summer school in 2018, I had the pleasure of meeting Lisa Schmitt, a fellow research associate from project C12, specializing in MEMS technology. Our discussion about potential collaboration and combining the strengths of our projects led to the idea of jointly creating a reconfigurable MEMS-based reflectarray. In our collaborative effort, my role includes the design of the reflectarray configuration, the analysis of its beam steering performance through both analytical calculations and electromagnetic simulations, as well as the measurement of radiation patterns for proof of concept using the reflectarray phantom. This work consists of these design, analysis, and measurement aspects related to the reconfigurable reflectarray.

It is only fair to acknowledge that I could not have completed this work on my own. I would like express my deepest gratitude to my beloved parents, Yang Xiaoling and Liu Zhenhua, for making everything possible for me and making me realize the importance of education. My sincere thanks goes to my supervisor Prof. Andreas Czylwik, for providing me with the opportunity to work at the NTS and pursue a Ph.D. He has shown unwavering belief in me, offering valuable guidance throughout this journey. I

am grateful for the insightful discussions and inspirations. I would like to express the deepest gratitude to Prof. Dr. Rolf Jakoby from the technical University of Darmstadt for his role as the second reviewer of my dissertation. From our discussion regarding the reflectarray, I have gained many new perspectives to the topic. Additionally, I appreciate Prof. Jan C. Balzer for contributing his expertise in terahertz to the chair.

I am delighted to have had the chance to collaborate with colleagues engaged also in research in the terahertz regime, including Bashar, Benedikt, Dilyan, Kevin, Nabil, Thorben, Tim, Vladyslav, Tobias, Sebastian, and Yixiong. I am grateful for the valuable and inspiring discussions and comments we have shared. I would also like to express my appreciation to all the other colleagues outside my research field, who have been friendly and kind to me. Working among them has been a blessing. Thank you to Arife, Alex, Andreas Müller, Barbara, Jessica, Lars, Nahid, Steffan, Thorsten, and Yusuf for contributing to a supportive and welcoming work environment.

I extend a special thank you to my husband, Dennis, who supported me throughout the writing of this thesis and took care of our daughter, allowing me the time to focus on my work. I also express my gratitude to my daughter, Ari. Without her, I believe I would not have completed this so promptly. Her presence made me realize the fleeting nature of time, reminding me to cherish and make use of every moment!

A heartfelt thanks goes to my closest MARIE project partner, Lisa, for engaging in value discussions and fostering a great collaboration. Working together was both easy and enjoyable.

Lastly, I want to express my gratitude to everyone who make MARIE possible. Being part of it allowed me to work on excellent projects, participate in numerous seminars and conferences, an engage in discussions with fellow "MARIErs". Within MARIE, I offer special thanks to Benedikt from C05, Alejandro from C09, Peng from C07, and Andreas from M01. Additionally, I appreciate the support from the FEMIE program for providing personal coaching and all other soft skill seminars!

CONTENTS

CHAPTER

ONE

INTRODUCTION

The terahertz frequency band, which is typically defined as ranging from 0.3 to 10 THz, lies between the microwave and infrared bands. It combines the advantages of these two bands and possesses a unique set of properties that make it advantageous for a variety of applications. One of the key advantages of terahertz waves is their ability to penetrate many optically opaque dielectric materials. This property, combined with its relatively short wavelength, makes it particularly well-suited for imaging applications with fine spatial resolution [38–41]. Additionally, the molecular vibrations of some substances occur within the terahertz band, resulting in distinct spectral fingerprints that can be used for material identification and chemical composition analysis [42].

The advent of coherent terahertz sources and detection techniques facilitated terahertz spectroscopy. As one of the earliest applications in the terahertz regime, terahertz spectroscopy has been utilized to investigate properties of various materials and substances. A common form of terahertz spectroscopy is terahertz time-domain spectroscopy [43,44]. It detects the time function of terahertz radiation passing through the sample under examination, from which the spectral response can be determined by the Fourier transform. Through this process, it is possible to calculate the absorption coefficient and refractive index of the material [45,46], as they can be inferred from the amplitude and phase response, respectively. Furthermore, the amplitude response can

be employed as a tool for the identification and differentiation of substances that possess distinct spectral fingerprints [47, 48]. The vibration frequencies of covalent bonds in organic molecules are located within the terahertz frequency band [49]. When the molecule is illuminated with terahertz radiation of a frequency that corresponds to one of its vibrational modes, the molecule absorbs the energy and the amplitude of the vibration increases, resulting a distinct peak in its absorption spectrum. As the vibration frequencies for different molecules are unique (unique terahertz spectral fingerprints), the identification of some certain substances can be determined by analysing their absorption spectra.

Numerous toxic gases, such as carbon monoxide and ammonia, have unique absorption spectra in the terahertz frequency range [50]. This finding opens up the possibility of utilizing terahertz spectroscopy in a security context: detecting the presence and concentration of toxic gases in the environment such as in landfills, mines, and gas production sites. In addition to the toxic gases, there are other substances of security interest: explosives and illicit drugs possess unique terahertz spectral fingerprints as well [51]. The ability of terahertz radiation to penetrate dry packagings and cloths, makes it possible to detect explosives without opening the package and drugs concealed beneath clothing without the need for physical contact, which is crucial in security applications.

In addition to its applications in spectroscopy, broadband terahertz radiation generated from a terahertz time-domain spectroscopy system can also be utilized for imaging proposes. Images of the sample can be created by changing the location of transmitting and/or receiving antenna with respect to the measured object. A range of applications can benefit from the terahertz imaging technique, such as security scanning for concealed firearms and knives [52], quality control in industrial inspection for impurities or cracks [53, 54], and monitoring of water content in plants to optimize irrigation schedules [56]. The utilization of imaging techniques that are non-destructive and non-invasive in the examination of ancient artwork is crucial in preserving the integrity of artistic collections [55].

Terahertz radiation, characterized by its low photon energy, represents a non-ionizing alternative to X-rays. As a result, it has garnered significant interest in the medical imaging field [57, 58]. Potential applications include the inspection of burned tissues [59], early screening of diabetic foot syndrome [60], monitoring of corneal hydra-

tion [61], and surgical imaging for the purpose of avoiding residual tumors during excision procedures [62].

Another promising field that combines the terahertz technology with biology and medicine is biosensing [63, 64]. So far, there are two approaches to realize terahertz biosensors. The first approach involves the use of a terahertz resonator and is based on the principle of detecting changes in the refractive index of its vicinity due to the introduction of a biomedical medium. This change in refractive index is manifested as a shift in the resonant frequency of the terahertz resonator. The second approach involves the use of microfluidics. In this method, the biomedical medium is injected into a microfluidic chamber and the changes in the terahertz absorption spectrum is observed. Despite both approaches demonstrating high sensitivity in detecting changes in refractive index and absorption spectra within the terahertz range, they are still far from being capable of providing quantifiable conclusions not to mention identifying and differentiating of the type of biological medium [65].

The rapid expansion of wireless communication traffic due to the growth of the mobile data demand and the development of the new applications, such as virtual reality/augmented reality, internet of things, and autonomous driving, results in a substantial increase in the demand for higher data rates and low latency [66]. The terahertz frequency band offers a large bandwidth capacity, providing the availability for the potential deployment of up to terabits per second wireless communication systems [67]. In addition to extensive bandwidth capacity, a terahertz communication system possesses a distinct advantage over a mm-wave communication system in terms of antenna directivity: with the same geometrical size of antenna, the terahertz system exhibits higher directivity, making eavesdropping more challenging and providing a higher degree of security in wireless communication [68].

Compared to its other neighbouring frequency band with shorter wavelength, i.e., infrared, terahertz is less sensitive to adverse weather conditions such as fog and smoke, where the infrared radiation is often scattered [69]. However, there still remain substantial challenges in deploying terahertz wireless communication systems. These include the need for more power efficient and compact terahertz hardware devices, as well as an accurate channel modelling for the terahertz frequency band. These challenges must be addressed in order to fully realize the potential of the terahertz frequency band for wireless communication.

Despite its numerous beneficial properties and potential application scenarios, the terahertz technology is not yet widely used in out-of-laboratory settings and remains largely uncommercialized due to the lack of compact, power-efficient terahertz sources and highly sensitive, low-noise terahertz detectors. In addition, the absence of amplifiers that can directly amplify broadband terahertz signals further exacerbates this issue, limiting its application in practical settings. In response to these challenges, significant efforts are underway to enhance the transmit power and dynamic range of terahertz systems while simultaneously miniaturizing the systems. Additionally, techniques such as beam steering and beamforming, which can improve the system performance, are being extensively researched.

The deployment of beam steering and beamforming techniques can overcome certain drawbacks that terahertz systems face. By utilizing a terahertz antenna array that incorporates multiple synchronized sources, the combined power can be steered in a specific direction, thereby enhancing the terahertz transmit power and improving directivity to counteract free-space loss and high atmospheric absorption. In imaging-related applications, the beam steering network can serve as a replacement for the bulky and slow mechanical scanning devices, enabling a fast and power-efficient terahertz imaging process. In the context of wireless communication and radar systems, the use of an adaptive beam steering network enables the optimization of the radiation pattern of the transmitter or receiver. Given prior knowledge of the target and interferer directions, the adaptive beam steering network can dynamically adjust the directivity to maximize signal strength in the target direction and minimize signal strength in the interferer direction.

Among the various techniques for terahertz beam steering and beamforming [70–72], one approach that involves a reconfigurable terahertz reflectarray stands out. What sets this technique apart is its inherent technological simplicity, as it eliminates the need for a complicated feeding network and associated electronics. Additionally, it is compatible with diverse free space terahertz systems and offers the advantage of a broad beam steering range as well as the ability to operate across a broad frequency spectrum. A typical reconfigurable terahertz reflectarray consists of sub-wavelength reflective elements, each possessing the ability to independently adjust the phase of the local terahertz wave while preserving its amplitude. The relatively short wavelength of terahertz radiation enables spatial phase shifting, facilitated by the actua-

tion of each reflective element. Micro-electromechanical systems (MEMS) offer compact and lightweight actuation systems, allowing a linear motion with displacement of several hundred micrometers that is comparable to the terahertz wavelength.

Within the realm of terahertz beam steering and beamforming techniques, this work studies the MEMS actuation system-enabled reconfigurable terahertz reflectarray, presenting several **contributions to the state of the art**, including

- a mathematical model that can be utilized to determine the radiation pattern of a linear reflectarray composed of sub-wavelength reflective elements that are actuated in a translational movement,
- a design of an approximate blazed grating that is utilized for terahertz beam steering applications with high diffraction efficiency,
- a design of a terahertz reflectarray that leverages the use of a genetic algorithm for continuous beam steering and a customizable radiation pattern, and
- the analysis of the designed reflectarray's bandwidth limitation in the context of communication.

The rest of the work is structured into five chapters. In the second chapter, a comprehensive summary and comparison of the state-of-art terahertz beam steering and beamforming techniques is presented. I highlight their respective advantages and disadvantages, and identify the most suitable application scenario for each technique. The third chapter presents a mathematical model for calculating the radiation pattern of a reflectarray consisting of sub-wavelength actuated reflective elements. An innovative approximate blazed grating structure enabled by a MEMS actuation system is introduced. The benefits of the proposed approximate blazed grating compared to other terahertz reflectarrays are discussed, along with its limitations. Full-wave electromagnetic (EM) simulations and radiation pattern measurements of reflectarray phantoms, i.e., reflectarrays without the MEMS actuation system, are conducted to verify the mathematical model and the beam steering capabilities of the approximate blazed grating.

In order to overcome the limitations associated with the approximate blazed grating,

a new enhanced design of the reflectarray configured by a genetic algorithm (GA) is presented in chapter 4. Single-objective optimizations utilizing a GA implemented in MATLAB are performed. There are three different objectives considered, and they are: maximizing the directivity in a specific direction, minimizing the sidelobe level, and nulling at a designated angle. As the results of the single-objective optimization exhibit a trade-off between the objectives of maximizing the directivity in a desired direction and minimizing the sidelobe level, a multi-objective optimization of these two objectives is carried out. The Pareto front, a representation of the optimal trade-off between the objectives, is obtained as a result of this multi-objective optimization. The analysis of the height profile of the reflectarray configured by a GA reveals its non-perfect periodicity that makes the reflectarray configured by a GA a quasi-grating. Radiation pattern measurements of reflectarray phantoms whose height profiles are determined by a GA are performed. Their measured radiation patterns are then compared with those of the approximate blazed grating phantoms.

In chapter 5, I discuss the bandwidth limitation of the proposed reflectarray designs for accommodating broadband applications, particularly in the realm of communications. Finally, in chapter 6, the future prospects and potential areas of improvement in the field of terahertz reflectarrays are outlined. This work is then brought to a close with a conclusion.

The results of chapter 3 and chapter 4 are published in [1, 3, 8, 10, 16, 30, 33].

CHAPTER

TWO

TERAHERTZ BEAM STEERING AND BEAMFORMING TECHNIQUES

The theoretical concept of phased arrays had already been established in the early years of the 20th century. Decades later, the first experimental demonstration of a phased array deployed in a radar system for military use was achieved [73]. Following this, the field of phased array-assisted beam steering and beamforming experienced rapid growth and development. A phased array consists of multiple array elements that can be organized in a line to form a linear array, or spread out in a plane to form a planar array. Through the assignment of specific phases and amplitudes to these elements, the radiated waves from all elements can be combined to produce a superposition in the far field that interferes constructively in the direction of the target, thus reinforcing the signal, and destructively in other directions, effectively mitigating interference. As a result, a phased array antenna has a greater directivity compared to an antenna that only has a single element. The deployment of electronically tunable phase shifters and amplifiers allows for dynamic tuning of the phase and amplitude distribution of the phased array, enabling an electronic beam steering network.

So far, beam steering techniques and technologies at microwave frequencies have been well-established and widely commercialized. A direct deployment of these techniques to terahertz frequencies still remains a significant challenge, due to the absence of es-

sential electronics that operate directly at terahertz frequencies. Therefore, it is necessary to adapt the existing beam steering techniques in order to make terahertz beam steering work. In this chapter, I summarize the terahertz beam steering and beamforming techniques and categorize them into five classes: phased array, leaky wave antenna, spatial modulation in the optical domain, free space-coupled terahertz beam steering and beamforming devices, and terahertz reflectarray. For each class, I describe the underlying principle and provide an overview of relevant research results, with a focus on comparison and evaluation of the different approaches.

2.1 Terahertz phased array

Phased arrays are widely used for beam steering at radio frequencies and usually are composed of three essential building blocks: array elements, feeding network, and phase shifters (or time delay elements). The waveguide-based feeding network employs splitters (couplers) and waveguides to create different branches that connect to the array elements. Each branch includes a phase shifter, which is used to adjust the phase of the signal reaching the corresponding array element. While much progress has been made in research on terahertz technology, the development of discrete terahertz components such as phase shifters, splitters (couplers), and waveguides is still in its infancy, making the realization of an integrated terahertz phased array challenging.

Researchers have been working for several decades to bridge the terahertz gap by advancing both the electrical and optical approaches. They have laid groundwork for generating terahertz signals electronically and optoelectronically. These terahertz generation methods offer the possibility of implementing a feeding network and phase shifters (time delay elements) at microwave frequencies and at optical frequencies, respectively, before the up-conversion and down-conversion stages. They require no breakthrough in terahertz technology and can accelerate the development of terahertz beam steering techniques by taking advantage of existing technology.

In this section, firstly, I will consider electronic terahertz systems and discuss the common phased array architectures that can be implemented in such systems, along with their corresponding working principles. Additionally, a literature review of relevant research will be presented. The second subsection will focus on the optoelectronic terahertz systems. Similar to the first subsection, I will introduce the common phased

array architectures for such systems and explain their underlying principles.

2.1.1 Phased array for electronic terahertz systems

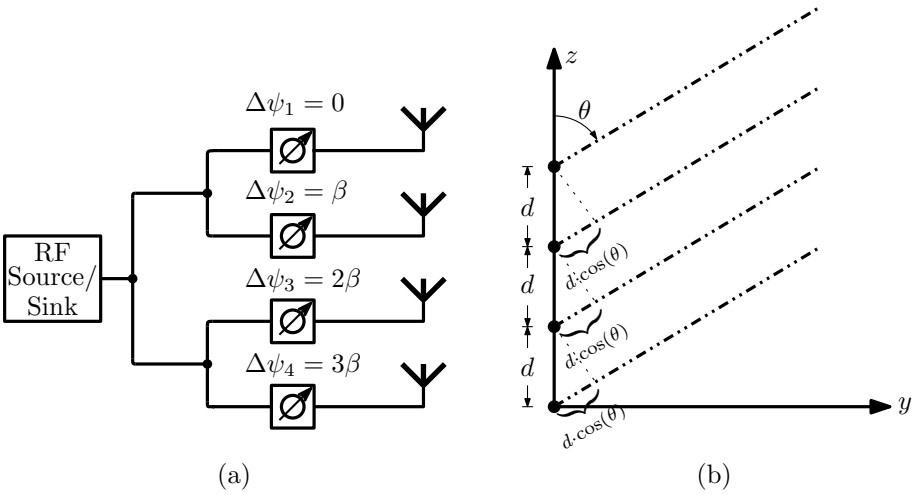

Figure 2.1: (a) Simplified block diagram of a 4-element phased array with a corporate feed. (b) Geometry of a 4-element array of sources positioned along the z-axis.

In order to gain an understanding of the operating principle of a phased array, a simple example is presented. Fig. 2.1 (a) depicts an analog beam steering network at radio frequency (RF) for a 4-element array with a corporate feed. This network enables the signal to be transmitted or received by all four elements, which are connected to a single RF source or sink depending on the system state. The corporate feed is also known as an equal path-length waveguide branching network, which ensures that the feeding network contributes no phase difference to the array elements. Instead, the phase shifters on each branch are solely responsible for adjusting the phase distribution of the array. A geometry model of the 4-element array is illustrated in Fig. 2.1(b).

The array factor $\mathrm{AF}_{\text{4-element}}$ of the uniform 4-element array is:

$$\mathrm{AF}_{\text{4-element}} = 1 + \mathrm{e}^{+\mathrm{j}(k\cdot d\cdot\cos(\theta)+\beta)} + \mathrm{e}^{+\mathrm{j}2(k\cdot d\cdot\cos(\theta)+\beta)} + \mathrm{e}^{+\mathrm{j}3(k\cdot d\cdot\cos(\theta)+\beta)}, \tag{2.1}$$

where k is the wave number in free space, d and β are the distance and phase difference between adjacent elements in the array, respectively.

The amplitude of the total field of the array at $\theta = \theta_0$ is maximized when:

$$k \cdot d \cdot \cos(\theta)\,|_{\theta=\theta_0} + \beta = 0, \tag{2.2}$$

holds.

The beam is adjusted to a given angle θ_0 by setting the phase difference β between adjacent elements to a predetermined value

$$\beta = -k \cdot d \cdot \cos(\theta)\,|_{\theta=\theta_0}. \tag{2.3}$$

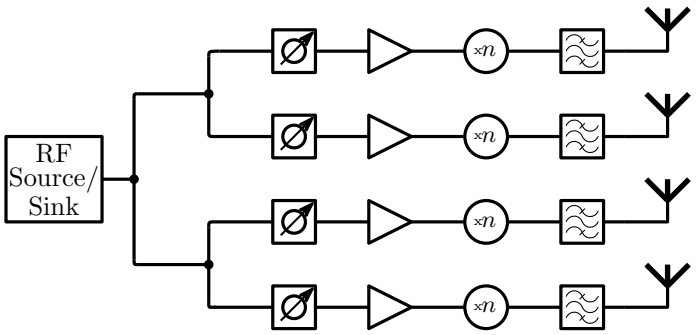

Figure 2.2: Simplified block diagram of a 4-element terahertz phased array with a corporate feed.

Fig. 2.2 illustrates the implementation of a terahertz beam steering network by expanding the RF beam steering network with a frequency multiplier in each branch.

To investigate the required phase difference between the adjacent branches for steering the main beam in a desired direction, I will consider here the use of a frequency doubler as the simplest frequency multiplier. The RF signal at the input of the frequency doubler in the n-th branch is given by

$$x_{\mathrm{RF},n}(t) = A_1 \cdot \cos(\omega_{\mathrm{RF}} \cdot t + \varphi_n). \tag{2.4}$$

The signal at the output of the frequency doubler that has a square characteristic is

$$x_{\mathrm{THz},n}(t) = k \cdot x_{\mathrm{RF},n}^2(t) = k \cdot \frac{A_1^2}{2}\left(\cos(2\omega_{\mathrm{RF}} + 2\varphi_n) + 1\right), \tag{2.5}$$

where k is a constant.

Eq. 2.5 reveals that both frequency and phase components are doubled. As a result, setting the phase difference β between adjacent elements to $\varphi_n - \varphi_{n-1} = \frac{-k \cdot d \cdot \cos(\theta)\,|_{\theta=\theta_0}}{2}$ is sufficient to steer the beam to the desired angle θ_0.

The RF - terahertz chain, as depicted in Fig. 2.2, adopts a partitioned approach which separates the terahertz generation, i.e., amplification, multiplication, and filtering, from terahertz radiation via an antenna. However, this block-by-block approach leads to low DC - to - radiated terahertz power conversion efficiency. To address this issue, Sengupta et al. proposed a terahertz power generation and beam steering array based on distributed active radiators [74]. This approach combines terahertz generation and radiation into a single process, thereby replacing the conventional partitioned approach. Phase shifting is typically achieved by employing a weighted summation of the quadrature signals, where combining the quadrature signal I and Q with a specific magnitude allows for arbitrary phase shifting to be achieved [74].

In addition to the corporate feeding network, phased arrays can also be achieved through coherent power-combing of multiple sources, such as coupled oscillating elements. The self-sustained oscillating elements can be synchronized to the adjacent elements via various coupling mechanisms. Tousi and Afshari proposed a scalable terahertz 2D phased array of oscillating elements which are connected to their adjacent elements both horizontally and vertically using phase shifters [75]. In contrast, Sengupta and Hajimiri utilize near field sensors to synchronize the oscillating elements in the phased array [76]. In this method, phase control is achieved by modifying the free-running oscillation frequency of each element with varactors in the resonator, allowing for beam steering without phase shifters.

2.1.2 Phased array for a fiber-coupled optoelectronic terahertz system

Considerable efforts have been devoted to bridge the terahertz gap from the optical side. Terahertz generation through optoelectronic means offers many advantages, including a broad bandwidth of several terahertz and high dynamic range, making it ideal for spectroscopy and imaging applications. This subsection will begin with describing an optoelectronically generated continuous-wave (cw) terahertz system, followed by an introduction to various phased array architectures that can be incorporated into such a system.

As illustrated in Fig. 2.3, two cw laser signals whose electric fields are denoted as $E_1(t) = A_1 e^{j(\omega_1 t+\varphi_1)}$ and $E_2(t)) = A_2 e^{j(\omega_2 t+\varphi_2)}$, respectively, operate in the infrared range with slightly different center frequencies. An optical coupler combines these two signals, resulting in a beat signal $E_3(t)$ whose envelope has a frequency equal to the difference frequency between the two laser signals. The envelope of the beat signal is detected and radiated into free space using a antenna-integrated photomixer, which can be a photodiode or photoconductor.

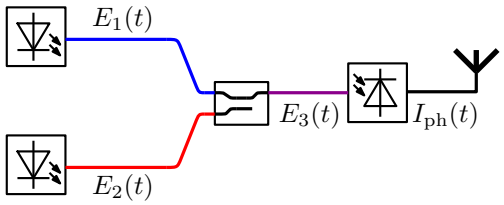

Figure 2.3: Simplified block diagram for terahertz generation by photomixing.

The photocurrent generated by the photomixer $I_{\mathrm{photo}}(t)$ is proportional to the instantaneous optical power of the beat signal $E_3(t)$, i.e.,

$$\begin{aligned} I_{\mathrm{photo}}(t) \propto |E_3(t)|^2 &= E_3(t) \cdot E_3^*(t) \\ &= \left(A_1 e^{j(\omega_1 t+\varphi_1)} + A_2 e^{j(\omega_2 t+\varphi_2)}\right) \cdot \left(A_1 e^{-j(\omega_1 t+\varphi_1)} + A_2 e^{-j(\omega_2 t+\varphi_2)}\right) \\ &= A_1^2 + A_2^2 + A_1 A_2 \cdot e^{j((\omega_1-\omega_2)t+(\varphi_1-\varphi_2))} + A_1 A_2 \cdot e^{-j((\omega_1-\omega_2)t+(\varphi_1-\varphi_2))} \\ &= A_1^2 + A_2^2 + 2A_1 A_2 \cdot \cos\left((\omega_1 - \omega_2)\, t + (\varphi_1 - \varphi_2)\right). \end{aligned} \tag{2.6}$$

It contains a frequency component with the frequency of $\omega_1 - \omega_2$ with the phase of $\varphi_1 - \varphi_2$.

When a corporate feed is introduced after the optical coupler as shown in Fig. 2.4, the phase shifter in each branch adjusts the phases of both laser signals simultaneously by the same amount $\Delta\psi$, which gives:

$$\begin{aligned} E'_{3,\mathrm{b1}}(t) &= A_1 e^{j(\omega_1 t+\varphi_1+\Delta\psi_1)} + A_2 e^{j(\omega_2 t+\varphi_2+\Delta\psi_1)}, \\ E'_{3,\mathrm{b2}}(t) &= A_1 e^{j(\omega_1 t+\varphi_1+\Delta\psi_2)} + A_2 e^{j(\omega_2 t+\varphi_2+\Delta\psi_2)}. \end{aligned} \tag{2.7}$$

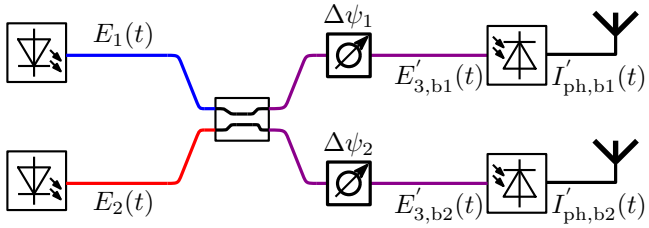

Figure 2.4: Simplified block diagram for a two-element terahertz phased array utilizing optical phase shifters after the combination of two laser signals.

After photomixing, the photocurrents in the upper and lower branches are:

$$
\begin{aligned}
I'_{\mathrm{ph,b1}}(t) \propto |E'_{3,\mathrm{b1}}(t)|^2 &= E'_{3,\mathrm{b1}}(t) \cdot E'^{*}_{3,\mathrm{b1}}(t) \\
&= \left(A_1 \mathrm{e}^{\mathrm{j}(\omega_1 t+\varphi_1+\Delta\psi_1)} + A_2 \mathrm{e}^{\mathrm{j}(\omega_2 t+\varphi_2+\Delta\psi_1)}\right) \\
&\cdot \left(A_1 \mathrm{e}^{-\mathrm{j}(\omega_1 t+\varphi_1+\Delta\psi_1)} + A_2 \mathrm{e}^{-\mathrm{j}(\omega_2 t+\varphi_2+\Delta\psi_1)}\right) \\
&= A_1^2 + A_2^2 + A_1 A_2 \cdot \mathrm{e}^{\mathrm{j}((\omega_1-\omega_2)t+((\varphi_1+\Delta\psi_1)-(\varphi_2+\Delta\psi_1)))} \\
&+ A_1 A_2 \cdot \mathrm{e}^{-\mathrm{j}((\omega_1-\omega_2)t+((\varphi_1+\Delta\psi_1)-(\varphi_2+\Delta\psi_1)))} \\
&= A_1^2 + A_2^2 + 2A_1 A_2 \cdot \cos\left((\omega_1-\omega_2)\,t + (\varphi_1-\varphi_2)\right), \\
I'_{\mathrm{ph,b2}}(t) \propto |E'_{3,\mathrm{b2}}(t)|^2 &= E'_{3,\mathrm{b2}}(t) \cdot E'^{*}_{3,\mathrm{b2}}(t) \\
&= \left(A_1 \mathrm{e}^{\mathrm{j}(\omega_1 t+\varphi_1+\Delta\psi_2)} + A_2 \mathrm{e}^{\mathrm{j}(\omega_2 t+\varphi_2+\Delta\psi_2)}\right) \\
&\cdot \left(A_1 \mathrm{e}^{-\mathrm{j}(\omega_1 t+\varphi_1+\Delta\psi_2)} + A_2 \mathrm{e}^{-\mathrm{j}(\omega_2 t+\varphi_2+\Delta\psi_2)}\right) \\
&= A_1^2 + A_2^2 + A_1 A_2 \cdot \mathrm{e}^{\mathrm{j}((\omega_1-\omega_2)t+((\varphi_1+\Delta\psi_2)-(\varphi_2+\Delta\psi_2)))} \\
&+ A_1 A_2 \cdot \mathrm{e}^{-\mathrm{j}((\omega_1-\omega_2)t+((\varphi_1+\Delta\psi_2)-(\varphi_2+\Delta\psi_2)))} \\
&= A_1^2 + A_2^2 + 2A_1 A_2 \cdot \cos\left((\omega_1-\omega_2)\,t + (\varphi_1-\varphi_2)\right).
\end{aligned}
\tag{2.8}
$$

As shown in Eq. 2.8, the resulting terahertz signals in the upper and lower branches are identical, i.e., there is no phase difference between the two elements.

In order to tune the phase of the terahertz signal in each branch independently, it is necessary to adjust the phase of one laser signal prior to its combination with the other laser signal. Fig. 2.5 illustrates a 2-element phased array, where the resulting terahertz phases in the upper and lower branches are $\varphi_1 + \Delta\psi_1 - \varphi_2$ and $\varphi_1 + \Delta\psi_2 - \varphi_2$, respectively, leading to a phase difference of $\Delta\psi_1 - \Delta\psi_2$ between the two elements.

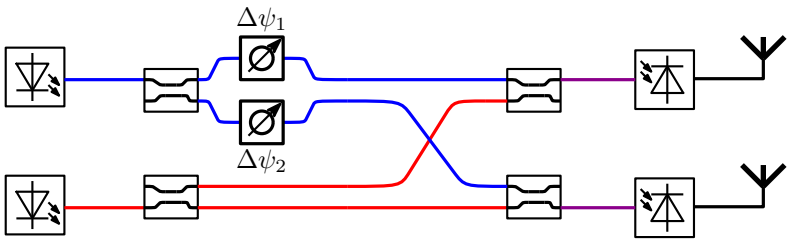

Figure 2.5: Simplified block diagram for a two-element terahertz phased array utilizing optical phase shifters prior to the combination of two laser signals.

In the work of Ming Che et al., they designed and fabricated a 2x8 optical phased array network, achieving a continuous beam steering in a range of 50° at 300 GHz [77]. The same research group has also investigated the possibility of building a terahertz phased array without the phase shifters. They have demonstrated a phased array by utilizing the chromatic dispersion of optical fibers [78]. The phase shifting is achieved by shifting the center frequencies of the laser signals while keeping the difference frequency constant. By inserting a chromatic dispersive device in one branch, the phase difference between two branches can be then achieved.

In addition to phase shifters, optical delay units (ODU) can also be employed to independently time delay the beat signal in each branch. In this way, we can introduce the corporate feed network after the two laser signals are combined. This approach provides the advantage of achieving broadband beam steering without experiencing the phenomenon of the main beam's direction shifts as the frequency changes. This phenomenon, known as beam squint, is often encountered in the phase-shifting-based beam steering networks.

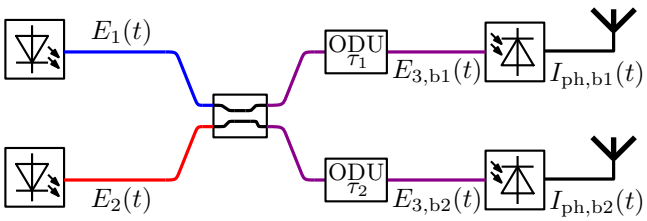

Figure 2.6: Simplified block diagram for a two-element terahertz phased array utilizing ODUs.

Let us take a look at the phased array system that employs ODUs with the simplest corporate feed, illustrated in Fig. 2.6. The array, consisting of two elements, introduces

delays of τ_1 and τ_2 to the beat signal in the upper and lower branch, respectively. The electric field of the beat signal in the upper branch $E_{3,\mathrm{b1}}(t)$ after passing through the ODU is:

$$E_{3,\mathrm{b1}}(t) = A_1 \mathrm{e}^{\mathrm{j}(\omega_1(t-\tau_1)+\varphi_1)} + A_2 \mathrm{e}^{\mathrm{j}(\omega_2(t-\tau_1)+\varphi_2)}. \tag{2.9}$$

The photocurrent generated by the photomixer 1 is then:

$$\begin{aligned} I_{\mathrm{photo,b1}}(t) \propto |E_{3,\mathrm{b1}}(t)|^2 &= E_{3,\mathrm{b1}}(t) \cdot E^*_{3,\mathrm{b1}}(t) \\ &= \left(A_1 \mathrm{e}^{\mathrm{j}(\omega_1(t-\tau_1)+\varphi_1)} + A_2 \mathrm{e}^{\mathrm{j}(\omega_2(t-\tau_1)+\varphi_2)}\right) \\ &\cdot \left(A_1 \mathrm{e}^{-\mathrm{j}(\omega_1(t-\tau_1)+\varphi_1)} + A_2 \mathrm{e}^{-\mathrm{j}(\omega_2(t-\tau_1)+\varphi_2)}\right) \\ &= A_1^2 + A_2^2 + 2A_1A_2 \cdot \cos\left(\omega_{\mathrm{THz}} t + (\varphi_1 - \varphi_2) - \omega_{\mathrm{THz}}\tau_1\right) \end{aligned} \tag{2.10}$$

Similarly, the electric field of the beat signal in the lower branch $E_{3,\mathrm{b2}}(t)$ after passing through the ODU is:

$$E_{3,\mathrm{b2}}(t) = A_1 \mathrm{e}^{\mathrm{j}(\omega_1(t-\tau_2)+\varphi_1)} + A_2 \mathrm{e}^{\mathrm{j}(\omega_2(t-\tau_2)+\varphi_2)}. \tag{2.11}$$

The photocurrent generated by the photomixer 2 is then:

$$\begin{aligned} I_{\mathrm{photo,b2}}(t) \propto |E_{3,\mathrm{b2}}(t)|^2 &= E_{3,\mathrm{b2}}(t) \cdot E^*_{3,\mathrm{b2}}(t) \\ &= A_1^2 + A_2^2 + 2A_1A_2 \cdot \cos\left(\omega_{\mathrm{THz}} t + (\varphi_1 - \varphi_2) - \omega_{\mathrm{THz}}\tau_2\right). \end{aligned} \tag{2.12}$$

The phase difference between the array elements is

$$\beta = -\omega_{\mathrm{THz}}\left(\tau_1 - \tau_2\right). \tag{2.13}$$

According to Eq 2.3, the superposition of the electrical fields of both elements is maximized in the direction of θ_0 in the far field when the phase difference is set to:

$$\beta = -k \cdot d \cdot \cos\left(\theta_0\right) = -\frac{\omega_{\mathrm{THz}}}{c_0} \cdot d \cdot \cos\left(\theta_0\right). \tag{2.14}$$

A comparison between Eq. 2.13 and Eq. 2.14 reveals that if the delay difference between the two elements is maintained at $\tau_1 - \tau_2 = \frac{d}{c_0} \cdot \cos\left(\theta_0\right)$, the main beam will always point towards θ_0 regardless of the terahertz frequency. In contrast to phased arrays that utilize phase shifters, the use of true time delay elements permits broadband beam steering without any beam squint effects.

2.2 Leaky wave antenna

This section explores another system that can be used for terahertz beam steering, known as the leaky wave antenna. In contrast to phased arrays, it requires neither a complex feeding network nor the phase shifters. Instead, it usually consists of a transmission line or waveguide and radiating unit cells placed periodically along the guided-wave propagation direction. The phase difference $\Delta\psi$ between adjacent cells arises as the wave passes through the unit cells subsequently:

$$\Delta\psi = \beta \cdot l, \tag{2.15}$$

where β is the propagation constant of the wave inside a waveguide or in a transmission line and l is the distance between the adjacent cells.

As the propagation constant β of the propagating wave is frequency-dependent, the phase difference $\Delta\psi$ between adjacent cells can thus be tuned by changing the frequency of the propagating wave. This gives the travelling-wave antenna an inherent property of beam steering with frequency sweeping. This section presents the working principle and a literature research on two types of leaky wave antennas: uniform leaky wave antenna and periodic leaky wave antenna.

2.2.1 Uniform leaky wave antenna

The very first uniform leaky wave antenna is created by simply cutting a long and uniform slot into the narrow wall of an air-filled metallic rectangular waveguide as shown in Fig 2.7(a) [79].

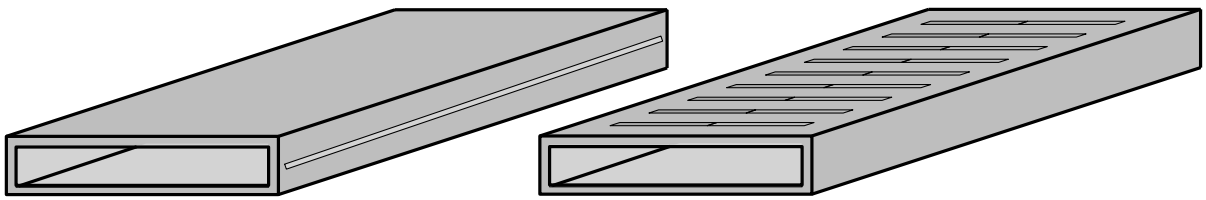

(a) (b)

Figure 2.7: Illustration of a rectangular waveguide-based (a) uniform leaky wave antenna and (b) quasi-uniform leaky wave antenna with transversely oriented slots.

The propagation constant β for the propagating mode in a closed rectangular waveguide is given by:

$$\beta = \sqrt{k_0^2 - k_c^2}, \tag{2.16}$$

where k_0 is the wave number in free space and k_c is the cut-off wave number. For an operating frequency above the cut-off frequency, the phase constant β is real and less than the wave number in free space k_0, resulting in a phase velocity $v_{ph} = \frac{\omega}{\beta}$ that is faster than in free space. This leads to the propagation of a fast wave, known as the radiating wave, within the rectangular waveguide. When an opening, such as a slot, is introduced into the waveguide, the radiating wave is able to pass into free space.

In practice, a quasi-uniform leaky wave antenna is often employed for beam steering applications. Its structure is illustrated in Fig. 2.7(b). This antenna configuration resembles an antenna array, with slots arranged periodically along the propagation direction, forming a uniform array with a progressively increasing phase profile. To prevent grating lobes, the adjacent slots should be placed next to each other with a separation distance no greater than half of the wavelength in free space. The maximum resulting phase difference between the adjacent unit cells $\Delta\psi$ can be calculated by taking into account that the phase constant in the rectangular waveguide β is smaller than the phase constant in free space k_0

$$\Delta\psi = \beta l < k_0 l \Rightarrow \psi < \frac{2\pi}{\lambda_0} \cdot \frac{\lambda_0}{2} \Rightarrow \Delta\psi < \pi. \tag{2.17}$$

The calculation reveals a drawback of using a quasi-uniform LWA implemented with a straight rectangular waveguide for beam steering: only forward-radiation is possible. The phase profile of the array always increases within the unambiguous phase range along the propagation direction, preventing a back-radiation. Moreover, the phase difference between the adjacent slots is insufficient to achieve a broadside radiation that requires a phase difference of $2n\pi,\ n \in \mathbb{Z}$.

To overcome this drawback, Sarabandi et al. have demonstrated a meandered waveguide structure that extends the propagation length l while keeping the distance between the adjacent radiating cells small [80]. This structure enables broadside radiation, reduces the required frequency sweep range for the same beam steering range, and achieves e.g. a 3.3°/GHz steering over a 50° scan angle at the Y-Band.

Another approach for achieving a broad beam steering range with a small fractional frequency bandwidth is to introduce a corrugation on the inner bottom of the rectangular waveguide, as shown by L. Ranzani et al. [81]. This approach achieved a 2°/GHz steering over a 40° scan angle at the G-Band.

1D slotted LWAs exhibit large electrical dimensions in the steering plane, and appropriately sized slots can produce a moderately narrow beam width in this plane. In contrast, the antenna has a small electrical dimension in the plane orthogonal to the steering plane, resulting in a fan-shaped 3D beam characteristic, which leads to suboptimal directivity, spatial ambiguity, and limited spatial resolution. To address these limitations, researchers have endeavoured to narrow the 3D beam width by converting 1D LWAs into 2D LWAs.

An effort by Sarabandi et al. involved placing patch antennas along a meandered waveguide to create a two-dimensional antenna array [80]. The E-type waveguide node couples power from the waveguide to a central patch above it, which is connected in series to other patches on either side via high-impedance transmission lines. In order to maintain the beam direction of the 1D leaky antenna while achieving a narrow beam width, all patch elements must be excited in-phase. A planar array was constructed by Ranzani and colleagues by feeding multiple slotted leaky wave antennas using a corporate feed network [81]. Both methods were successful in narrowing the beam width to 10°.

2.2.2 Periodic leaky wave antenna

As the operating frequency increases, the use of the metallic rectangular waveguides becomes impractical due to manufacturing difficulties and high conductor losses. Instead, open waveguides, such as dielectric waveguides or microstrip, are preferred for terahertz applications. Open waveguides often feature a dielectric substrate that confines a major portion of the wave, resulting in a propagating wave with a phase constant larger than its phase constant in free space. This leads to the propagation of a slow wave in open waveguides, also known as a non-radiating wave. However, by introducing discontinuities along the wave propagation axis, the slow wave can be converted into a radiating wave that can propagate into free space.

Fig. 2.8 shows a terahertz microstrip transmission line based periodic leaky wave an-

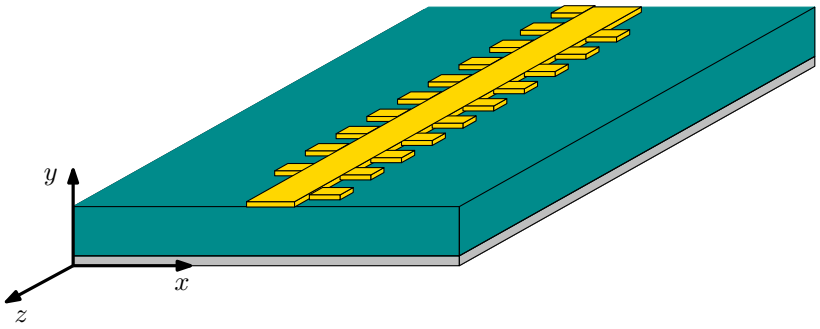

Figure 2.8: Illustration of a microstrip-based periodic leaky wave antenna.

tenna. The periodic rectangular stubs located along the top conductor of the microstrip, aligned with the wave propagation axis ($z-$axis), introduces spatial periodicity, making the transmission line a periodic structure. The distance between adjacent rectangular stubs is denoted as d. According to the Floquet-Bloch theorem, the electric field in such a periodic structure can be expressed as the product of a periodic function and an exponential function:

$$\mathbf{E}\left(x,y,z\right) = \mathbf{E}_{\text{periodic}}\left(x,y,z\right) \cdot \mathrm{e}^{\mathrm{j}\beta_0 z}, \tag{2.18}$$

where β_0 represents the propagation constant of the fundamental mode on the transmission line.

Furthermore, the periodic function $\mathbf{E}_{\text{periodic}}\left(x,y,z\right)$ can be expanded using its Fourier series representation:

$$\mathbf{E}_{\text{periodic}}\left(x,y,z\right) = \sum_{n=-\infty}^{\infty} \mathbf{E}_n\left(x,y\right) \cdot \mathrm{e}^{\mathrm{j}\frac{2\pi n z}{d}}. \tag{2.19}$$

Substituting this expression into Eq. 2.18, we obtain:

$$\begin{aligned} \mathbf{E}\left(x,y,z\right) &= \sum_{n=-\infty}^{\infty} \mathbf{E}_n\left(x,y\right) \cdot \mathrm{e}^{\mathrm{j}\frac{2\pi n z}{d}} \cdot \mathrm{e}^{\mathrm{j}\beta_0 z} \\ &= \sum_{n=-\infty}^{\infty} \mathbf{E}_n\left(x,y\right) \cdot \mathrm{e}^{\mathrm{j}\left(\frac{2\pi n}{d}+\beta_0\right) z} \\ &= \sum_{n=-\infty}^{\infty} \mathbf{E}_n\left(x,y\right) \cdot \mathrm{e}^{\mathrm{j}\beta_n z}. \end{aligned} \tag{2.20}$$

Here, $\mathbf{E}_n\left(x,y\right) \cdot \mathrm{e}^{\mathrm{j}\beta_n z}$ represents the field of n-th-order space harmonic wave, characterized by its field distribution $\mathbf{E}_n\left(x,y\right)$ on the transversal plane and its propagation

constant $\beta_n = \beta_0 + \frac{2\pi n}{d}$.

As observed in Eq. 2.20, by introducing the periodicity into the transmission line, an infinite numbers of the space harmonic waves are excited, including both fast and slow waves [82]. To ensure a single beam radiation of the leaky wave antenna, the periodic leaky wave antenna is designed so that the first space harmonic wave (negative first order) is fast. Its wave number is given by $\beta_{-1} = \beta_0 - \frac{2\pi}{d}$. As the operating frequency changes, the wave number β_{-1} can be negative, zero, or positive, which allows the beam to point in the backward, broadside, or forward direction.

Murano et al. successfully demonstrated a microstrip-based terahertz leaky wave antenna capable of covering a steering range from -23° to 15° by tuning the frequency from 235 GHz to 325 GHz [83]. This particular leaky wave antenna is equipped with two waveguide ports, allowing coupling of the wave from a discrete source to the leaky wave antenna and facilitating coupling out from the leaky wave antenna to a discrete detector. Lu et al. present a novel design that monolithically integrates the microstrip-based leaky wave antenna with a photodiode to create a steerable terahertz transmitter [84]. By sweeping the frequency from 230 GHz to 330 GHz, the transmitter achieves a steering from -46° (backward) to 42° (forward). The realized gain and 3 dB beam width of the periodic leaky wave antenna are approximately 11 dBi and 10°, respectively.

2.3 Beam steering technique incorporated in a free-space optoelectronic terahertz system

In Section 2.1.2, a phased array incorporated in a fiber-coupled optoelectronic terahertz system is described. The phase of the terahertz signal at each antenna element is tuned by shifting the phase of one of the laser signals used for photomixing, which requires a waveguide-based corporate feeding network and an optical phase shifter per element. For a free-space optoelectronic terahertz system, an analogous approach to the use of phase shifters is to spatially modulate the phase of the laser signal. In this section, I first briefly describe a free-space optoelectronic terahertz system, which provides a useful context for understanding the approach to be discussed. This is followed by a discussion of a terahertz beam steering technique that utilizes spatial phase modulation of

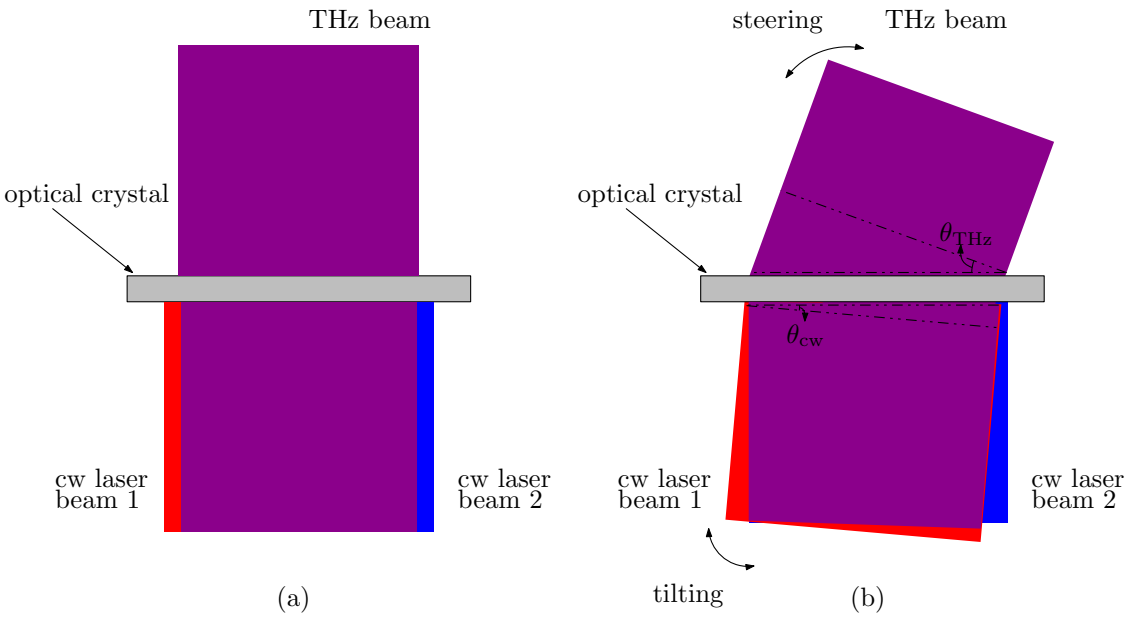

Figure 2.9: Illustration of (a) generating terahertz radiation by two cw lasers illuminating an optical crystal and (b) steering the terahertz beam by tilting one of the cw laser sources [85].

the laser signal. Finally, I summarize the relevant research results.

Fig. 2.9(a) illustrates the process of generating cw terahertz radiation through the optical process of difference-frequency generation, which is achieved by illuminating a nonlinear optical crystal with two cw lasers with slightly different center frequencies.

Let the instantaneous electric fields of the two cw lasers be:

$$\begin{aligned} E_1(t) &= A_1 \cos\left(\omega_1 t + \varphi_1\right) \\ \text{and } E_2(t) &= A_2 \cos\left(\omega_2 t + \varphi_2\right). \end{aligned} \tag{2.21}$$

The instantaneous electric field that illuminates the optical crystal is then:

$$E(t) = E_1(t) + E_2(t) = A_1 \cos\left(\omega_1 t + \varphi_1\right) + A_2 \cos\left(\omega_2 t + \varphi_2\right). \tag{2.22}$$

Using the Euler's formula, it can also be written as:

$$E(t) = \frac{A_1}{2} e^{\mathrm{j}(\omega_1 t + \varphi_1)} + \frac{A_1}{2} e^{\mathrm{j}(\omega_1 t + \varphi_1)} + \frac{A_2}{2} e^{\mathrm{j}(\omega_2 t + \varphi_2)} + \frac{A_2}{2} e^{\mathrm{j}(\omega_2 t + \varphi_2)}. \tag{2.23}$$

Upon the incidence of the electric field $E(t)$ onto the optical crystal, the nonlinearity of the optical crystal leads to a wave mixing. For the difference-frequency generation,

the second-order nonlinearity which is characterized by the second-order nonlinear susceptibility $\chi^{(2)}$ is responsible.

The induced second-order nonlinear polarization $P(t)$ is then given by:

$$\begin{aligned} P &= \epsilon_0 \chi^{(2)} E^2(t) \\ &= \frac{\epsilon_0 \chi^{(2)}}{4} \Bigg(A_1^2 e^{j(2\omega_1 t + 2\varphi_1)} + A_2^2 e^{j(2\omega_2 t + 2\varphi_2)} + 2A_1^2 A_2^2 e^{j((\omega_1+\omega_2)t + \varphi_1 + \varphi_2)} \\ &+ 2A_1^2 A_2^2 e^{-j((\omega_1+\omega_2)t + \varphi_1 + \varphi_2)} + A_1^2 e^{-j(2\omega_1 t + 2\varphi_1)} + A_2^2 e^{-j(2\omega_2 t + 2\varphi_2)} + 2A_1^2 + 2A_2^2 \\ &+ 2A_1^2 A_2^2 e^{j((\omega_1-\omega_2)t + \varphi_1 - \varphi_2)} + 2A_1^2 A_2^2 e^{-j((\omega_1-\omega_2)t + \varphi_1 - \varphi_2)} \Bigg) \end{aligned} \tag{2.24}$$

The frequency component highlighted in red is the generated terahertz radiation that has an angular frequency of $\omega_1 - \omega_2$ and a phase of $\varphi_1 - \varphi_2$.

As shown in Fig. 2.9(b), when a tilted laser beam is employed, a linear phase ramp is generated along the optical crystal due to the locally varying path length. This results in a linearly increasing phase difference between the two laser beams, which is translated into the local terahertz radiation through the difference-frequency generation. This resembles a terahertz phased array with a linear phase profile along the optical crystal, whose electric fields constructively interfere with each other in a specific direction in the far field. Unlike the traditional phased array deployed in the fiber-coupled optoelectronic terahertz system that requires the corporate feeding network and phase shifters, this approach simply yet effectively achieves spatial phase modulation without these additional components, significantly reducing the system complexity.

Maki and Otani have made significant advances in free-space terahertz beam steering systems using the technique of spatial phase modulation. In 2008, they reported on the successful overlap of two spatially dispersed laser beams to achieve an independent and simultaneous tuning of the terahertz frequency and main beam direction [85]. Through the linear adjustment of the overlapping area of two laser beams by mechanically shifting the mirrors reflecting one of the laser beams, they were able to decrease or increase the resulting terahertz frequency between 0.31 THz and 1.69 THz. At 0.6 THz, they were able to steer the direction of the terahertz beam within a range of 29° by tilting the mirror reflecting the laser beam by only 0.155°. In 2011, the same research group used two identical fs pump lasers to produce a periodic interference pattern,

a grating pattern, on a strip-line photoconductive antenna [86]. The spatial period of the grating is adjusted as the angle of incidence between the two pump laser varies, which in turn leads to the beam steering of the generated terahertz. At frequencies of 0.73 THz and 0.93 THz, they achieved a steering range of 20° with an incidence angle change of only 0.027° and 0.025°, respectively.

2.4 Free space-coupled terahertz beam steering and beam-forming devices

In contrast to the techniques discussed in earlier sections, the devices covered in this section are compatible with both optoelectronically and electronically generated terahertz sources. These devices are discrete building blocks that modulate the phase, and often the amplitude, of terahertz waves. The modulation occurs spatially as the free space terahertz wave passes through the devices, eliminating the need for a complex waveguide-based feeding network. However, it poses the disadvantage of the infeasibility of system integration, resulting in a beam steering system with a relatively large footprint. This section is divided into three subsections. In the first two subsections 2.4.1 and 2.4.2, I will provide a brief overview of the working principle of two kinds of semiconductor-based terahertz devices, and highlight research works that employ these techniques. In the third subsection 2.4.3, a Luneberg lens for the terahertz range will be discussed.

2.4.1 Photo-induced grating structure

When a light source illuminates semiconductor materials, such as Silicon, Gallium arsenide, Germanium, free carriers are generated once the photon energy of the light source exceeds the band gap of the semiconductor. The refractive index, the absorption constant, and the conductivity of the semiconductor varies with the change of the free-carrier density that is proportional to the illumination fluence of the light source. By using a specific illumination pattern of the light source, we can create a desired transmission response profile across the semiconductor film, thereby enabling amplitude or phase modulation of terahertz radiation passing through the film.

Busch and colleagues have demonstrated terahertz beam steering using a virtual diffrac-

tion grating on a Silicon film [87]. By illuminating the semiconductor with an alternating pattern of bright and dark regions, they are able to achieve periodic variation in transmission. However, this binary grating profile has a low grating efficiency and grating angle ambiguity, with the directivities of the diffraction angles at the +1 and -1 grating order being the same. To resolve this ambiguity, Steinbusch et al. used a graded illuminating pattern within one grating period on a thin Gallium arsenide film, resulting in an approximate blazed grating structure [88]. They experimentally demonstrated the toggling of the blazed angle between the +1 and -1 grating order as the blaze arrow changed from one side to the other.

Kannegulla and colleagues conducted a thorough investigation into the theory of the transmission response of the illuminated semiconductors and the impacts of substrate material, substrate thickness, illuminating light wavelength, and illuminating area on the terahertz modulation [89]. Their study provides a useful guideline for designing such terahertz modulators.

2.4.2 Photo-induced Fresnel zone plate

I will now discuss another photo-induced component for the terahertz range: the Fresnel zone plate. As the terahertz wave passes through a semiconductor film illuminated by a specific light pattern, both its phase and amplitude can be modulated. While the virtual diffraction gratings described in the previous subsection mainly rely on phase modulation, the Fresnel zone plate exploits direct amplitude modulation, making it capable of both beam steering and beamforming.

A two-dimensional Fresnel zone plate consists of concentric rings that alternate between being opaque and transparent as depicted in Fig. 2.10(a). In a photo-induced Fresnel zone plate, the opaque and transparent states are achieved by the presence and absence of illumination from a light source, respectively. Fig. 2.10(b) illustrates the principle of the focusing mechanism of a Fresnel zone plate. A beam radiated from the point source which is located at the position S passes the edge of the n-th Fresnel zone with radius of r_n, and is focused at the position P. The path length difference Δl_n between the path of the beam through the edge of the n-th Fresnel zone and the line of

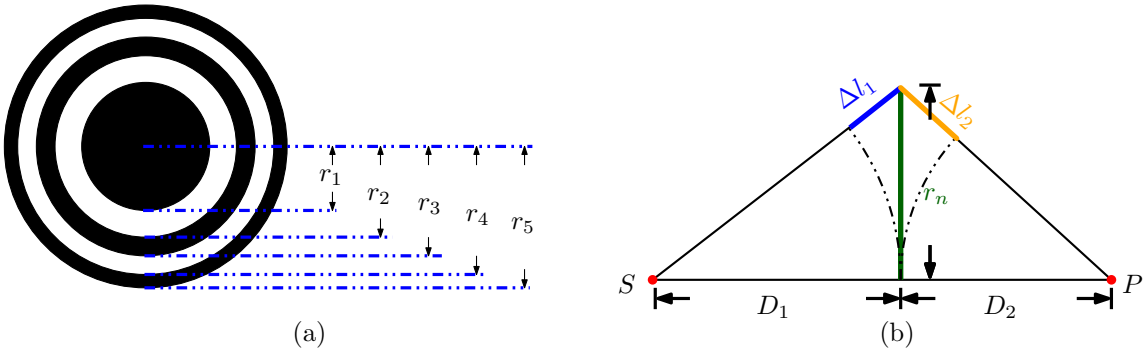

Figure 2.10: Schematic illustration of a Fresnel zone plate.

sight is given by:

$$\Delta l_n = \Delta l_{1,n} + \Delta l_{2,n} = \sqrt{D_1^2 + r_n^2} - D_1 + \sqrt{D_2^2 + r_n^2} - D_2. \tag{2.25}$$

The radius r_n of the n-th Fresnel zone must be chosen such that the path length difference Δl_n satisfies the following condition:

$$\Delta l_n \stackrel{!}{=} n \cdot \frac{\lambda}{2}, \tag{2.26}$$

where λ denotes the wavelength in free space. Eq. 2.26 reveals that beams passing through the adjacent zones interfere destructively, while the beams passing through every two zones interfere constructively at position P. As a result, masking every two Fresnel zones can create a focus at position P.

By inserting Eq. 2.26 into Eq. 2.25, rearranging, neglecting the higher order term of λ, and assuming that $n \cdot \lambda \ll D_1 + D_2$, it gives:

$$r_n^2 \approx n\lambda \cdot \frac{D_1 \cdot D_2}{D_1 + D_2}. \tag{2.27}$$

Using the thin lens equation $\frac{1}{D_1} + \frac{1}{D_2} = \frac{1}{f}$, where f is the focal length, Eq. 2.27 can be simplified to [90]:

$$r_n^2 \approx n \cdot \lambda \cdot f. \tag{2.28}$$

Eq. 2.28 provides the general design formula for the Fresnel zone plate to obtain a certain focal length.

In addition to the functionality of focusing with variable focal length, a reconfigurable Fresnel zone plate also provides the capability of beam steering. Fig. 2.11 illustrates two Fresnel zone plates with the beam direction pointing to the broadside at $\theta = 0°$ and an arbitrary angle of $\theta = \theta_0$.

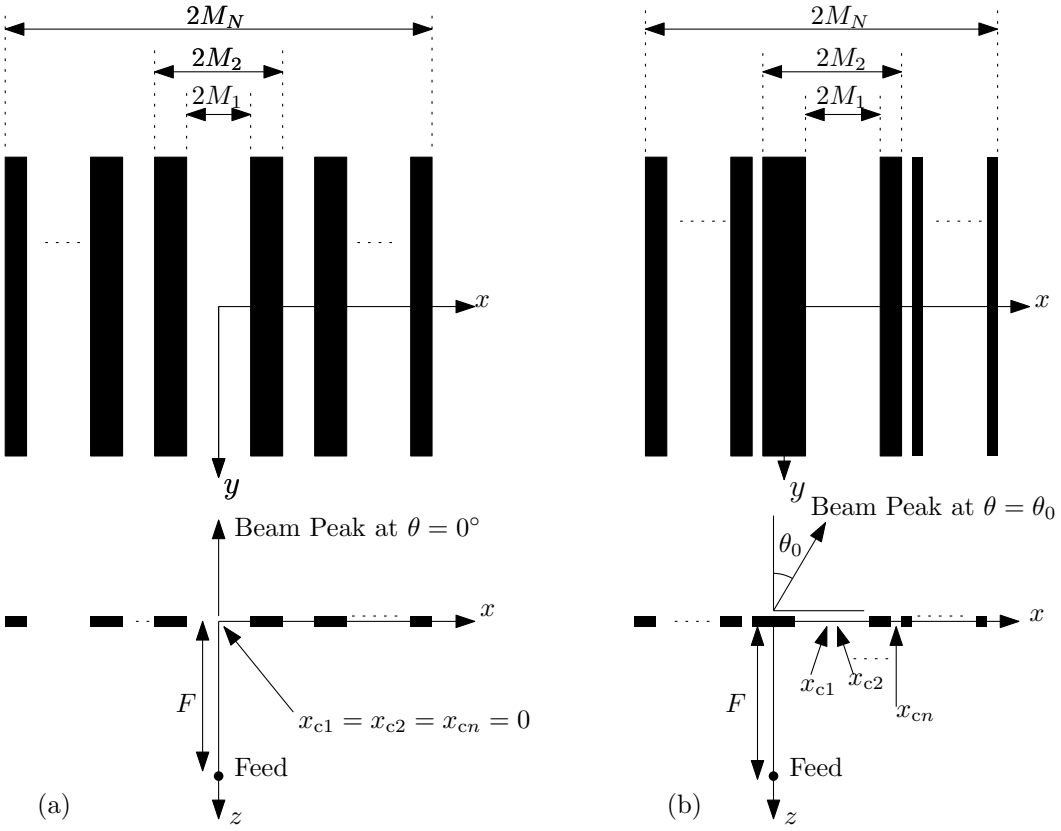

Figure 2.11: Schematic illustration of a 1D Fresnel zone plate with the beam peak (a) at $\theta = 0°$ and (b) at $\theta = \theta_0$ [91]. x_{cn} and M_n represent the center and length of the n-th zone, respectively.

Now, consider a point source at the focal point $z = -F$ of the Fresnel zone plate as depicted in Fig. 2.11. The field just before it interacts with the Fresnel zone plate at z=0 has the phase distribution:

$$\varphi_{\text{Feed}}(x) = \left(\sqrt{F^2 + x^2} - F\right) \cdot k, \tag{2.29}$$

where k is the wave number in free space.

In section 2.1.1, Eq. 2.2 shows the required phase difference between the adjacent array element of a phased array to steer the main beam to a target angle. This can be adapted

to calculate the phase distribution of the field after passing through the Fresnel zone plate in order to steer the beam to a given angle $\theta = \theta_0$:

$$\varphi_{\text{Required}}(x) = -k \cdot x \cdot \cos(\theta_0). \tag{2.30}$$

Thus, the phase response of the Fresnel zone plate can be simply calculated as:

$$\varphi_{\text{FZP}}(x) = \varphi_{\text{Feed}}(x) - \varphi_{\text{Required}}(x) \tag{2.31}$$

Petosa and co-workers derived equations to determine the center and length of the n-th zone for a given focal length F and scan angle θ_0 for a one-dimensional Fresnel zone plate [91]. Shams and co-authors adapted these equations to design a reconfigurable photo-induced two-dimensional Fresnel zone plate capable of achieving a total scan range of 24° at a frequency of 750 GHz [92].

2.4.3 Luneburg lens

A Luneburg lens is used to convert a point source that is located at its circumference to a collimated plane wave in free space on the opposite side and vice versa as illustrated in Fig. 2.12. It is a spherically symmetric gradient-index lens. Its refractive index is highest at the lens center, gradually decreases toward the outer surface, and reaches the minimum at the lens circumference. Due to the spherical symmetry of the Luneburg lens, a point source can be fed anywhere at the circumference, enabling a beam steering or beam switching functionality. Furthermore, owing to the linearity, multiple point sources can be fed to the Luneburg lens simultaneously, allowing the lens to have a multi-beam radiation pattern.

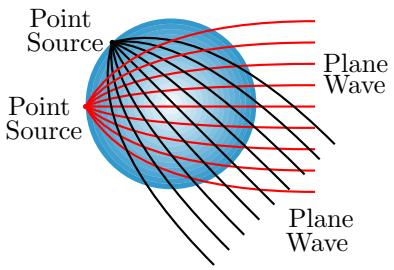

Figure 2.12: Schematic illustration of a Luneburg lens.

Luneburg's solution for the radial dependent refractive index $n(r)$ in a Luneburg lens is given by:

$$n(r) = \sqrt{2 - \left(\frac{r}{R}\right)^2}, \text{for } r \leq R, \tag{2.32}$$

where R denotes the radius of the Luneburg lens. According to this equation, the refractive index at lens center and the circumference shall be $\sqrt{2}$ and 1, respectively. It indicates the restriction of the Luneburg's solution: the refractive index distribution in Eq. 2.32 only applies when the refractive index can reach unity at the lens circumference which is rather challenging to manufacture such gradient-index materials. S.P. Morgen provides a more general solution to derive the refractive index distribution in the Luneburg lens for a given value of the refractive index at the circumference [93].

Headland et.al have employed a planar Luneburg lens using effective medium techniques in a demonstration of terahertz beam switching and multi-beam radiation [94]. The effective medium is realized by a lattice of through holes in a silicon slab. Its refractive index can be controlled by varying its fill factor. To feed the lens, they incorporated 7 evenly spaced photonic crystal waveguides, covering 120° field of view. The measured gain of the Luneburg lens lies in the range between 18 dBi and 25 dBi for the frequencies between 320 GHz and 390 GHz. The fabrication of the lens is simple thanks to the 2D micromachining and the lens is integrable with other silicon-based platforms. However, a continuous beam steering with this design is not feasible and the mechanical move of the terahertz source between the feeding waveguides limits the speed in changing the beam direction.

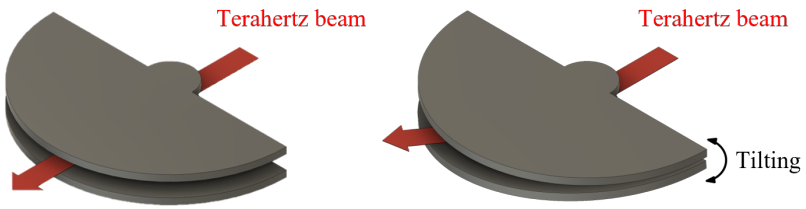

Figure 2.13: Illustration of a Luneburg lens using a parallel plate waveguide. The beam steering is achieved by tilting the lower plate with respect to the longitudinal axis [95].

To resolve these two problems, Sato and Monnai proposed a Luneburg lens using a parallel plate waveguide [95]. Since the effective refractive index between the parallel

plate waveguide depends on the distance between the two plates, the gradient-index of the Luneburg lens can then achieved by a properly designed variant curvature of the inner waveguide wall. As mentioned earlier in this subsection, the beam steering using the Luneburg lens is conventionally realized by changing the feeding position at its circumference. The parallel plate waveguide based Luneburg lens, as shown in Fig. 2.13, deflects the guided beam by a tiny tilt of the lower plate with respect to the longitudinal axis as a result of a linear perturbation of the effective refractive index along the transverse axis introduced by the tilt. With a tiny tilt the lower plate of the waveguide from -0.42° to 0.42°, a continuous beam steering at 300 GHz from -25° to 25° is successfully demonstrated.

2.5 Terahertz reflectarray

The concept of a reflectarray is first proposed by Berry, Malech, and Kennedy [96]. They combine the natures of two components: the antenna array and reflector, forming the reflectarray. Unlike the conventional antenna array whose feed network is usually transmission line or waveguide based, the reflectarray shares the nature of a reflector: the feed is done spatially by illuminating its aperture. For applications requiring a specific radiation pattern or a dynamic beam steering capability, the reflectarray makes use of the array nature to synthesize the phase profile over the aperture accordingly.

In RF domain, the reflectarray has been intensively studied and developed with an ultimate goal of its employment in wireless and satellite communication, as well as radar systems, replacing the bulky parabolic reflector. It offers numerous advantages, such as low mass, low cost, small footprint, ease of fabrication, and most importantly, a phase tuning mechanism can be incorporated in the array elements for beam steering applications. In the review paper [97], various phase tuning mechanisms for the reflectarray operating at RF frequencies and the associated enabling technologies are covered in detail. Here, I will briefly mention four of the most common phase tuning mechanisms:

- incorporating a phase shifter or true time delay unit to each array element, individually tuning the phase of the locally incident wave before radiating back to free space,

- varying the size of the array element, individually tuning the resonant frequency of each element, a distinct phase shift resulting from the offset between the feed and resonant frequency is then imposed on the locally scattered wave,
- for a circular polarized incident wave, rotating a circular polarized array element, a distinct phase shift that corresponds to the angle of rotation is imposed on the locally scattered wave,
- using functional materials whose dielectric properties can be electronically controlled, such as liquid crystal and graphene, manipulating the local surface impedance, subsequently the local reflection coefficient.

In order to adopt these phase tuning mechanisms at terahertz regime, the available enabling technologies are the key. Here, I will briefly discuss the existing demonstration/prototype of terahertz reflectarrays using those phase tuning mechanisms and the associated enabling technologies.

Due to the lack of solid-state electronics working directly at terahertz frequencies, the phase tuning mechanism that incorporates the phase shifter and true-time delay unit in each array element is so far less feasible.

For a static reflectarray whose phase distribution is introduced by array elements with varying dimensions, a fabrication process on a sub-wavelength scale is required. The matured micro-machining technologies can be used to fabricate such terahertz arrays, since it works on the same scale as the sub-wavelength of terahertz. Niu and coworkers presented a 2D terahertz reflectarray that deflects the incident wave in a given direction using squared metallic microstrip patches as the array elements [98]. The length of the squared patching varies only in one dimension while the patches along the other dimension have the same size. The lengths of the patches are chosen so that a wrapped phase ramp distribution is formed. The same research group have also proposed a reflectarray that is employed as a terahertz free-space polarizing beam splitter [99]. They use two sets of orthogonal strip dipoles to deflect the orthogonal polarized beams in two different directions.

Most reflectarrays have an inherent disadvantage in that they typically operate over a very limited bandwidth. This limitation comes from two main factors, the narrowband nature of the array element itself, and the phase error of the phase tuning mech-

anism at different frequencies. As an example, the resonant frequency of a metallic patch element versus its path length is a non-linear characteristic. Therefore, the phase distribution is rapidly distorted as the feed frequency is tuned away from the resonant frequency. In order to achieve broadband operation, we need an array element that has a linear phase response with respect to the feed frequency. Metamaterial, for example, can be used to achieve that. You and Co-workers presented a design of a metasurface reflectarray that is able to perform focusing over a 3dB relative bandwidth of 23.3% and 23.9% around 1 THz for TE and TM polarization, respectively [100].

As the frequency increases to the short wavelength range of terahertz, the metals used for the patch and dipole are no longer ideal conductors. As a result, ohmic losses are evident when the incident wave interacts with the metallic array elements. As an alternative design, dielectric resonators with varying dimensions can be used as array elements for terahertz reflectarrays. In the work presented by Headland et. al., they used cylindrical resonators made of high resistive silicon adhered to a gold plate to form a terahertz reflectarray [101]. As a proof of concept, the designed reflectarray was shown to focus collimated incident waves.

Although those reflectarrays with metallic or dielectric elements exhibit good performance in deflecting and focusing the incident beam in a predetermined direction, they remain static, i.e., lacking of ability to reconfigure the phase distribution. Functional materials, such as graphene and liquid crystals, whose dielectric properties can be electrically controlled, offer the possibility of dynamic terahertz reflectarrays. Many numerical studies have demonstrated the feasibility of such reflectarrays [102,103]. However, only a few prototypes have been experimentally demonstrated.

Owing to the relatively short wavelength of terahertz waves compared to the microwave region, the phase of the locally incident terahertz wave can also be modulated spatially by each individual array element. The array element shall include a reflective element controlled by an actuation system, moving in a linear or rotary motion. One of the common designs of the reflectarray using a spatially phase tuning mechanism is a reconfigurable diffraction grating. By changing its grating period, dynamic beam steering can be achieved. Monnai et al. presented a reconfigurable terahertz diffraction grating consisting of 256 cantilevers and demonstrated the reflectarray with a steerable range of 40° at 0.3 THz [104]. These cantilevers can be controlled individually to be in one of the binary states: up-state or down-state. The vertical displacement between the

states is only 80 μm. This leads to a poor grating efficiency, i.e., the specular reflection is therefore around 20 dB higher than the first order diffraction.

A grating structure with poor grating efficiency creates for such reflectarrays the disadvantage of grating lobes. To improve the grating efficiency, we can start from two aspects:

- The size of the single reflective element shall be in the order of sub-wavelength of the operating frequency to suppress diffraction effects from individual elements,
- an actuation system shall support a high throw that is comparable to the wavelength of the operating frequency and a fine resolution allowing a flexible configuration.

CHAPTER

THREE

MEMS-BASED RECONFIGURABLE APPROXIMATE BLAZED GRATING FOR TERAHERTZ BEAM STEERING

In order to maximize the grating efficiency in a specific grating order, a blazed grating can be used. The repeating unit of a blazed grating is a ramp-shaped reflective surface and the slope of the ramp is designed so that the specular reflection on it aligns with one of the diffraction angle of the grating. This repeating unit is also commonly refered to as the grating element. An ideal design for a 1D reconfigurable terahertz blazed grating would be a row of reflective elements, whose dimension parallel to the grating axis is in sub-wavelength scale. Each reflective element shall be actuated to perform linear and tilting motions. Furthermore, to ensure a blazed grating design for a large beam steering range, the linear and tilting movements shall have a large displacement. Take a reflective grating for 300 GHz for example. For a full steering range of $\pm 90^\circ$ away from the normal to the grating, the tilting motion must be at $\pm 45^\circ$ and the vertical displacement must be equal to the wavelength of 300 GHz in free space, i.e., 1 mm.

In this chapter, I present a novel design for an approximate blazed grating. This design replaces the traditional ramp-shaped configuration with multiple sub-wavelength reflective elements, each independently actuated along the x-axis, as illustrated in Fig. 3.1. To facilitate this actuation system, MEMS technology offers a solution, enabling precise linear displacement over several hundred micrometers.

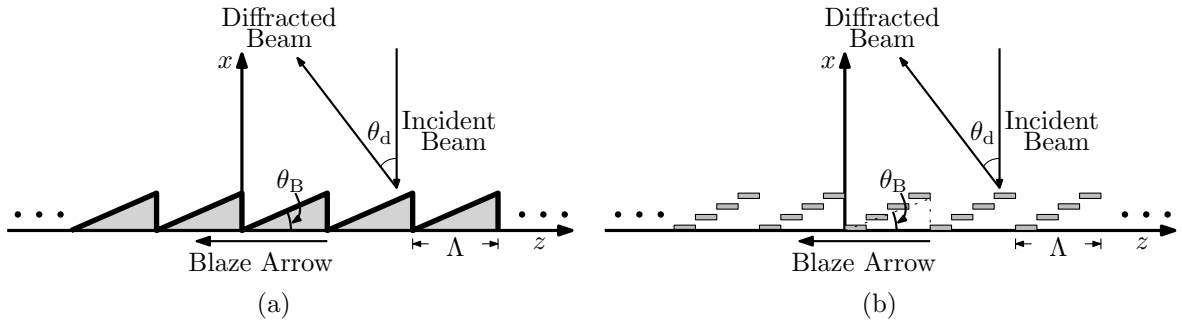

Figure 3.1: Illustration of (a) a blazed grating and (b) an approximate blazed grating featuring multiple sub-wavelength reflective elements.

This chapter comprises five sections. The design considerations as well as key parameters of the MEMS-based actuation system and the reflective element are given in the first two sections, respectively. The phase tuning of the incident wave is done by adjusting the vertical position of the reflective element, the array factor can no longer be applied to calculate the radiation pattern of such a reflectarray. A mathematical model based on the Huygens-Fresnel principle is therefore given to calculate the radiation pattern of the grating structure in section 3.3. The design of a reconfigurable approximate blazed grating is described in section 3.4. In addition, based on the calculated radiation patterns, the achievable steering range and operating frequency range of the designed blazed grating are also discussed in this chapter. At last in section 3.5, full-wave EM simulation using a finite-difference time-domain (FDTD) solver and far-field radiation pattern measurements are carried out to validate the functionality of the designed blazed gratings.

3.1 Key parameters of the MEMS actuation system

The MEMS actuation system has the ability to achieve translational displacement in the sub-millimeter range, which aligns with the wavelength range of the terahertz waves. As a result, a reflective surface driven by a MEMS actuation system can be employed to spatially modulate the phase of the terahertz waves and the stacking of multiple reflective elements for constructing a reconfigurable terahertz reflectarray holds great potential. MEMS actuation systems are characterized by their advantageous properties such as their lightweight and compact nature [105]. Furthermore, when electrostatic

actuators are employed, they consume extremely low power [106]. In this work, the MEMS electrostatic actuators driven by an in-plane mechanical digital-to-analog converter (DAC), developed by our project partner Lisa Schmitt and colleagues, are considered. They have successfully demonstrated a 3-ternary digit actuation system capable of positioning the reflective element uniformly in $3^3 = 27$ different locations within a displacement range of 120 μm [16]. This system can be further enhanced to increase its compatibility with terahertz beam steering applications by increasing the numbers of the ternary digits and amplification factor of the mechanical amplifier [107, 108]. In the present chapter and subsequent ones, a 5-bit actuation system with a maximum displacement of 600 μm is considered for the MEMS actuation system. It is worth mentioning that a more sophisticated actuation system is considered here so that the proposed designs of the reflectarray can also be easily adapted to a simpler system.

3.2 Key parameters of the reflective element

The reconfigurable reflectarray shall approximate a blazed grating, there are mainly two design aspects that affect the radiation pattern of the approximate blazed grating: the dimension of the reflective element and the amount of elements used within the reflectarray. A section of an approximate blazed grating structure is shown in Fig. 3.2. The grating element comprises multiple reflective elements with a size of width w and length l, forming an approximate ramp. The periodic grating elements are placed along the $z-$axis which makes it the grating axis. The normally incident wave can be diffracted in a different direction in the elevation plane by changing the grating period Λ.

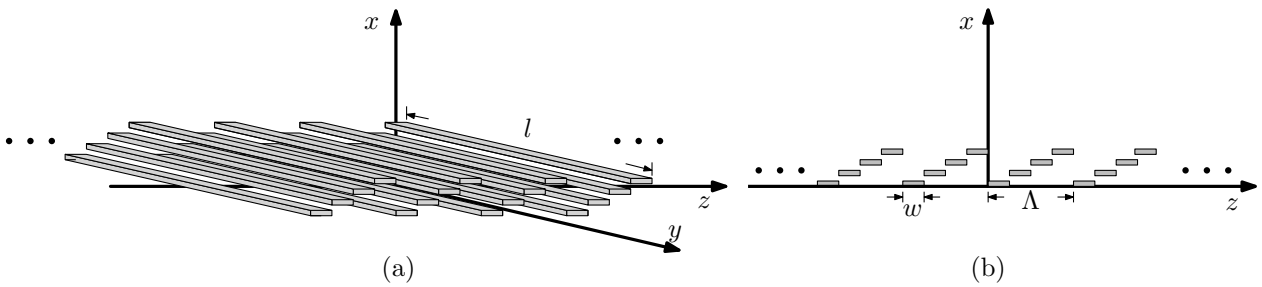

Figure 3.2: 3D (a) and 2D (b) illustration of a diffraction grating consisting of multiple subwavelength reflective elements.

However, the repeating unit of the diffraction grating consists of multiple identical reflective elements, effectively forming a diffraction grating with a period equal to the width the reflective element. The diffracted beam within the repeating unit can introduce spurious beams into the radiation pattern of the designed reflectarray. To mitigate this, the width w of the reflective element must be carefully chosen to reduce diffraction effects within the repeating unit. I have decided on a width of 300 μm, precisely one wavelength at 1 THz. For normal incidence on a grating structure, which, in this case , is the repeating unit, the grating equation is represented as:

$$w \sin(\theta_{\mathrm{d},m}) = m\lambda,\ m \in \mathbb{Z}, \tag{3.1}$$

where $\theta_{\mathrm{d},m}$ is the m-th-order diffraction angles and λ denotes the wavelength. Considering a frequency $f \leq 1\,\mathrm{THz}$, corresponding to a wavelength $\lambda \geq 300\,\mu\mathrm{m}$, and a reflective element width $w = 300\,\mu\mathrm{m}$, Eq. 3.1 yields results only for $m = 0$, giving $\theta_{\mathrm{d},0} = 0^\circ$, indicating specular reflection. In this scenario, no other diffraction angles occur, making the impact of the diffraction within the grating element on the radiation pattern of the reflectarray negligible up to 1 THz.

The electrical length of the reflective element along the $y-$axis determines the beam width in the azimuth plane. For a single frequency, the electrical length is proportional to its geometrical length l. Even though the beam is only steered in the elevation plane, an adequately narrow beam in the azimuth plane is still desired to avoid the interference and ambiguity. So the length l shall be large but not too bulky for the MEMS actuation system. I have decided on a length of 5 mm which is 5λ at 300 GHz.

The directivity in the elevation plane increases, and the beam width becomes narrower as the number of reflective elements within the reflectarray increases. While achieving high directivity and a narrow beam width is undoubtedly desirable, we have to keep in mind that such improvements come at the cost of increased technological complexity. This complexity is primarily related to the layout design necessitated by a large number of bond pads and wire bonding. The choice of the number of reflective elements depends on the specific requirements for directivity, beam width, and the diameter of the incident terahertz beam. In the subsequent numerical and experimental analysis of the reflectarray presented in this work, a reflectarray configuration comprising 80 reflective elements is considered.

3.3 Mathematical model

As the phase of the incident wave is modulated spatially by the changing position of the reflective element, the array factor can be no longer applied to calculate the radiation pattern of the reflectarray. In the proposed mathematical model, I calculate the fields of the reflected wave just above the reflective surfaces, the total field of the reflectarray in far-field region can be obtained by using the Huygens-Fresnel principle, i.e., superposition of the fields from these reflective surfaces.

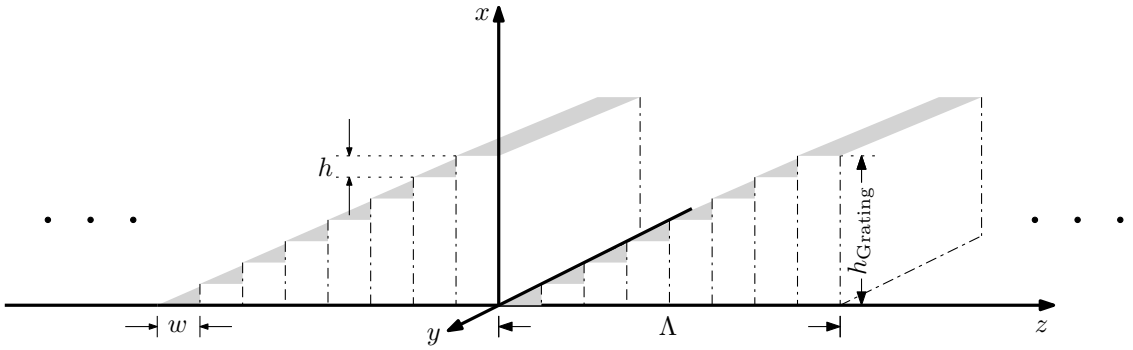

Figure 3.3: 3D illustration for a section of a diffraction grating [1].

The repeating unit, also referred to as a grating element, is composed of a number of N reflective elements, forming an approximate ramp with a grating period of Λ. Each reflective element has a width of w and length of l and a number of N_{total} elements constructs the reflection grating. Within one grating element, the $x-$coordinate of the reflective element increases linearly with an increment of h along the $-z$-axis as shown in Fig. 3.3.

The height profile of the reflective elements within the first grating element $x_{\text{element}}(z)$ along the $z-$ axis is the summation of N rectangular functions:

$$x_{\text{element}}(z) = \sum_{n=1}^{N} \text{rect}\left(\frac{z - \frac{w \cdot (N_{\text{total}} - 1)}{2} + (n-1) \cdot w}{w}\right) \cdot (n-1) \cdot h. \tag{3.2}$$

The height profile of the reflective elements within the diffraction grating, denoted as $x_{\text{grating}}(z)$ along the $z-$ axis, is hereby a periodic repetition of $x_{\text{element}}(z)$ with a period Λ. In the case where the total number of the elements N_{total} within the grating is not

a multiple integer of the number of elements N within the grating element, a partial grating element with a number of $N_{\text{total}} - \lfloor \frac{N_{\text{total}}}{N} \rfloor \cdot N$ elements emerges:

$$x_{\text{grating}}(z) = x_{\text{element}}(z) * \sum_{k=0}^{\lfloor \frac{N_{\text{total}}}{N} \rfloor} \delta(z - k \cdot \Lambda) + \sum_{n=1}^{N_{\text{total}} - \lfloor \frac{N_{\text{total}}}{N} \rfloor \cdot N} \text{rect}\left(\frac{z - w \cdot \left(\lfloor \frac{N_{\text{total}}}{N} \rfloor \cdot N - \frac{N_{\text{total}}}{2} \right) + (n-1) \cdot w}{w} \right) \cdot (n-1) \cdot h. \tag{3.3}$$

For the simplicity, I assume a linearly polarized incident plane wave whose polarization is parallel to $z-$axis and the amplitude of the incident wave E_0 has no variation within the reflective element of the grating structure:

$$\mathbf{E}_{\text{incident}}(z) = \mathbf{e}_z \cdot E_0 \cdot \mathrm{e}^{\mathrm{j}\Delta\varphi_{\text{incident}}} \cdot \mathrm{e}^{-\mathrm{j}k_0 x}, \tag{3.4}$$

where $\mathbf{e}_z$ is the unit vector in z direction and k_0 is the wave number in free space. Since the incident wave is a plane wave, the phase $\Delta\varphi_{\text{incident}}$ is constant across a wavefront.

Once the incident wave interacts with the grating structure, a phase profile is imposed on the reflected wave just above the reflective surfaces. It can be determined by the multiplication of the height profile of the grating $x_{\text{grating}}(z)$ with the wave number k_0 in free space:

$$\mathbf{E}_{\text{reflected}}(z) = \mathbf{e}_z \cdot E_0 \cdot \mathrm{e}^{\mathrm{j}\Delta\varphi_{\text{incident}}} \cdot \mathrm{e}^{-\mathrm{j}k_0 x_{\text{grating}}(z)}. \tag{3.5}$$

The reflective element can be modelled approximately by multiple isotropic radiators located adjacently. To illustrate the calculation of the far-field radiation pattern of the reflectarray, two arbitrary isotropic radiators located at (x_n, z_n) and (x_m, z_m) on two distinct reflective elements are selected, as depicted in Fig. 3.4. In the far field region, an observation point P is chosen at a radial distance r from the coordinate origin and at an angle θ away from the $z-$axis. The electric field at point P is determined by the superposition of the fields from these two radiators:

$$\mathbf{E}_{\text{FF,2-element}}(r, \theta) = \frac{\mathbf{E}_{n,\text{reflected}}}{|\mathbf{r}'_n|} \cdot \exp\left(-\mathrm{j}\mathbf{k}_n \cdot \mathbf{r}'_n\right) + \frac{\mathbf{E}_{m,\text{reflected}}}{|\mathbf{r}'_m|} \cdot \exp\left(-\mathrm{j}\mathbf{k}_m \cdot \mathbf{r}'_m\right), \tag{3.6}$$

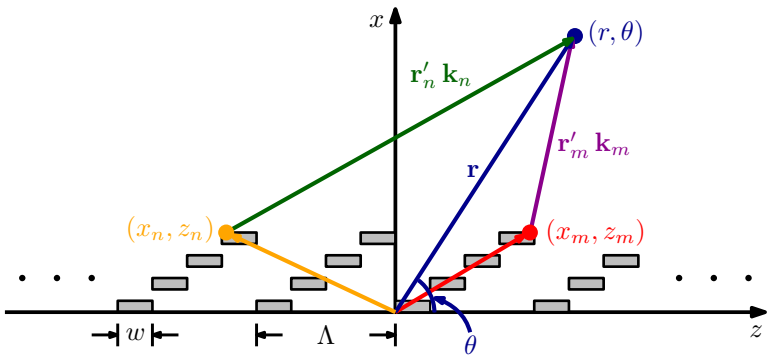

Figure 3.4: Coordinate system for calculating the far-field radiation pattern of the reflectarray.

where the vectors $\mathbf{r}'_n$ and $\mathbf{k}_n$ represent the distance and wavenumber vectors from n-th radiator to the far field observation point P, respectively. These are given by:

$$\mathbf{r}'_n = \sqrt{(\cos\theta \cdot r - z_n)^2 + (\sin\theta \cdot r - x_n)^2} \cdot \mathbf{e}_{r'_n} \text{ and} \tag{3.7}$$

$$\mathbf{k}_n = \frac{2\pi}{\lambda} \cdot \mathbf{e}_{k_n}. \tag{3.8}$$

Similarly, the vectors $\mathbf{r}'_m$ and $\mathbf{k}_m$ represent the distance and wavenumber vectors from m-th radiator to the far field observation point P, respectively. These are given by:

$$\mathbf{r}'_m = \sqrt{(\cos\theta \cdot r - z_m)^2 + (\sin\theta \cdot r - x_m)^2} \cdot \mathbf{e}_{r'_m} \text{ and} \tag{3.9}$$

$$\mathbf{k}_m = \frac{2\pi}{\lambda} \cdot \mathbf{e}_{k_m}, \tag{3.10}$$

where $\mathbf{e}'_r$ and $\mathbf{e}_k$ are the unit vector in $\mathbf{r}'$ direction and $\mathbf{k}$ direction, respectively. Since the wavenumber and the observation vectors are in the same direction, the term $\mathbf{k} \cdot \mathbf{r}'$ is reduced to

$$\mathbf{k} \cdot \mathbf{r}' = |\mathbf{r}'| \cdot |\mathbf{k}| \tag{3.11}$$

Eq. 3.6 easily extends to accommodate the case of a total number of M isotropic radiators within the entire reflectarray:

$$\mathbf{E}_{\text{FF}}(r,\theta) = \sum_{l=1}^{M} \frac{\mathbf{E}_{l,\text{reflected}}}{|\mathbf{r}'_l|} \cdot \exp\left(-\mathrm{j}\mathbf{k}_l \cdot \mathbf{r}'_l\right) \mathrm{d}x. \tag{3.12}$$

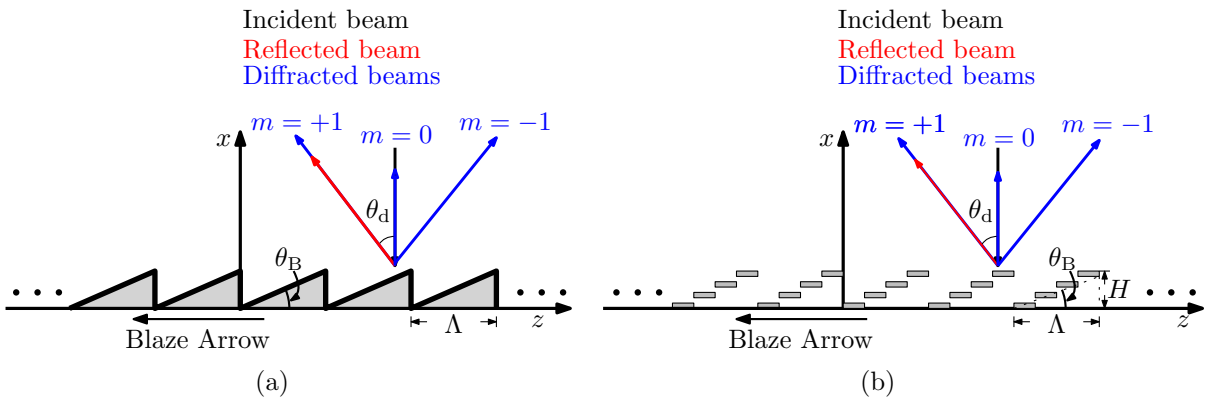

Figure 3.5: Illustration of (a) a blazed grating where the grating efficiency at the first diffraction order $m = 1$ is maximized and (b) an approximate blazed grating featuring multiple sub-wavelength reflective elements as grating elements.

3.4 Approximate blazed grating

A grating is a blazed grating when its diffracted beam of the grating structure coincides with the reflected beam of the grating element. For this to hold at normal incidence, the tilting θ_B of a saw-tooth shaped blazed grating shown in Fig. 3.5 must be in the form

$$\theta_B = \frac{1}{2}\theta_d, \tag{3.13}$$

where θ_d is the angle between the diffracted beam and the grating's normal vector.

The design variable grating period Λ determines the m-th-order diffraction angles $\theta_{d,m}$ which are given by the grating equation at normal incidence

$$\sin(\theta_{d,m}) = m \cdot \frac{\lambda}{\Lambda},\ m \in \mathbb{Z}. \tag{3.14}$$

For a blazed grating, the design variable ramp rise $H = h_{\text{Grating}}$ determines in which order of diffraction is the most of the diffracted power concentrates. In this design, I aim to maximize the grating efficiency at the first diffraction order $m = 1$. The ramp rise H can thus be calculated

$$\begin{aligned} H &= \Lambda \cdot \tan\theta_B \\ &= \Lambda \cdot \tan\frac{\theta_{d,1}}{2}. \end{aligned} \tag{3.15}$$

Using Eq. 3.14, we can write Eq. 3.15 as

$$\begin{aligned} H &= \Lambda \cdot \tan \frac{\theta_{\mathrm{d},1}}{2} \\ &= \Lambda \cdot \tan \left(\frac{\arcsin\left(\frac{\lambda}{\Lambda}\right)}{2} \right). \end{aligned} \tag{3.16}$$

In the proposed blazed grating, the ramp is approximated by a number of N reflective elements driven by MEMS linear actuators. The ideal height increment h between the adjacent reflective elements within one grating element shall be

$$h = \frac{H}{N-1}. \tag{3.17}$$

For the approximate blazed grating, both design variables the grating period Λ and height increment h have constraints. The grating period Λ can only be the integer multiple of the reflective element's width w. The MEMS actuation system determines the achievable height increment h. In the following subsections, I discuss the performance and limitations of the approximate blazed grating that takes these constraints into account.

3.4.1 Phase ambiguity

The minimum ramp rise H_{min} for a blazed grating can be obtained by using the small-angle approximation $x \leq \arcsin(x)$ for $0 \leq x \leq 1$ and $x \leq \tan(x)$ for $0 \leq x \leq \frac{\pi}{2}$ in Eq. 3.16,

$$H = \Lambda \cdot \tan \left(\frac{\arcsin\left(\frac{\lambda}{\Lambda}\right)}{2} \right) \geq \Lambda \cdot \frac{\frac{\lambda}{\Lambda}}{2} \Rightarrow H_{\mathrm{min}} = \frac{\lambda}{2}. \tag{3.18}$$

Within one grating element of an ideal blazed grating, a linear phase ramp with a rise of at least π (which corresponds to $\frac{\lambda}{2}$) is introduced as the locally incident wave first interacts with the grating element. Note that the diffracted beam experiences the same phase ramp again when it is diffracted from the grating element. In total, a ideal blazed grating element introduces a linear phase ramp with a rise of at least 2π. The approximate blazed grating discretizes the linear phase ramp and depending on how many reflective elements are inside a grating element, a phase ambiguity may occur.

First, the case is considered where a grating element consists of only two reflective elements. The height increment h between these two reflective elements must be equal to the ramp rise H to approximate the blazed grating. The linear phase ramp is thus sampled only at the two ends. With the small-angle approximation, the resulting phase difference between these two reflective elements is 2π which is equal to 0 phase shift. The approximate blazed grating with two reflective elements inside a grating element thus introduces a flat phase profile. As a result, the incident beam is reflected in a specular manner.

Next, the case is considered where a grating element consists of three reflective elements. The linear phase ramp is thus sampled at the two ends and in the middle. With the small-angle approximation, the resulting phase profile by these three reflective elements is $\{0, \pi, 2\pi\}$ that can also be interpreted as $\{2\pi, \pi, 0\}$. With the phase profile of $\{0, \pi, 2\pi\}$ the normally incident wave is diffracted on the left hand side of the grating's normal vector, whereas the normally incident wave is diffracted on the right hand side of the grating's normal vector with the phase profile $\{2\pi, \pi, 0\}$. As a result, two grating lobes are formed.

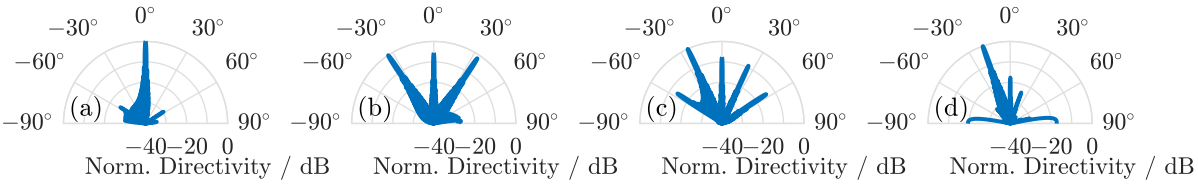

Figure 3.6: Calculated radiation pattern of the approximate blazed grating with (a) two reflective elements per grating period, (b) three reflective elements per grating period, (c) four reflective elements per grating period, and (d) five reflective elements per grating period [1].

To investigate the impact of the aforementioned phase ambiguity on the radiation pattern of the approximate blazed grating, I calculate and depict the radiation pattern for a beam at 0.6 THz diffracted by an approximate blazed grating with varying numbers of reflective elements: two, three, four, and five. The corresponding figures are presented in Fig. 3.6 (a), (b), (c), and (d), respectively. As anticipated, the specular reflection dominates for the case where a grating element consists of two reflective elements. Grating lobes on both sides of grating's normal vector appear for the case where a grating element consists of three reflective elements. Once each grating element has four or more

reflective elements, we are able to steer the beam in the desired direction and with a directivity at least 10 dB higher than the sidelobes.

3.4.2 Achievable steering angles

According to the grating equation Eq. 3.14, for the diffraction effect to occur, that grating period Λ must be equal to or greater than the wavelength λ in free space. In addition, there must be four reflective elements per grating period to resolve the phase ambiguity, avoiding the grating lobes. Four reflective elements results in a grating period of 1.2 mm which is greater than the wavelength for the frequency range between 0.3 THz and 1 THz. Therefore, 1.2 mm is the minimum grating period that determines the maximum steering angle off the grating's normal vector. The minimum steering angle is limited by the displacement resolution h_{min} of the MEMS actuation system. Once the height increment h between the adjacent reflective elements within one grating element falls below the h_{min}, the minimum steering angle occurs.

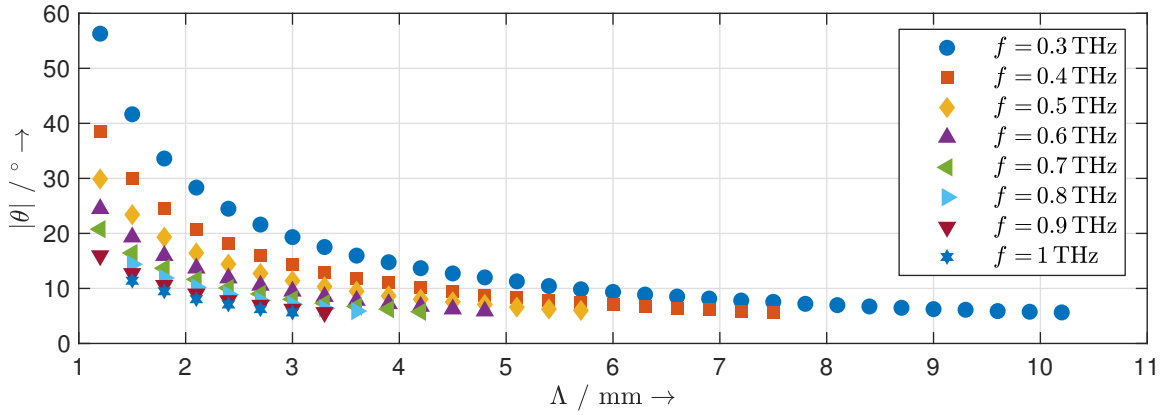

Figure 3.7: Calculated achievable steering angles of the reconfigurable reflectarray that approximates the blazed gratings with different grating periods at different frequencies [1].

The achievable steering angles for the frequencies between 0.3 THz and 1 THz with a 0.1 THz increment is shown in Fig. 3.7. Note that the same steering angles on the other side of grating's normal vector can be achieved by changing the direction of the blazed arrow. The achievable angles are discrete since the grating element must comprise an integer multiple of reflective elements. As the frequency increases, the wavelength is

decreases, leading to a narrower steering range, as predicted by the grating equation Eq 3.14.

3.4.3 Directivity and grating efficiency

To take a closer look at the beam steering performance of the approximate blazed grating, I calculate its radiation patterns for the maximum and minimum steering angles as well as the middle of the steering range at the frequencies 0.3 THz, 0.6 THz and 0.9 THz and show them in Fig. 3.8.

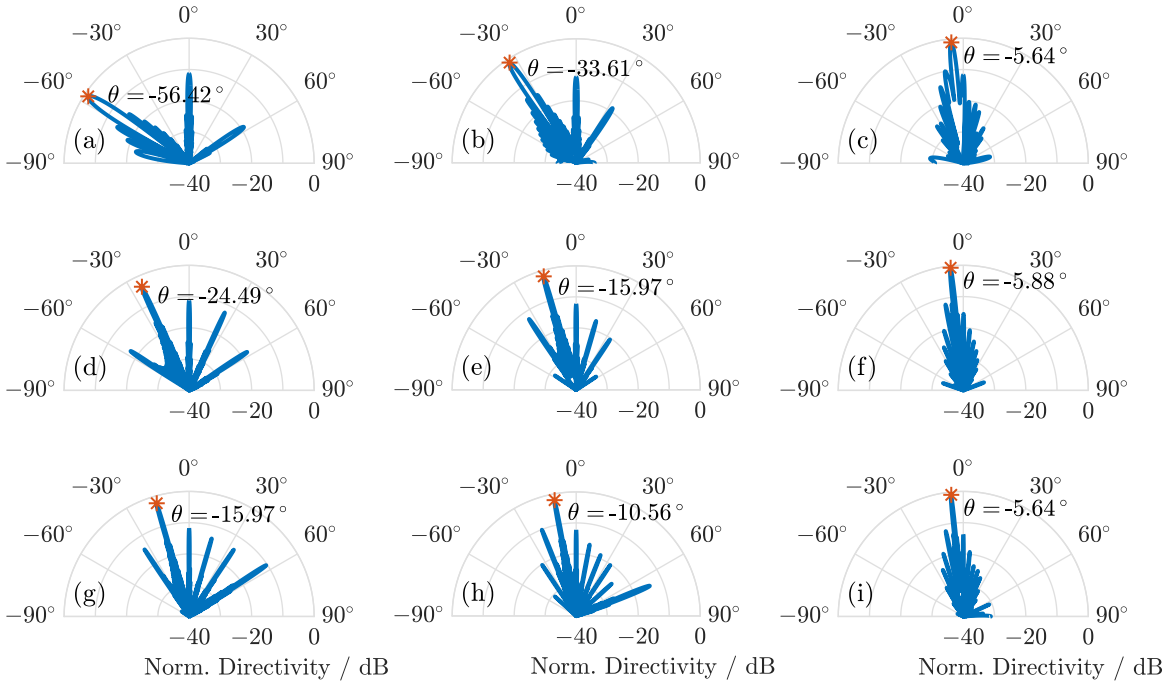

Figure 3.8: Calculated radiation patterns of the approximate blazed grating configured for (a) the maximum steering angle at 0.3 THz, (b) the middle of the steering range at 0.3 THz, (c) the minimum steering angle at 0.3 THz, (d) the maximum steering angle at 0.6 THz, (e) the middle of the steering range at 0.6 THz, (f) the minimum steering angle at 0.6 THz, (g) the maximum steering angle at 0.9 THz, (h) the middle of the steering range at 0.9 THz, and (i) the minimum steering angle at 0.9 THz [1].

In addition to the main lobe in the desired direction and specular reflection at 0°, we also observe many evident side lobes. The specular reflection at 0° and those side lobes

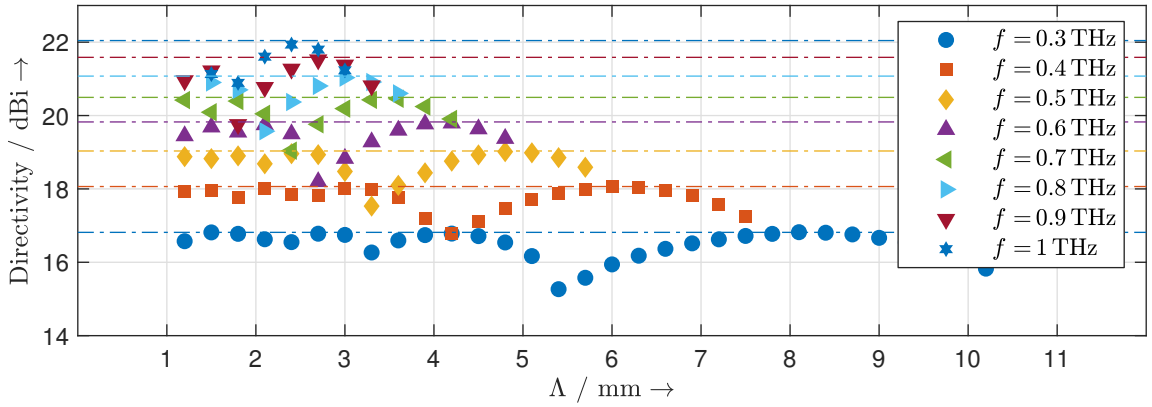

Figure 3.9: Directivity of the approximate blazed grating for different grating periods at different frequencies (solid points) and theoretical directivity of a uniform linear antenna array with the same dimension (dashed line) [1].

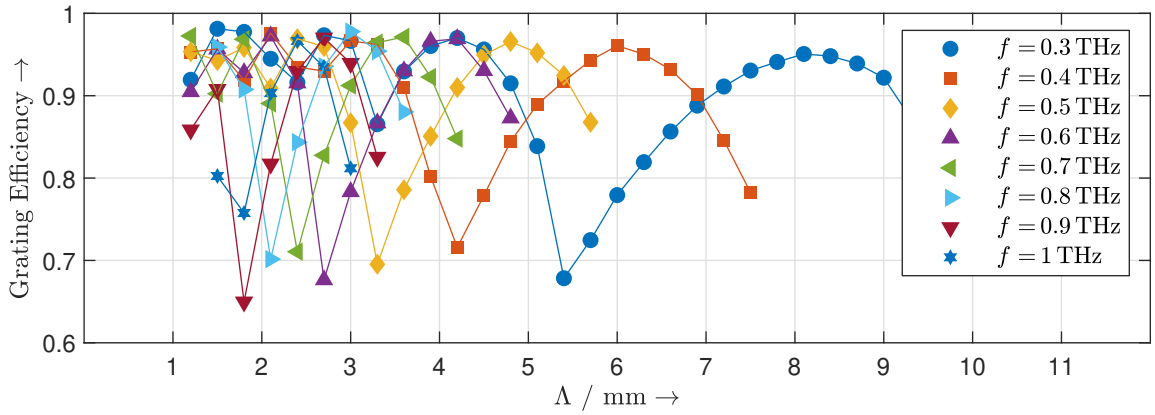

Figure 3.10: Grating efficiency of the approximate blazed grating for different grating periods at different frequencies [1].

worsens the performance of the approximate blazed grating and degrades the grating efficiency η_{grating}, which is defined as the ratio of the power carried by the diffracted beam P_{m_0} at a certain diffraction order over the incident power P_{incident} on the grating, expressed as:

$$\eta_{\text{grating}} = \frac{P_{m_0}}{P_{\text{incident}}}. \tag{3.19}$$

To quantify this impact, for each reflectarray configuration corresponding to each achievable steering angle shown in Fig. 3.7, I calculate its maximum directivity and depict in

Fig. 3.9. As the frequency increases, the electrical size of the approximate blazed grating increases, this subsequently results in a higher directivity. Within the steering range at one frequency, the maximum directivity remains adequately constant and comparable with the theoretical maximum directivity of a equivalent uniform linear array of isotropic radiators. The distinct notches appear as the grating efficiency η_{grating} drops, as shown in Fig. 3.10, owing to the geometric deviation of the approximate blazed grating from the ideal one.

3.5 Characterization

In order to verify the proposed mathematical model and the functionality of the approximate blazed grating, I conduct full-wave EM simulations of the designed approximate blazed grating and carry out proof-of-concept measurements on reflectarray phantoms. In the first part of this section, a detailed EM simulation setup is described and a comparison between the simulated and calculated radiation patterns is given. As for the proof-of-concept measurements, two reflectarray phantoms-reflectarrays with fixed reflectors, i.e., without MEMS actuation systems are fabricated. They are made of a silicon wafer whose characteristics are the same as for the reconfigurable reflectarray. Far-field radiation pattern measurements of these two reflectarray phantoms are performed using both terahertz time-domain and frequency-domain spectroscopy systems. The second subsection includes the measurement setups and a thorough analysis of the measurement results.

3.5.1 EM simulation

An FDTD solver Empire XPU is used to conduct the full-wave EM simulations of the designed approximate blazed grating. Fig. 3.11 illustrates the EM simulation setup. The reflective elements are modelled as the bulky rectangular boxes (in blue) with a relative permittivity of silicon in the terahertz regime of $\epsilon_{\text{r}} = 11.73$. The side of the rectangular box lying on the yz-plane represents the reflective surfaces. Each reflective surface has a size of $300\,\mu\text{m} \times 5000\,\mu\text{m}$. A plane wave box (in yellow) is used to generate a plane wave with a propagation direction of $-y$ and a linear polarization parallel to the z-axis. Fictitious currents flow on the surfaces of the plane wave box such that both incident and scattered fields are present inside the box, whereas only the scattered

field is present outside of the box. The reflectarray under simulation is enclosed in the plane wave box. The simulation boundary with absorbing boundary conditions is at a distance from the plane wave box of two times the wavelength of lowest simulation frequency in all axes. The simulation area is meshed with rectangular meshes based on the following rules: at least 15 cells per wavelength of the highest simulation frequency and at least 4 cells per object. The simulation frequency range is between 0.3 THz and 1 THz. A far-field monitor is placed at xz-plane to capture the radiation pattern of the reflectarray under simulation. There are 100 temporal sampling points per period at the highest simulation frequency.

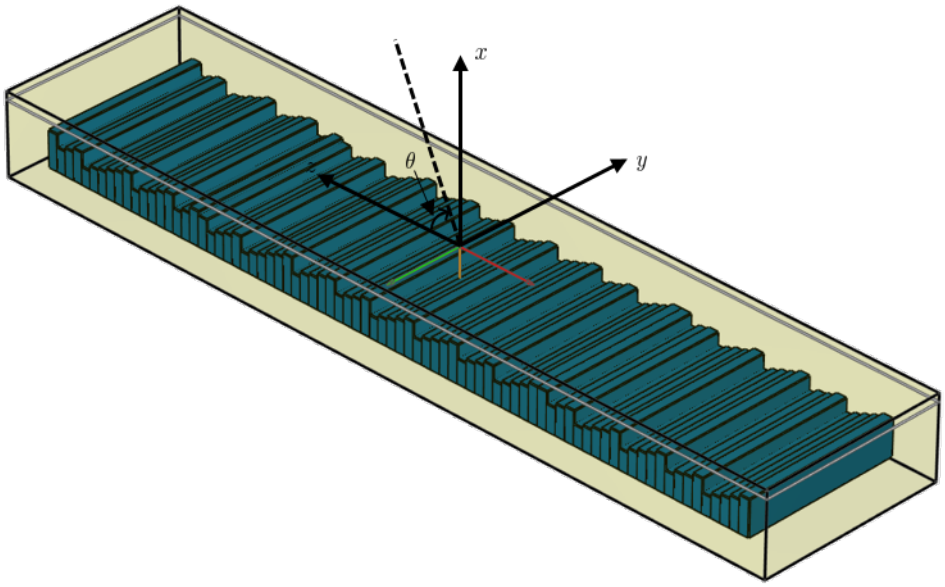

Figure 3.11: EM simulation setup in the FDTD solver EMPIRE XPU for analysing the radiation pattern of the reflectarray.

In section 3.4.3, radiation patterns of 9 different approximate blazed gratings are calculated. For an intuitive comparison between the calculated and simulated radiation patterns, I conduct EM simulations of the same 9 approximate blazed gratings and show their calculated and simulated radiation patterns in Fig. 3.12. For all 9 approximate blazed gratings, the calculated and simulated radiation pattern exhibit an agreement both in main lobe at the desired steering angle and in side lobes as well as the sidelobe levels.

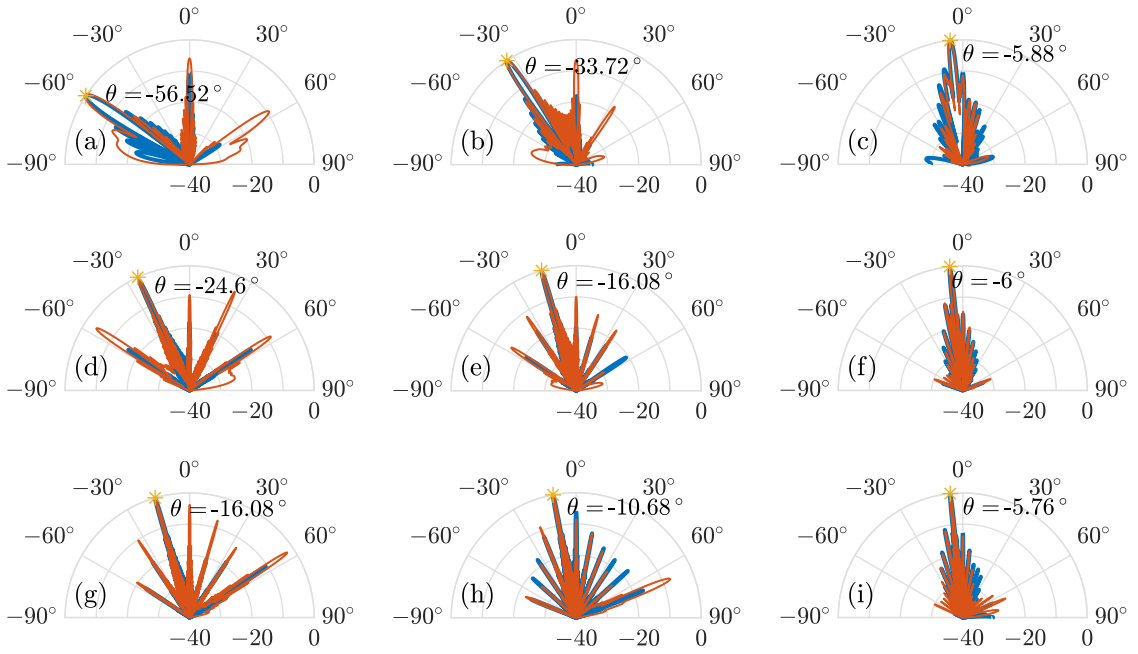

Figure 3.12: Calculated (in blue) and simulated (in red) radiation patterns of the diffraction grating configured for (a) the maximum steering angle at 0.3 THz, (b) the middle of the steering range at 0.3 THz, (c) the minimum steering angle at 0.3 THz, (d) the maximum steering angle at 0.6 THz, (e) the middle of the steering range at 0.6 THz, (f) the minimum steering angle at 0.6 THz, (g) the maximum steering angle at 0.9 THz, (h) the middle of the steering range at 0.9 THz, and (i) the minimum steering angle at 0.9 THz [1].

Due to the finite size of the approximate blazed grating under simulation, the diffracted electric near-field by the grating under simulation is inherently multiplied by a rectangular function. This rectangular function in the near-field corresponds to a sinc function in the far-field region that manifests in the excessive side lobes around the main lobe. According to the theory of antenna arrays and aperture antennas, the directivity of the first side lobe is about 13.46 dB lower than the directivity of the main lobe. The calculated radiation patterns are in excellent agreement with this number. To suppress the sidelobe level while maintaining the main lobe directivity, a tapered amplitude distribution instead of an uniform amplitude distribution of the feeding beam can be used. Even with the approximate blazed grating design, we still observe in both calculated and simulated radiation patterns apparent grating lobes that reduce the radiated power in the desired direction and can cause interference to other communication and

radar systems.

3.5.2 Measured radiation characteristics

To further validate the proposed mathematical model and the beam steering capability of the designed approximate blazed gratings, I conduct the planar and 3D radiation pattern measurements of two reflectarray phantoms, i.e., reflectarrays without the MEMS actuation systems. Fig. 3.13 displays photographs of the two reflectarray phantoms. The reflectarray phantom 1 is an approximate blazed grating whose height profile is designed to have a diffraction angle of 56.4° at 300 GHz. The reflectarray phantom 2 is an approximate blazed grating whose height profile is designed to have a diffraction angle of 41.8° at 300 GHz.

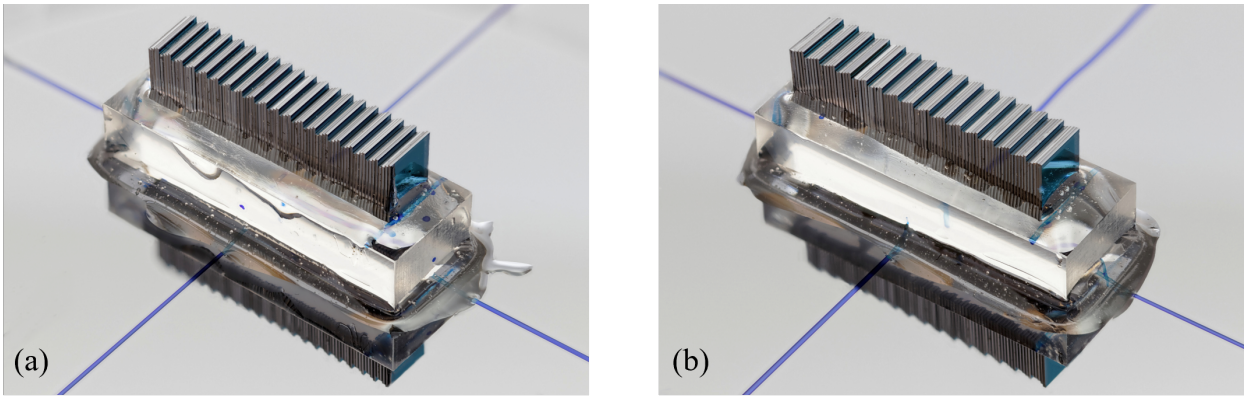

Figure 3.13: (a) Photograph of a reflectarray phantom, an approximate blazed grating with a designed height profile for a diffraction angle of 56.4°. (b) Photograph of a reflectarray phantom, an approximate blazed grating with a designed height profile for a diffraction angle of 41.8° [3].

Planar radiation pattern measurement with a terahertz TDS system

For the planar radiation pattern measurements, a fiber-coupled terahertz time-domain spectroscopy (TDS) system TERA K15 from Menlo Systems is used for terahertz generation and detection. It includes a femtosecond fiber laser at 1550 nm wavelength that has a repetition rate of 100 MHz and pulse duration of less than 90 fs. Its terahertz spectrum typically has a spectral bandwidth of 5.5 THz and a peak dynamic range of

95 dB. The optical delay line provides a long scan range of 1600 ps which corresponds to a spectral resolution of 0.7 GHz.

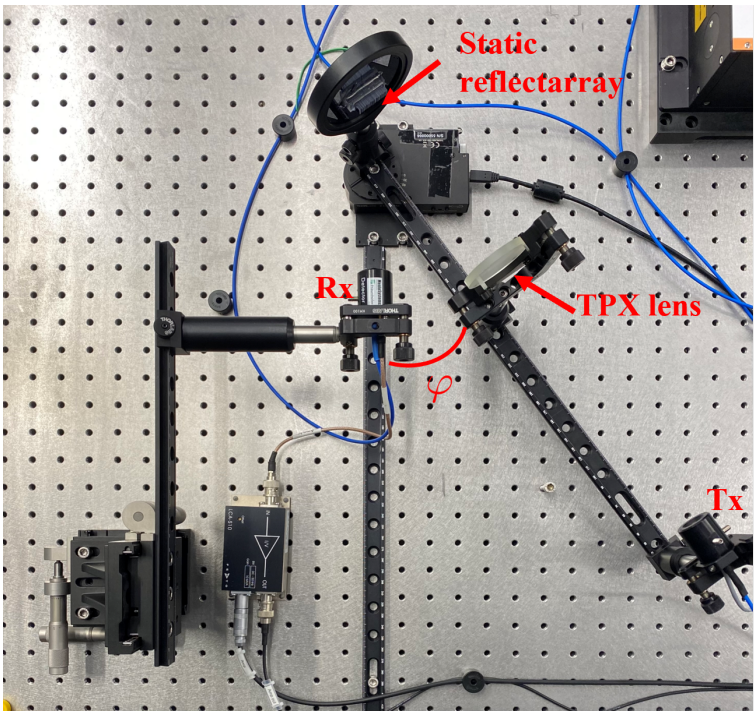

Figure 3.14: Photograph of the planar radiation pattern measurement setup with the fiber-coupled terahertz TDS system [3].

A photograph of the planar radiation pattern measurement setup is shown in Fig. 3.14. The reflectarray phantom is positioned on a motorized rotation stage, while the terahertz receiver (RX) is placed on an $xyz-$stage at a fixed distance from the reflectarray phantom. The transmitted terahertz beam from the terahertz transmitter (TX) is first collimated by a polymethylpentene (TPX) lens before normally incident on the reflectarray phantom. The TPX lens is a plano-convex terahertz lens with a diameter of 2 inch and a long focal length of 250 mm so that the collimated beam can illuminate the entire reflectarray. To ensure a normal incidence as the reflectarray phantom rotates, the terahertz transmitter (TX), TPX lens, and reflectarray phantom are attached on the same rail that is mounted on the motorized rotation stage. The rotation range is set between $\varphi = 15°$ and $\varphi = 65°$ in steps of 0.2°. To improve the signal-to-noise power ratio, the averaged terahertz pulse from 1000 measurements is recorded at each angle. The scan window of the delay line is set to be 200 ps which is sufficient to capture the terahertz

pulse with the adequate frequency resolution. It takes around 5 hours to measure one reflectarray phantom.

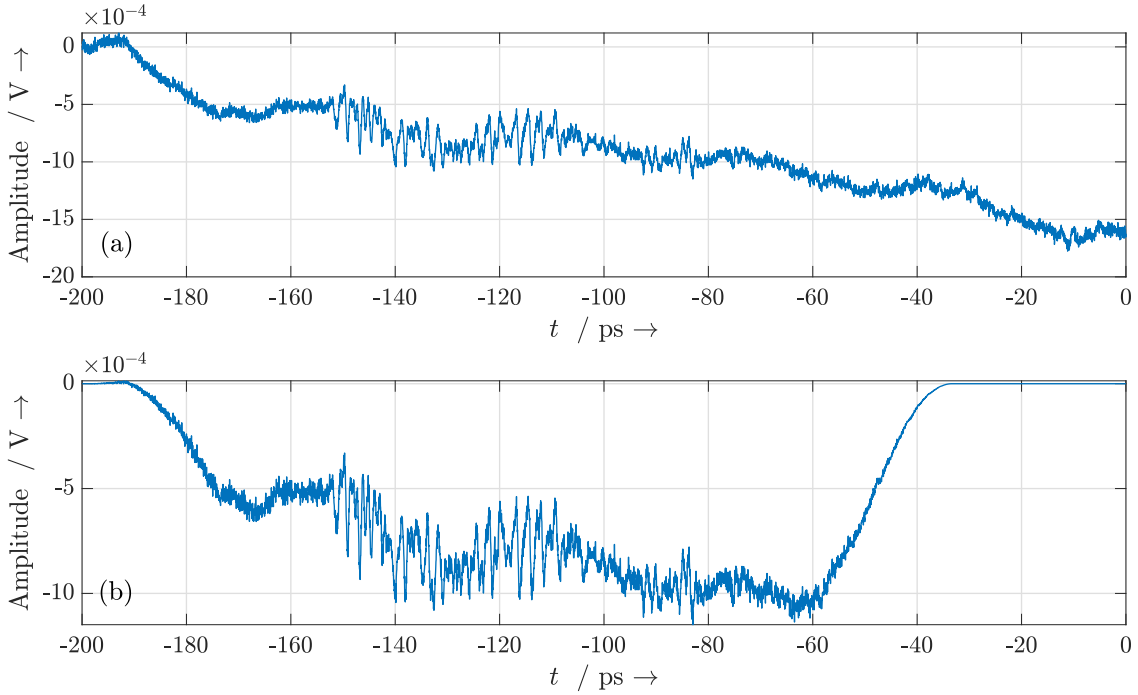

Figure 3.15: (a) The averaged terahertz pulse reflected by a reflectarray phantom, obtained by averaging 1000 measurements. (b) The resulting windowed terahertz pulse after applying a Tukey window to the pulse shown in (a).

For one reflectarray phantom, 251 averaged terahertz time-domain traces, each corresponding to an angle within the rotation range $15° \cdots 65°$, are obtained. Fig. 3.15 depicts the signal processing that is performed on one of the time-domain traces. The acquired raw data, shown in Fig. 3.15(a), represents the tranimpedance-amplified photocurrent, which is directly proportional to the terahertz electric field. The observed decrease in the overall amplitude over time is a result of a slight power variation at the receiver as the delay line is scanned. This variation leads to a gradual change in the photocurrent, resulting in this varying offset over the scan window of the delay line. However, considering that this variation occurs at a relatively slow rate compared to the terahertz signal, offset correction is unnecessary. In the raw trace shown in Fig. 3.15(a), The desired terahertz signal begins around -150 ps and ends around -80 ps. Alongside the desired signal, echoes and spurious signals are observed. In order

to eliminate them while preserving the terahertz pulse, the raw time-domain trace is multiplied by a Tukey window. The resulting windowed time-domain trace is shown in Fig. 3.15(b). The windowed time-domain trace is then zero-padded so that its duration is the same as the temporal pulse spacing of the laser. Finally, the discrete Fourier transform is computed and the spectrum of the diffracted terahertz beam is obtained. The same signal processing steps are performed on all the other time-domain traces.

The calculated and measured radiation patterns for the two reflectarray phantoms at the frequencies between 200 GHz and 800 GHz are shown in Fig. 3.16. The measured radiation patterns exhibit the excellent agreement with the calculated ones for both reflectarray phantoms. From these broadband radiation patterns, we observe a frequency dependence of the main beam direction. Take reflectarray phantom 1 as an example. At the frequencies between 260 GHz to 450 GHz, its main beam approaches the grating's normal vector with the increasing frequency. This can be explained by the grating equation Eq.3.14: with the increasing frequency (decreasing wavelength), the diffraction angle becomes smaller. The second-order diffraction at frequencies between 520 GHz and 800 GHz occurs by further increasing the frequency.

The agreement observed between the calculated and measured broadband radiation patterns of these two reflectarray phantoms serves as validation for the applicability of the proposed mathematical model in calculating the radiation pattern of such reflectarrays.

To assess the beam steering capability of the designed approximate blazed gratings, an analysis of the radiation patterns at the design frequency of 300 GHz is conducted. As shown in Fig. 3.17, at the design frequency of 300 GHz, the measured radiation patterns agree with the calculated ones in terms of the main lobe angle. The maximum angular offset between the calculated and measured main beam is around 2°. It is worth noting that several factors within the measurement setup can contribute to the offset. For example, the transmitted terahertz beam is not incident on the reflectarray phantom normally but with a small incident angle. However, the measured sidelobe level is less satisfactory, i.e. higher than the anticipated sidelobe level by the calculation. The reason is that the terahertz receiver (RX) is placed not quite in the far-field to ensure a sufficient dynamic range for the measurements.

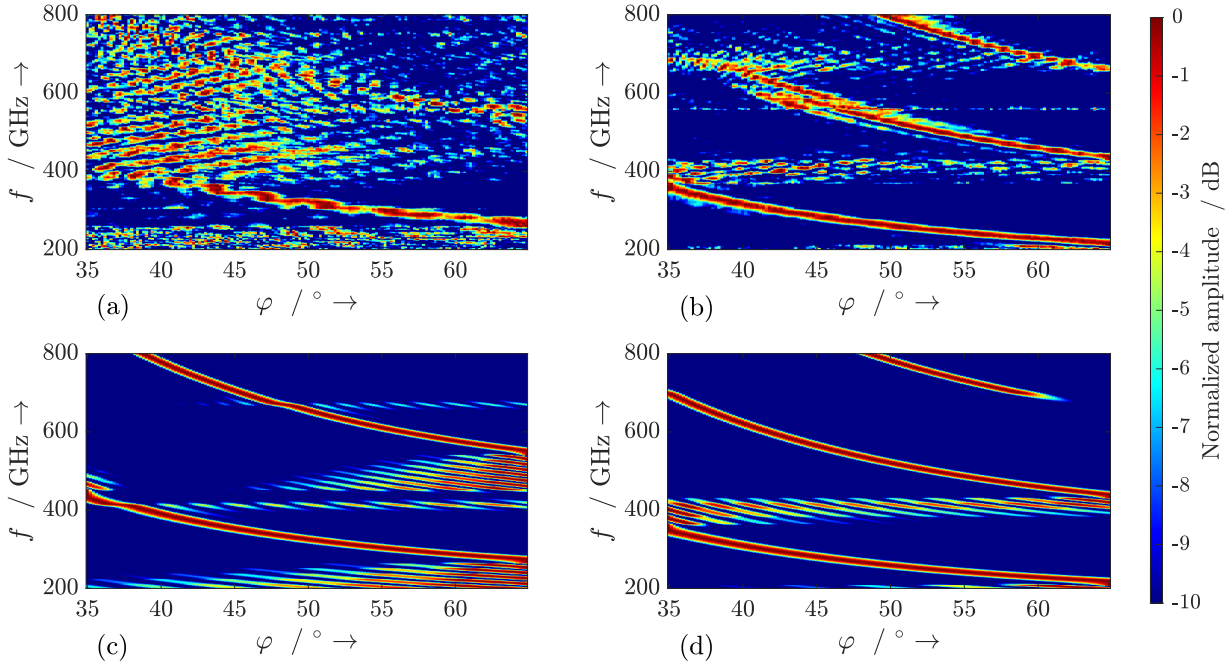

Figure 3.16: (a) Measured and (c) calculated radiation patterns of the reflectarray phantom 1 for the frequencies between 200 GHz and 800 GHz at the angles between 35° and 65°. (b) Measured and (d) calculated radiation patterns of the reflectarray phantom 2 for the frequencies between 200 GHz and 800 GHz at the angles between 35° and 65° [3].

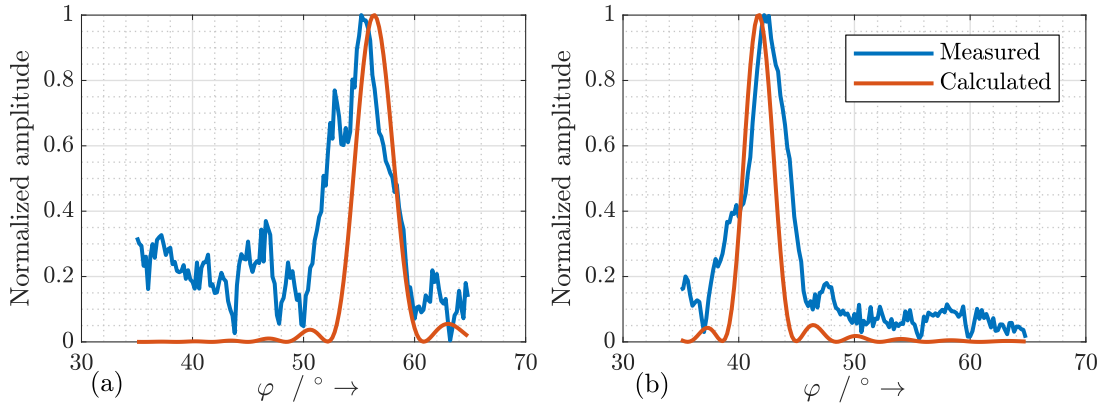

Figure 3.17: Measured (in blue) and calculated (in red) radiation pattern of (a) the reflectarray phantom 1 and (b) the reflectarray phantom 2 for the frequency of 300 GHz at the angles between 35° and 65° [3].

3D radiation pattern measurement with a terahertz FDS system

A motorized spherical measurement system is utilized to measure the 3D radiation patterns of the reflectarray phantoms as shown in Fig. 3.18. It has a fully hemispherical coverage: $0^\circ \cdots 360^\circ$ in azimuth and $0^\circ \cdots 90^\circ$ in elevation. The reflectarray phantom is attached on a rail and its center is located at the origin of the spherical measurement system. The terahertz transmitter (TX) is mounted on the same rail, facing the center of the reflectarray phantom. The terahertz receiver (RX) is mounted on an arch frame, revolving around the center of the reflectarray phantom during the measurement. Compared with the planar radiation pattern measurement setup described in section 3.5.2, the collimating lens is removed for this measurement setup. The reason is that the lens cannot be accommodated while ensuring that the center of the reflectarray phantom is located at the origin of the spherical measurement setup. Consequently, the incident terahertz beam illuminating the reflectarray phantom cannot be considered a strictly plane wave. The measured 3D radiation pattern therefore cannot be interpreted quantitatively. However, with the measured 3D radiation patterns of the reflectarray phantoms, we can still observe the grating lobes locating at the opposing site of the grating's normal vector and the relative difference between the azimuth and elevation beam widths.

To cover as much hemisphere as possible without the collisions between the components, the elevation angle θ is set between 15° and 65°, and the azimuth angle φ is set between -130° and 130°. The radiation pattern of the reflectarray has a stronger angular dependence in elevation than in azimuth. Therefore, I choose a fine step size of 0.25° in elevation and a sparse step size of 2° in azimuth. This gives in total 26000 angular points to measure. The measurement duration for a single reflectarray phantom would be around 35 days if the terahertz TDS system utilized in the planar radiation pattern measurement was used. Here, I employ a terahertz frequency-domain spectroscopy (FDS) system TeraScan 1550 from TOPTICA PHOTONICS for the terahertz generation and detection, operating in the sampling mode at the design frequency of 300 GHz, to drastically reduce the measurement time.

The measured 3D radiation patterns of the two reflectarray phantoms at the design frequency of 300 GHz are shown in Fig. 3.19. Both reflectarray phantoms exhibit strong reflections between $\theta = 15^\circ \cdots 35^\circ$. This is caused by the specular reflection of the

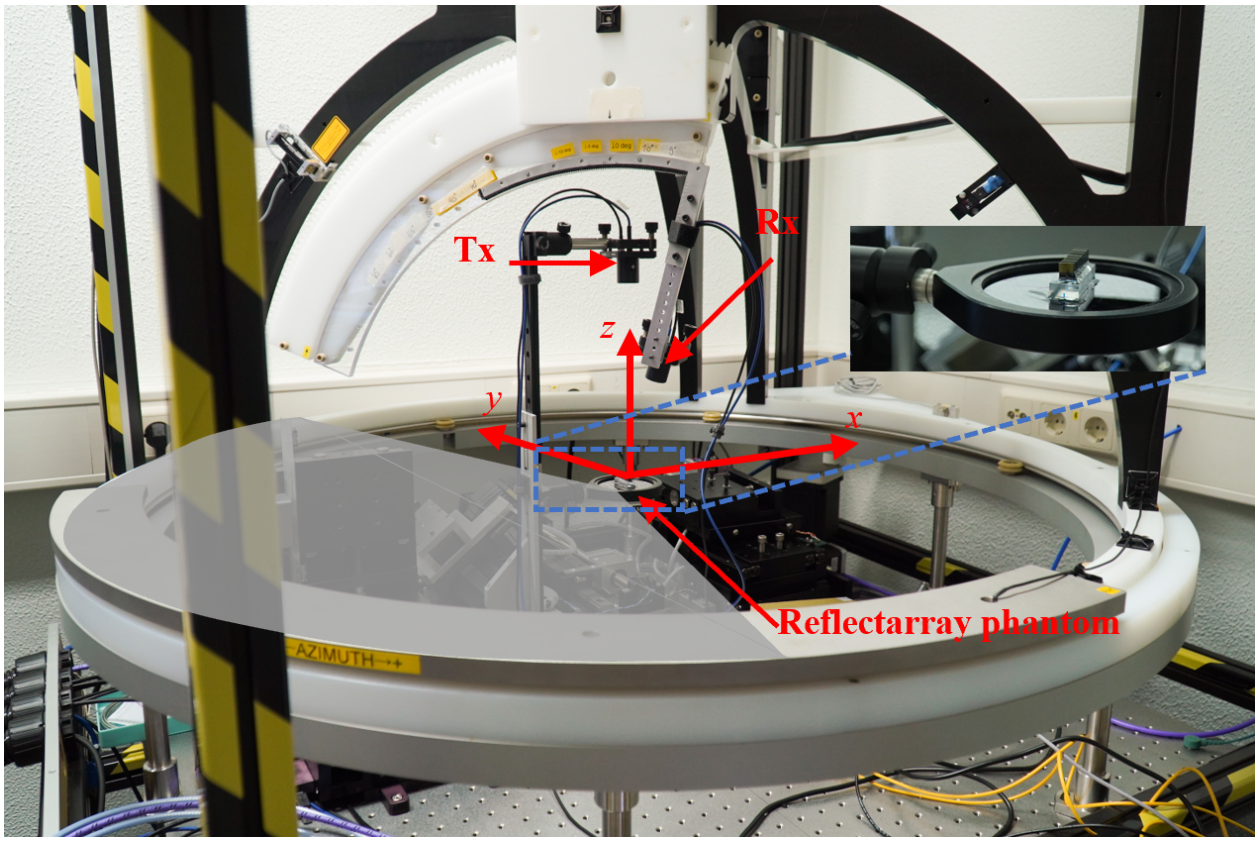

Figure 3.18: Photograph of the 3D radiation pattern measurement setup with the terahertz FDS system (gray shaded area is not measured) [3].

divergent terahertz beam on the 3 inch silicon wafer on which the reflectarray phantom is adhered. At $\varphi = 0°$, the polarizations of the terahertz transmitter (TX) and receiver (RX) are orthogonal. This leads to a total polarization mismatch, a null around $\varphi = 0°$ is therefore observed for both reflectarray phantoms. In addition to the main beams at the designed diffraction angles of 56.4° for phantom 1 and 41.8° for phantom 2, the grating lobes on the opposing side ($\varphi = -90°$) of the grating's normal vector appear as expected. The measured 3 dB beam widths in elevation and azimuth are around 5° and 12°, respectively. The reflectarray phantoms have a narrower 3 dB beam width in elevation than in azimuth which is consistent with the expectation. This is due to the reflectarray having a larger electrical size in the elevation plane than in the azimuth plane.

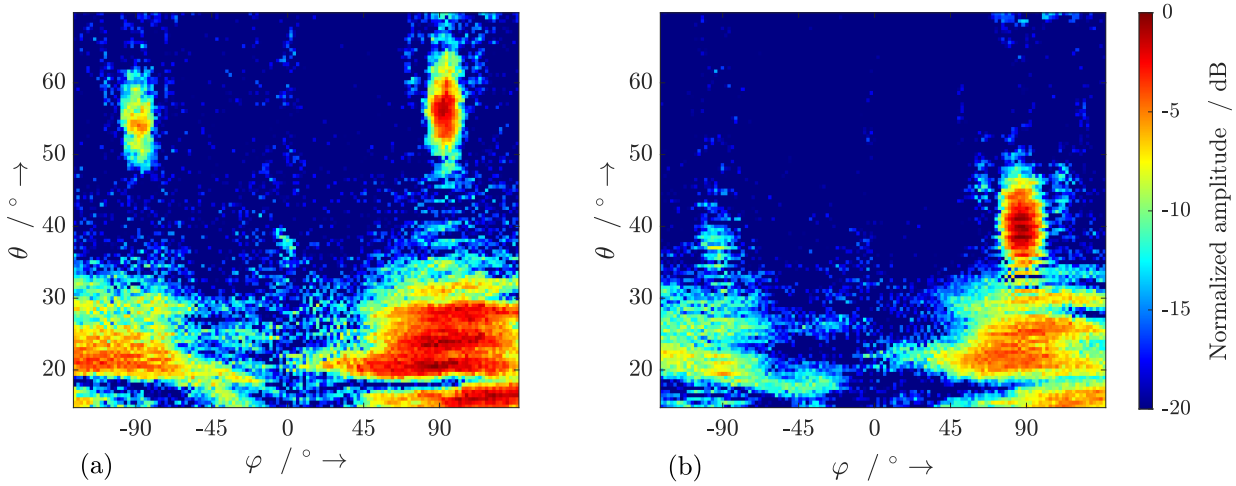

Figure 3.19: Measured 3D radiation pattern of (a) the reflectarray phantom 1 and (b) the reflectarray phantom 2 for the elevation angle θ between 15° and 65° and azimuth angle φ between −130° and 130° [3].

CHAPTER

FOUR

MEMS-BASED REFLECTARRAY CONFIGURED BY A GENETIC ALGORITHM FOR TERAHERTZ BEAM STEERING

In the previous chapter, I demonstrated the feasibility of using an approximate blazed grating for terahertz beam steering. This is a simple configuration of a reflectarray, and the shape of the approximate blazed grating can be easily determined from the grating equation with the knowledge of the predefined steering angle. However, deploying such approximate blazed gratings in beam steering systems still encounters some limitations and drawbacks, such as limited steering range, inability to steer continuously, and the appearance of grating lobes. Therefore, it is desirable to explore other configurations of the reflectarray.

Let us first review the situation we are facing here. The reflectarray comprises 80 reflective elements. Each reflective element is actuated with an independent MEMS actuation systems and can settle on 2^5 vertical positions. In total, the reflectarray has $2^{5\cdot 80}$ possible configurations. For such a large search space, an optimization algorithm can be used to find a feasible optimal solution.

Here, I configure the MEMS-based reflectarray using a genetic algorithm (GA). A GA is one of the evolution algorithms that mimic the evolution process in the nature. It

starts by choosing an initial population with random chromosomes in the search pool. The offspring is then produced by the process of crossover, mutation, and migration. The GA follows the basic evolution rule "survival of the fittest". The fittest is defined and assessed by a so-called fitness function which describes the objective of an optimization.

In this chapter, I first discuss a single-objective optimization problem with three different objectives, each of which corresponds to one of the desired characteristics of the reflectarray's radiation pattern: maximizing the directivity at a given angle, minimizing the sidelobe level, and nulling in a specific direction. Based on the results of the single-objective optimizations, I further analyze the trade-off between the above objectives and illustrate the results in the form of a Pareto front. Finally, a comparison between the approximate blazed grating and the reflectarray optimized by a GA is carried out by studying their measured radiation patterns.

4.1 Single-objective optimization

In general, a single-objective optimization without constraints can be mathematically formulated as follows:

$$\text{Minimize: } f(\boldsymbol{x}). \tag{4.1}$$

In a GA, $f(\boldsymbol{x})$ is the fitness function that evaluates each individual within the population for every iteration (generation). $\boldsymbol{x}$ is the vector of design variables, $\boldsymbol{x} = [h_1, h_2, \cdots, h_N]$, where N is the total number of the design variables.

In this optimization problem, the design variables are the heights of 80 reflective elements. Therefore, the vector of design variables can be written as $\boldsymbol{x} = [h_1, h_2, \cdots, h_{80}]$. Each reflective element is driven by an independent 5-bit MEMS-actuation system in the range of $0 \cdots 600\,\mu$m. This imposes two constraints on the design variables: a discrete constraint and a bound constraint. For simplicity, I first consider the optimization problem as a continuous optimization and then round the results to the nearest feasible discrete position. Later in this section, I demonstrate with an example, that rounding the results has no noticeable impact on the radiation pattern of the reflectarray. Thus, it is only necessary to consider the bound constraint imposed on the design variables,

Table 4.1: Options for the single-objective GA [3].

Size of the population	200
Creation of the initial population	The initial population is created with a uniform distribution
Maximum number of generations	8000
Number of elite	10
Mutation option	Adaptive
Crossover option	Scattered
Crossover fraction	0.8
Stopping criteria	Average cumulative change in value of the fitness function over 50 generations is less than 10^{-6}

which can be formulated as:

$$0\,\mu\text{m} \leq h_i \leq 600\,\mu\text{m}, \quad i = 1, 2, \cdots, 80. \tag{4.2}$$

In this work, single-objective optimizations using a GA implemented in Matlab are carried out. The options employed for the single-objective GA are outlined in Table 4.1. The generation-to-generation evolution, as depicted in Fig. 4.1, is used illustrate operational mechanism of the GA under the specific options.

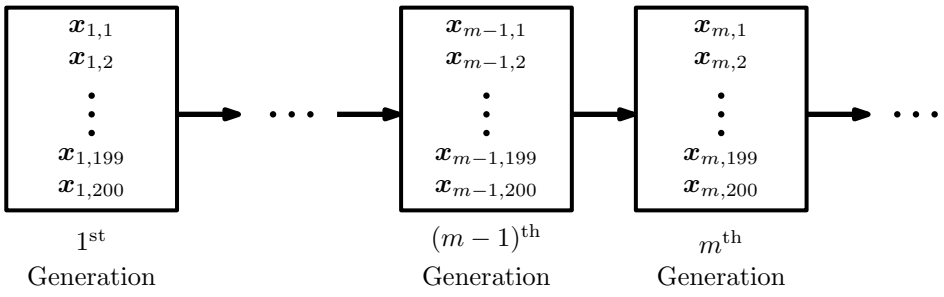

Figure 4.1: Generation-to-generation evolution within a GA.

Each generation, as determined by the "size of the population" specified in Table 4.1, consists of 200 individuals. Within the m^{th} generation, 10 individuals are elite offspring, i.e., they are the direct replication from the $(m-1)^{\text{th}}$ generation without any changes, as described by the equation:

$$\boldsymbol{x}_{m,n} = \boldsymbol{x}_{m-1,n}. \tag{4.3}$$

As specified by the "crossover fraction" outlined in Table 4.1, the 80% of the remaining population in the m^{th} generation, which is $(200 - 10) \cdot 0.8 = 152$ individuals, is generated through the crossover operation. The specific crossover technique employed here is the scattered crossover. Fig. 4.2 visually represents the creation of a crossover offspring. For this process, two individuals from the $(m-1)^{\text{th}}$ generation are selected as parent 1 and parent 2. Additionally, a random binary vector of 80 elements, denoted as $\boldsymbol{c}$, is generated. The resulting offspring inherits the genes from parent 1 when the corresponding vector element is 1, and from parent 2 when the element is 0.

Parent 1	$\boldsymbol{x}_{m-1,i} = [h_{m-1,i,1}, h_{m-1,i,2}, h_{m-1,i,3}, \cdots, h_{m-1,i,79}, h_{m-1,i,80}]$
Parent 2	$\boldsymbol{x}_{m-1,j} = [h_{m-1,j,1}, h_{m-1,j,2}, h_{m-1,j,3}, \cdots, h_{m-1,j,79}, h_{m-1,j,80}]$
Binary vector	$\boldsymbol{c}_{m,i} = [1, 1, 0, \cdots, 0, 1]$
Offspring	$\boldsymbol{x}_{m,i} = [h_{m-1,i,1}, h_{m-1,i,2}, h_{m-1,j,3}, \cdots, h_{m-1,j,79}, h_{m-1,i,80}]$

Figure 4.2: Illustration of a crossover offspring generated through the scattered crossover operation.

The remaining 38 individuals in the m^{th} generation are mutation offspring. Given the existence of the bound constraints, an adaptive mutation strategy is implemented. The resulting mutation offspring is generated by adding the parent vector to a scaled direction vector, as expressed by:

$$\boldsymbol{x}_{m,k} = \boldsymbol{x}_{m-1,k} + \boldsymbol{l} \odot \boldsymbol{d}. \tag{4.4}$$

Here, the $\boldsymbol{l}$ is the step length vector, representing the mutation magnitude, and $\boldsymbol{d}$ denotes the mutation direction. The adaptability of the mutation depends on the performance of the previous generation. If an individual from the previous generation has a successful performance, the mutation is kept minimal to explore the surrounding area. Conversely, in case of suboptimal performance, a larger mutation is applied to facilitate exploration.

For most of the terahertz beam steering applications, at least one of the following features is desirable:

- being able to steer the main beam in an arbitrary direction with a high directivity and narrow beam width in order to compensate for the low transmit power of the terahertz system, the large free space loss, and the high atmospheric absorption of the terahertz radiation,
- a low sidelobe level,
- and a steerable null to mitigate an interferer while maintaining the main beam direction.

With the help of the proposed mathematical model, these features can be formulated mathematically by defining the fitness function $f(\boldsymbol{x})$. In this section, one or more fitness functions $f(\boldsymbol{x})$ are formulated to describe three different objectives mentioned above. If more than one fitness function are applied to the same objective, their performances are compared.

4.1.1 Maximizing the directivity at a given angle

The first feature mentioned above can be treated as an optimization problem involving maximizing the directivity at a given angle. For this objective, three different fitness functions are proposed.

Note that the GA implemented in Matlab finds the minimum of the fitness function. Therefore, the first proposed fitness function for the objective of maximizing the directivity at a given angle is simply the reciprocal of the directivity at the target angle $D(\theta = \theta_{\text{target}})$

$$f_{D,1} = \frac{1}{D(\theta = \theta_{\text{target}})}. \tag{4.5}$$

This fitness function guides the GA to maximize the directivity at the target angle without satisfying any predefined value.

Now, I take the directivity of a uniform linear array of the isotropic radiators at the target angle as a reference. The properties of the uniform linear array are as follows:

- the length of the linear array of the isotropic radiators is the same as the reflectarray, which is $l = 300\,\mu\text{m} \cdot 80 = 24\,\text{mm}$,

- the element spacing between the adjacent radiators is smaller than half of the wavelength at the operating frequency.

The following two fitness functions guide the GA to bring the directivity of the reflectarray at the target angle $D(\theta = \theta_{\text{target}})$ close to this reference directivity $D_{\text{ULA}}(\theta = \theta_{\text{target}})$.

$$f_{D,2} = \left(D(\theta = \theta_{\text{target}}) - D_{\text{ULA}}(\theta = \theta_{\text{target}})\right)^2 \text{ and} \tag{4.6}$$

$$f_{D,3} = 1 - \exp\left(-\frac{\left(D(\theta = \theta_{\text{target}}) - D_{\text{ULA}}(\theta = \theta_{\text{target}})\right)^2}{2 \cdot 240^2}\right). \tag{4.7}$$

The fitness functions $f_{D,2}$ and $f_{D,3}$ reach the minimum, i.e., 0, when the directivity of the reflectarray at the target angle $D(\theta = \theta_{\text{target}})$ is equal to the reference directivity $D_{\text{ULA}}(\theta = \theta_{\text{target}})$.

Before presenting and comparing the optimization results of these three fitness functions. I first demonstrate through an optimization example that applying a discrete constraint is not necessary. A continuous GA optimization is performed with the objective of maximizing the directivity of the refelctarray at 45° at 300 GHz using the fitness function $f_{D,1}$. The radiation pattern of the reflectarray, where the heights of the 80 reflective elements are the direct output of the continuous optimization, is shown in blue in Fig. 4.3. The radiation pattern of the reflectarray, where the heights of the 80 reflective element take the next feasible values by rounding the output of the continuous optimization, is shown in red in Fig. 4.3. As observed, there are almost no variations in the two radiation patterns in terms of the main lobe and side lobes positions, with only slight directivity variations that can be neglected. Therefore, in the following chapter, optimizations are carried out without the discrete constraint for the simplicity.

Now, I present an optimization instance using these three fitness functions. The optimization objective is to maximize the directivity of the reflectarray in the direction of 45° at the frequency of 300 GHz. Three independent runs of GA with the fitness function $f_{D,1}$, $f_{D,2}$, and $f_{D,3}$ are carried out. The calculated and EM simulated radiation patterns of the three reflectarrays, each of which is obtained by the GA with one of the three fitness functions, are shown in Fig. 4.4. All three obtained reflectarrays successfully steer the beam in the target direction of 45° with a directivity approximately 16.7 dBi and sidelobe level of around -13 dB.

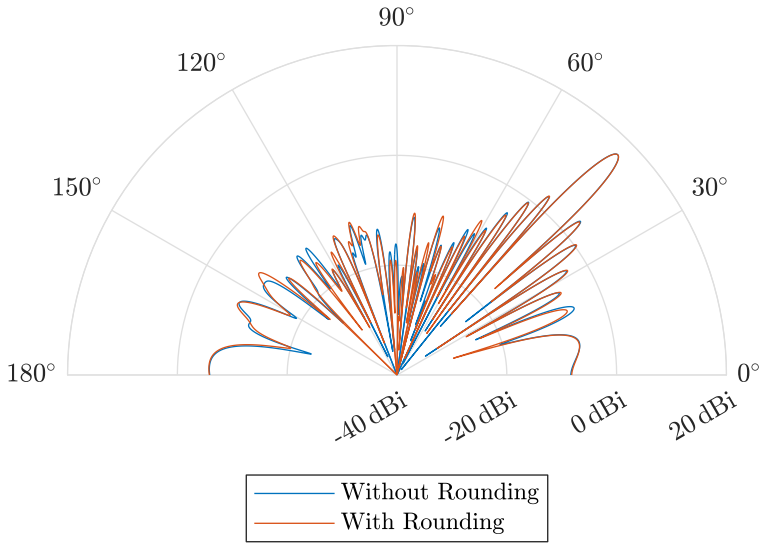

Figure 4.3: Radiation pattern of the reflectarray at 300 GHz, illustrating the comparison between two scenarios: one where the heights of the 80 reflective element are the direct output of a continuous optimization (in blue) and the other where these heights take the next feasible values by rounding the output of a continuous optimization (in red).

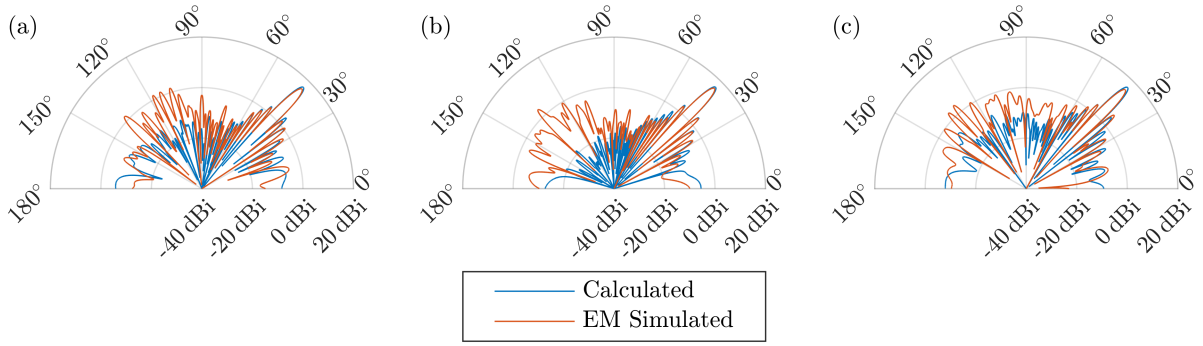

Figure 4.4: Radiation pattern of the reflectarray at 300 GHz, showing the comparison between calculated (in blue) and EM simulated (in red) results. The reflectarray's height profile is optimized using a GA to maximize the directivity in the direction of 45°. Three different fitness functions are employed: (a) $f_{D,1}$, (b) $f_{D,2}$, and (c) $f_{D,3}$ [3].

Note that for each execution, the GA returns a slightly different optimization result despite using the same machine, fitness function, algorithm's settings. This is because of its intrinsic randomness. For a fair comparison of the optimization performances for these three fitness functions, 20 runs of the GA for each fitness function are con-

Table 4.2: Averaged directivity D_{avg}, sidelobe level SLL_{avg}, 3 dB beam width θ_{3dB}, runtime t_{avg}, and standard deviation σ of the 20 resulting directivities over 20 optimization runs using the enlisted fitness functions [3].

	$f_{\text{D},1}$	$f_{\text{D},2}$	$f_{\text{D},3}$
D_{avg}	16.78 dBi	16.82 dBi	16.67 dBi
SLL_{avg}	-12.96 dB	-13.10 dB	-12.79 dB
θ_{3dB}	2.97°	2.98°	2.97°
t_{avg}	7 min	126 min	3 min
σ	0.066 dB	0.044 dB	0.063 dB

ducted. The average maximum directivity D_{avg}, sidelobe level SLL_{avg}, 3 dB beam width $\theta_{\text{3dB,avg}}$, runtime t_{avg}, and the standard deviation σ of the 20 resulting directivities are summarized in Table 4.2. In terms of the directivity, sidelobe level, and 3 dB beam width, there are no distinct differences between those three fitness functions. The fitness function $f_{D,2}$ gives a slightly better directivity, but at the cost of a drastic increase in runtime.

4.1.2 Minimizing the sidelobe level

Another desired feature in the radiation pattern of an antenna array: a low sidelobe level, can be formulated as an optimization problem with the objective of finding the minimum sidelobe level.

The sidelobe level is defined as a ratio of the directivity at the peak of the main lobe θ_{ML} to the directivity at the peak of the highest sidelobe $\theta_{\text{SL,highest}}$

$$\gamma_{\text{SLL}} = \frac{D\left(\theta = \theta_{\text{SL,highest}}\right)}{D\left(\theta = \theta_{\text{ML}}\right)}. \tag{4.8}$$

The first proposed fitness function for the objective of minimizing the sidelobe level is simply the definition of the sidelobe level $f_{\text{SLL},1} = \gamma_{\text{SLL}}$. This fitness function guides the GA to minimize the sidelobe level without satisfying any predefined value.

To test the optimization performance of the fitness function $f_{\text{SLL},1}$, I run the GA optimization with this fitness function 20 times, calculate the average sidelobe level and list it in Table 4.3. Comparing to the average sidelobe level in the previous section, this

fitness function is able to achieve the optimization goal by suppressing the sidelobe level of around 1 dB. However, this change is not very significant. To further suppress the sidelobe level, I introduce two additional fitness functions.

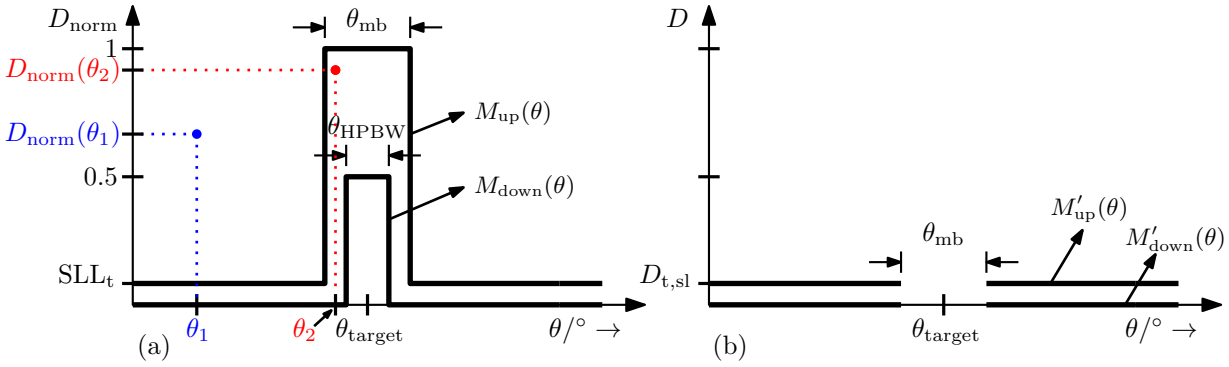

Figure 4.5: Illustration of masks employing in the fitness function (a) $f_{\text{SLL},2}$ and (b) $f_{\text{SLL},3}$ [3].

The second fitness function $f_{\text{SLL},2}$ for the objective of minimizing the sidelobe level is defined by the mask-based method proposed by Sheikholeslami and Atlasbaf [109]. This fitness function guides the GA to restrict the normalized radiation pattern $D_{\text{norm}}(\theta) = \dfrac{D(\theta)}{D(\theta_{\text{target}})}$ of the reflectarray to the region bounded by the upper mask $M_{\text{up}}(\theta)$ and the lower mask $M_{\text{down}}(\theta)$ as illustrated in Fig. 4.5(a). We can change the shapes of the masks and subsequently obtain the desired radiation pattern by setting the following parameters

- θ_{target} defines the angle at the peak of the main lobe,
- θ_{mb} defines the angle difference between the diametrically opposed nulls around the peak of the main lobe,
- θ_{HPBW} defines the half-power beam width of the main lobe,
- and SLL_t determines the target sidelobe level

The fitness function is defined as follows

$$f_{\text{SLL},2} = \sum_{l=0}^{M} \Big(\big(M_{\text{up}}(\theta_l) - D_{\text{norm}}(\theta_l)\big) \cdot \big(M_{\text{down}}(\theta_l) - D_{\text{norm}}(\theta_l)\big) + \big|M_{\text{up}}(\theta_l) - D_{\text{norm}}(\theta_l)\big| \cdot \big|M_{\text{down}}(\theta_l) - D_{\text{norm}}(\theta_l)\big| \Big). \tag{4.9}$$

To understand the functionality of fitness function $f_{\mathrm{SLL},2}$, two arbitrary points shown in Fig. 4.5(a) are considered: one at $(\theta_1, D_{\mathrm{norm}}(\theta_1))$ is positioned above the upper mask $M_{\mathrm{up}}(\theta_1)$, leading to $D_{\mathrm{norm}}(\theta_1) > M_{\mathrm{up}}(\theta_1) > M_{\mathrm{down}}(\theta_1)$. Under this condition, Eq. 4.9 is further simplified as:

$$\begin{aligned} f_{\mathrm{SLL},2} = \sum_{\theta_1}^{\theta_1} \Big(& \big(M_{\mathrm{up}}(\theta_l) - D_{\mathrm{norm}}(\theta_l)\big) \cdot \big(M_{\mathrm{down}}(\theta_l) - D_{\mathrm{norm}}(\theta_l)\big) \\ & + \big|M_{\mathrm{up}}(\theta_l) - D_{\mathrm{norm}}(\theta_l)\big| \cdot \big|M_{\mathrm{down}}(\theta_l) - D_{\mathrm{norm}}(\theta_l)\big| \Big) \\ & = -\big|M_{\mathrm{up}}(\theta_1) - D_{\mathrm{norm}}(\theta_1)\big| \cdot -\big|M_{\mathrm{down}}(\theta_1) - D_{\mathrm{norm}}(\theta_1)\big| \\ & + \big|M_{\mathrm{up}}(\theta_1) - D_{\mathrm{norm}}(\theta_1)\big| \cdot \big|M_{\mathrm{down}}(\theta_1) - D_{\mathrm{norm}}(\theta_1)\big| \\ & = 2\big|M_{\mathrm{up}}(\theta_1) - D_{\mathrm{norm}}(\theta_1)\big| \cdot \big|M_{\mathrm{down}}(\theta_1) - D_{\mathrm{norm}}(\theta_1)\big| > 0. \end{aligned} \tag{4.10}$$

Meanwhile, the other point $(\theta_2, D_{\mathrm{norm}}(\theta_2))$ locates between the upper mask $M_{\mathrm{up}}(\theta_2)$ and lower mask $M_{\mathrm{down}}(\theta_2)$, resulting in $M_{\mathrm{up}}(\theta_2) > D_{\mathrm{norm}}(\theta_2) > M_{\mathrm{down}}(\theta_2)$. Under this condition, Eq. 4.9 is further simplified as:

$$\begin{aligned} f_{\mathrm{SLL},2} = \sum_{\theta_2}^{\theta_2} \Big(& \big(M_{\mathrm{up}}(\theta_l) - D_{\mathrm{norm}}(\theta_l)\big) \cdot \big(M_{\mathrm{down}}(\theta_l) - D_{\mathrm{norm}}(\theta_l)\big) \\ & + \big|M_{\mathrm{up}}(\theta_l) - D_{\mathrm{norm}}(\theta_l)\big| \cdot \big|M_{\mathrm{down}}(\theta_l) - D_{\mathrm{norm}}(\theta_l)\big| \Big) \\ & = \big|M_{\mathrm{up}}(\theta_2) - D_{\mathrm{norm}}(\theta_2)\big| \cdot -\big|M_{\mathrm{down}}(\theta_2) - D_{\mathrm{norm}}(\theta_2)\big| \\ & + \big|M_{\mathrm{up}}(\theta_2) - D_{\mathrm{norm}}(\theta_2)\big| \cdot \big|M_{\mathrm{down}}(\theta_2) - D_{\mathrm{norm}}(\theta_2)\big| \\ & = 0. \end{aligned} \tag{4.11}$$

A more general conclusion can be drawn from these two observations: for all points positioned above the upper mask, $f_{\mathrm{SLL},2}$ yields a positive value, while points between the upper and lower masks result in $f_{\mathrm{SLL},2}$ returning 0. This implies that once the normalized radiation pattern $D_{\mathrm{norm}}(\theta)$ completely lies in the region bounded by the masks, the fitness function $f_{\mathrm{SLL},2}$ reaches its minimum, i.e., 0.

The third fitness function $f_{\mathrm{SLL},3}$ is similar to the $f_{\mathrm{SLL},2}$. Instead of defining a sidelobe level as in the $f_{\mathrm{SLL},2}$, an absolute directivity $D_{\mathrm{t}}(\theta_{\mathrm{sl}})$ to the sidelobes is assigned as illustrated in Fig. 4.5(b). In addition, a gap with a width of θ_{mb} is introduced to exclude

the characteristic of the main lobe. The fitness function is defined as follows:

$$
\begin{aligned}
f_{\mathrm{SLL},3} = \sum_{l=0}^{M} \Big(& \Big(M'_{\mathrm{up}}(\theta_l) - D(\theta_l) \Big) \cdot \big(M'_{\mathrm{down}}(\theta_l) - D(\theta_l) \big) \\
& + \Big| M'_{\mathrm{up}}(\theta_l) - D(\theta_l) \Big| \cdot \big| M'_{\mathrm{down}}(\theta_l) - D(\theta_l) \big| \Big) \\
& + \sum_{l=N}^{N+M} \Big(\Big(M'_{\mathrm{up}}(\theta_l) - D(\theta_l) \Big) \cdot \big(M'_{\mathrm{down}}(\theta_l) - D(\theta_l) \big) \\
& + \Big| M'_{\mathrm{up}}(\theta_l) - D(\theta_l) \Big| \cdot \big| M'_{\mathrm{down}}(\theta_l) - D(\theta_l) \big| \Big).
\end{aligned}
\tag{4.12}
$$

Here the first summation covers all the discrete angles from 0° to $\theta_{\mathrm{target}} - \frac{\theta_{\mathrm{mb}}}{2}$, and the second summation covers all the discrete angles from from $\theta_{\mathrm{target}} + \frac{\theta_{\mathrm{mb}}}{2}$ to π.

I now present an optimization example using these three fitness functions for the objective of minimizing the sidelobe level. A plane wave with the frequency of 300 GHz is normally incident on the reflectarray and the following values are assigned to the parameters of the masks used in the fitness functions $f_{\mathrm{SLL},2}$ and $f_{\mathrm{SLL},3}$

- $\theta_{\mathrm{mb}} = 6^\circ$
- $\theta_{\mathrm{HPBW}} = 3^\circ$
- $\theta_{\mathrm{target}} = 45^\circ$
- $\mathrm{SLL_t} = -18\,\mathrm{dB}$
- $D_{\mathrm{t,sl}} = -3\,\mathrm{dBi}$.

By independent GA optimizations the fitness function $f_{\mathrm{SLL},1}$, $f_{\mathrm{SLL},2}$, and $f_{\mathrm{SLL},3}$ are minimized. The calculated and EM simulated radiation patterns of the obtained reflectarrays are shown in Fig. 4.6. An evident side lobe suppression is observed from all three radiation patterns. To have a quantitative comparison among those three fitness functions, 20 GA optimization runs for each fitness function are performed. The average maximum directivity D_{avg}, sidelobe level $\mathrm{SLL_{avg}}$, 3 dB beam width $\theta_{\mathrm{3dB,avg}}$, runtime t_{avg}, and the standard deviation σ of the 20 resulting directivities are summarized in Table 4.3. Comparing Table 4.3 to Table 4.2, all three fitness functions $f_{\mathrm{SLL},1}$, $f_{\mathrm{SLL},2}$, and $f_{\mathrm{SLL},3}$ are able to suppress the sidelobe level but at the expense of a directivity degradation at the target angle. The fitness function $f_{\mathrm{SLL},3}$ exhibits the best optimization performance by having the lowest sidelobe level, but requires the most runtime.

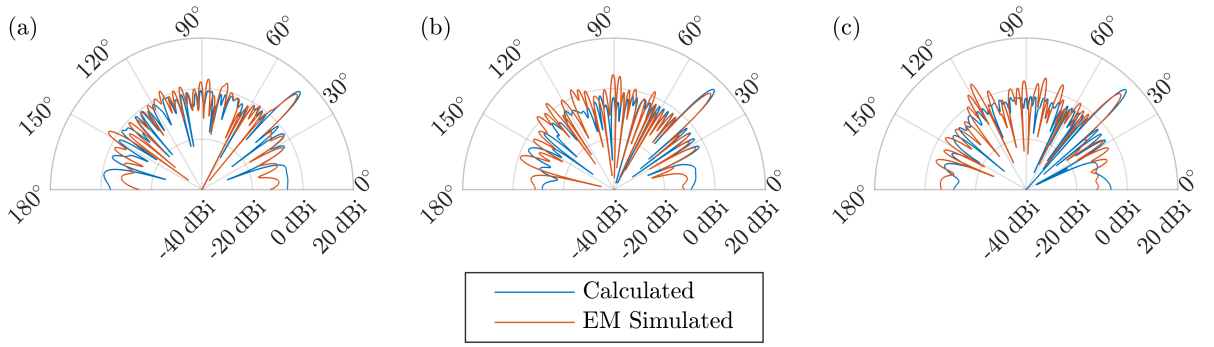

Figure 4.6: Radiation pattern of the reflectarray at 300 GHz, showing the comparison between calculated (in blue) and EM simulated (in red) results. The reflectarray's height profile is optimized using a GA to minimize the sidelobe level as the main beam points in the direction of 45°. Three different fitness functions are employed: (a) $f_{\mathrm{SLL},1}$, (b) $f_{\mathrm{SLL},2}$, and (c) $f_{\mathrm{SLL},3}$ [3].

Table 4.3: Averaged directivity D_{avg}, sidelobe level $\mathrm{SLL}_{\mathrm{avg}}$, 3 dB beam width $\theta_{3\mathrm{dB}}$, execution time t_{avg}, and standard deviation σ of the resulting directivities over 20 simulation runs carried out by a GA using the enlisted fitness functions [3].

	$f_{\mathrm{SLL},1}$	$f_{\mathrm{SLL},2}$	$f_{\mathrm{SLL},3}$
D_{avg}	14.44 dBi	15.83 dBi	15.71 dBi
$\mathrm{SLL}_{\mathrm{avg}}$	-14.08 dB	-17.51 dB	-18.4 dB
$\theta_{3\mathrm{dB}}$	3.15°	3.08°	3.1°
t_{avg}	12 min	40 min	130 min
σ	0.97 dB	0.26 dB	0.2 dB

4.1.3 Nulling in a specific direction

For situations where the coexistence with other communication or radar systems sharing the same frequency band are unavoidable, it is useful to be able to synthesize a radiation pattern with a steerable null to mitigate the inference while maintaining the main beam in the target direction. This comprises two optimization objectives: maximizing the directivity at the target angle and minimizing the directivity in the direction of the interferer. In order to convert the two-objective into a single objective optimization, I use the equally weighted sum method and define the fitness function as follows

$$f_{\mathrm{null}} = \frac{1}{D\left(\theta = \theta_{\mathrm{target}}\right)} + D\left(\theta = \theta_{\mathrm{nulling}}\right). \tag{4.13}$$

Here, I use the fitness function f_{null} for two optimization instances. In both cases, I consider a plane wave with the frequency of 300 GHz normally incident on the reflectarray. The main beam shall point at 45°, while a null shall be placed at 20° for the first instance and at 30° for the second instance. Two independent GA runs for these two examples are carried out. As depicted in Fig. 4.7, both calculated and EM simulated radiation patterns of the two obtained reflectarrays show that the null is successfully steered from 20° to 30°, while the main beam remains at 45°.

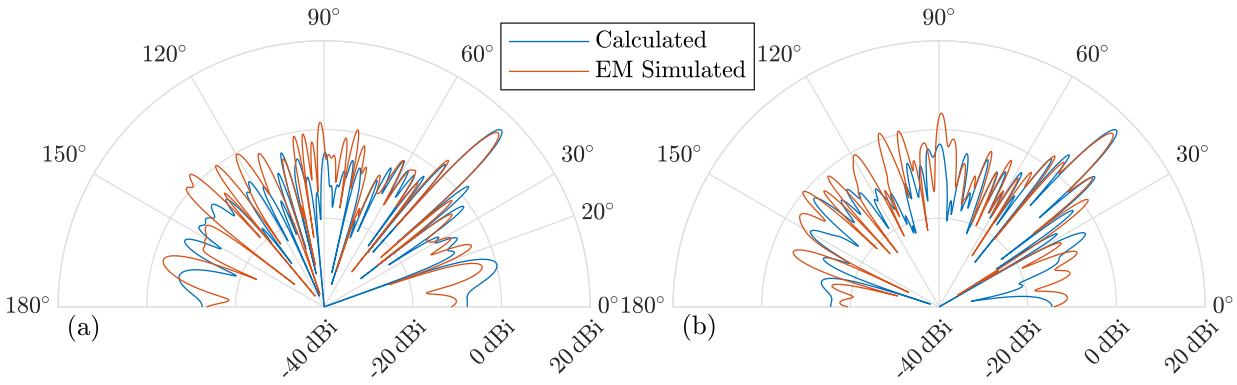

Figure 4.7: Radiation pattern of the reflectarray at 300 GHz, showing the comparison between calculated (in blue) and EM simulated (in red) results. The reflectarray's height profile is optimized using a GA to perform a nulling at the angle of (a) 20° and (b) 30° as the main beam points in the direction of 45° [3].

4.2 Multi-objective optimization

By looking at the optimization results of maximizing the directivity and minimizing the sidelobe level shown in the previous section, we can see the trade-off between these two objectives: optimization of one objective cannot be achieved without degrading the other objective. In contrast to single-objective optimization, this multi-objective optimization with conflicting objectives can have multiple optimal solutions that form a Pareto front. Note that all solutions on the Pareto front are equivalent optimal solutions. However, we usually need only one solution, which can be obtained by adding some practical considerations.

An unconstrained multi-objective optimization that has 2 objectives can be mathemat-

ically formulated as follows:

$$\text{Minimize: } \left(f_1\left(\boldsymbol{x}\right), f_2\left(\boldsymbol{x}\right)\right). \tag{4.14}$$

In single-objective optimization, there is usually only one optimal solution $\boldsymbol{x}$. In multi-objective optimization, this single solution may not exist due to the trade-off nature among the objectives. Instead, there are multiple non-dominated points. To be able to understand what are the non-dominated points, we first need to understand the domination for any two solutions. A solution $\boldsymbol{x}_1$ dominates another solution $\boldsymbol{x}_2$, if

$$\begin{aligned} &\forall i \in \{1,2\}\, f_i\left(x_1\right) \leq f_i\left(x_2\right) \text{ and} \\ &\exists i \in \{1,2\}\, f_i\left(x_1\right) < f_i\left(x_2\right). \end{aligned} \tag{4.15}$$

In the graphical representation provided in Fig. 4.8(a), it is evident that solution $\boldsymbol{x}_1$ dominates solution $\boldsymbol{x}_2$. This is supported by the observation that the conditions $f_1(\boldsymbol{x}_1) < f_1(\boldsymbol{x}_2)$ and $f_2(\boldsymbol{x}_1) = f_2(\boldsymbol{x}_2)$ are met, fulfilling the first statement. Furthermore, the second statement is satisfied as well, given that there exists at least one fitness function, in this case, f_1 for which $f_1(\boldsymbol{x}_1) < f_1(\boldsymbol{x}_2)$.

Non-dominated points are the points that are not dominated by any other solution in the feasible region. The values of the fitness functions at the non-dominated points form a frontier, which is called the Pareto front.

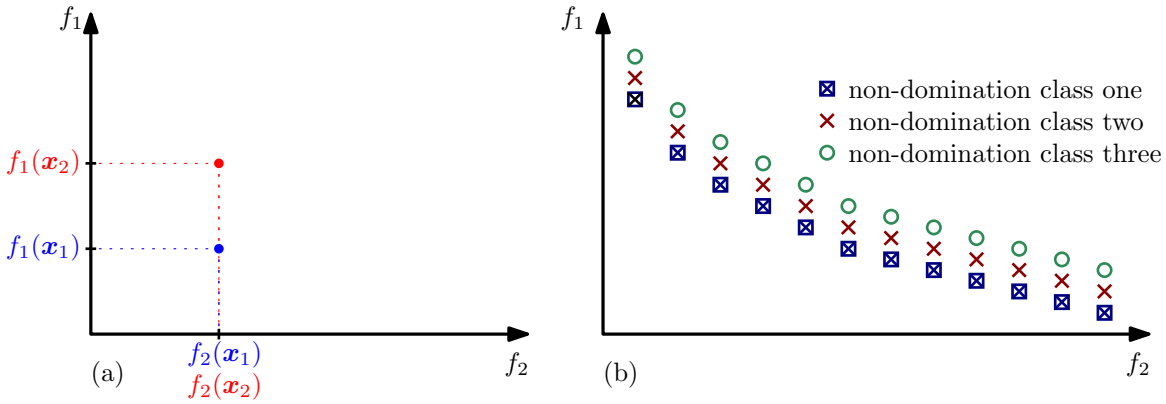

Figure 4.8: Illustrative example of three distinct non-domination classes.

The multi-objective GA implemented in MATLAB uses the non-dominated sorting genetic algorithm II (NSGA-II) proposed by Kalyanmoy Deb et.al. [110]. Here, I briefly describe the procedure of this algorithm. In any generation, the offspring population

is first created by performing genetic operations (selection, crossover, mutation) on the parents, just like a general GA. Thereafter, the population of the offspring and the population of the parents are merged and divided into different non-domination classes.

Fig. 4.8(b) presents an illustrative example of three non-domination classes. Based on the conditions given in Eq. 4.15, it is evident that non-domination class one encompasses all non-dominated points. After removing all points from non-domination class one, only points from classes two and three remain. Applying the conditions specified in Eq. 4.15 again, non-domination class two emerges as the set of non-dominated points. Similarly, upon eliminating all points from both non-domination classes one and two, non-domination class three includes the remaining non-dominated points.

Once the merged population of parents and offspring is categorized into different non-domination classes, a new generation is formed by populating it with individuals from the merged population. The population is filled subsequentially, starting with the individuals from the non-domination class one, followed by class two, and so on, until the capacity of the new generation is reached. As the merged population comprises both parents and offspring, the size of the merged population is twice the size of a new generation. Therefore, half of the individuals from the merged population will be rejected during this process. It is worth mentioning that in this algorithm, the two objectives are not merged or converted into a single objective by a parametric scalarizing approach.

In the following, I present a multi-objective optimization example that considers two conflicting objectives, namely maximizing the directivity at the angle of 45° and minimizing the sidelobe level. As in other optimization instances, I consider a plane wave with a frequency of 300 GHz that is normally incident on the reflectarray. I choose $f_{\mathrm{D},1}$ and $f_{\mathrm{SLL},1}$ as the fitness functions for maximizing the directivity and minimizing the sidelobe level objectives, respectively. The parameters of the fitness function $f_{\mathrm{SLL},3}$ are the same as those mentioned in section 4.1.2. After trying different initial populations for the multi-objective GA, I find that the algorithm outputs the best results when I use the results of single-objective GA as the initial population.

Two different multi-objective GA optimizations with two different initial populations are carried out and their resulting Pareto fronts are shown in Fig. 4.9. Fig. 4.9(a) displays the Pareto front obtained from the multi-objective GA with the initial population

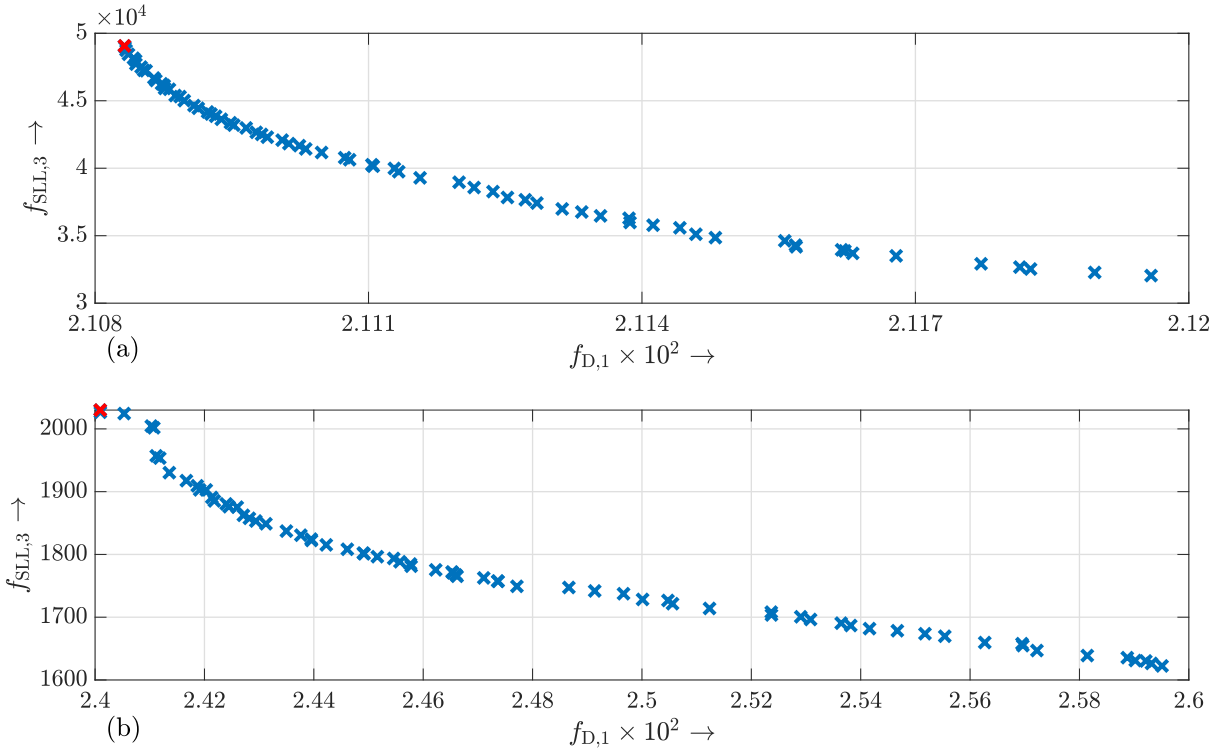

Figure 4.9: Pareto front resulting from a multi-objective GA, where the initial population is generated through a single-objective optimization GA using fitness function: (a) $f_{D,1}$ for directivity optimization and (b) $f_{SLL,3}$ for side-lobe level optimization [3].

given by the output of the single-objective GA whose objective is to maximize the directivity. Fig. 4.9(b) displays the Pareto front obtained from a multi-objective GA with the initial population given by the output of the single-objective GA whose objective is to minimize the sidelobe level. The Pareto front in Fig. 4.9(a) gives a better directivity, while the Pareto front in Fig. 4.9(b) outputs a better sidelobe level. We can conclude that the initial population dominates the optimization focus in the multi-objective optimization. As mentioned at the beginning of this section, all solutions of the Pareto front are equally optimal, and here I choose one solution and compare its results with the results obtained in the single-objective optimization. The tagged element in Fig. 4.9(a) has a directivity of 16.76 dBi and a sidelobe level of -14.2 dB. It achieves the same directivity level as the single-objective optimization, and suppresses the sidelobe level better than the single-objective optimization for maximizing the directivity. The tagged element in Fig. 4.9(b) has a directivity of 16.19 dBi and a sidelobe level of -18.59 dB. In

the previous section, the single-objective optimization aimed at minimizing the sidelobe level utilizing the fitness function $f_{\mathrm{SLL},3}$ effectively reduces the sidelobe level to -18.4 dB while achieving a directivity of 15.71 dBi at the target angle. This improvement in directivity while maintaining the same sidelobe level confirms the advantage of the multi-objective optimization.

4.3 GA-configured reflectarray vs. diffraction grating

So far, I have only shown the radiation patterns of the reflectarray optimized by the GA. In this section, I study the output of the GA optimization, i.e., the shape of the resulting reflectarray.

In section 4.1.1, I present an optimization example that employs the fitness function $f_{\mathrm{D},2}$. Fig. 4.10(a) displays the outcome of this optimization example, i.e., the height profile of the resulting reflectarray. It exhibits a periodic pattern to some extent. However, if we look closely, the number of reflectors per cycle is different. In order to detect the presence of a periodic pattern in this structure, I perform a Fourier transform of the resulting structure and depict its spatial frequency representation in Fig. 4.10(b).

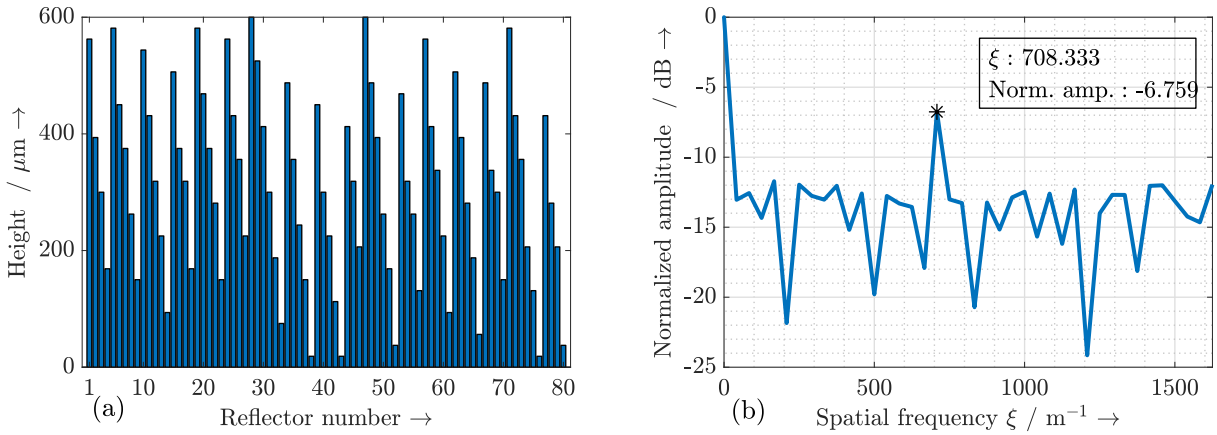

Figure 4.10: (a) Height profile of the reflectarray optimized using a GA with an objective of maximizing the directivity 45° away from the reflectarray axis. (b) Spatial frequency representation of the height profile depicted in (a) [3].

There is a dominant spatial frequency component at 708.333 m^{-1}, which corresponds to the spatial period of $\Lambda = \frac{1}{708.333\,\mathrm{m}^{-1}} = 1.412\,\mathrm{mm}$. Putting this value into the grating

equation, we get the diffraction angle of the first diffraction order $\theta = \arcsin\left(\frac{\lambda}{\Lambda}\right) = \arcsin\left(\frac{1\,\text{mm}}{1.412\,\text{mm}}\right) = 45.09°$. The complement of this angle is $\varphi = 90° - 45.09° = 44.9°$, which is very close to our target angle of 45°. This explains how such a reflectarray works: it is basically a concealed diffraction grating structure with a non-perfect period.

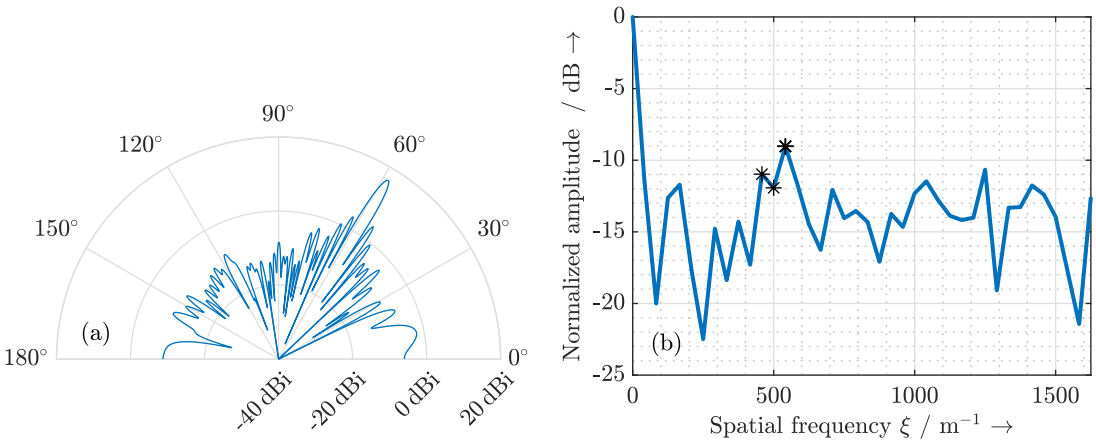

Figure 4.11: (a)Radiation pattern of the reflectarray at 300 GHz. The reflectarray's height profile is optimized using a GA to maximize the directivity in the direction of 58.5°. (b) Fourier transform of the height profile of the resulting reflectarray.

Since the reflectarray has a finite length of $l = 80 \cdot 300\,\mu\text{m}$=24 mm, the spatial frequency components of the structure are discrete and can only be the integer multiples of the fundamental spatial frequency $\xi = \frac{1}{l} = \frac{1}{24\,\text{mm}} = 41.7\,\text{m}^{-1}$. It means that the achievable spatial periods inside the reflectarray structure are also discrete. This arises the question: are the steering angles that can be achieved also discrete? Table 4.4 lists all the spatial frequency components ξ between $500\,\text{m}^{-1} \cdots 708.3\,\text{m}^{-1}$ and their corresponding spatial periods Λ, diffraction angles θ, and complementary angles φ. Now I run the GA with the objective of maximizing the directivity at the angle between the listed complementary angles φ above, let us say 58.5°. Fig. 4.11(a) is the radiation pattern of the resulting reflectarray. The main beam is successfully steered in the direction of 58.5°. The spatial frequency representation of the resulting structure, as depicted in Fig. 4.11(b) has three dominant components that correspond to the three complementary angles listed in Table 4.4 adjacent to 58.5°. This indicates that a continuous beam

Table 4.4: Achievable spatial frequency components ξ of the reflectarray, spanning from $500\,\mathrm{m}^{-1}$ to $708.3\,\mathrm{m}^{-1}$. For each ξ, the corresponding spatial period Λ, diffraction angle θ, and complementary angle φ are provided.

$\xi\,(\mathrm{m}^{-1})$	500	541.7	583.3	625	666.7	708.3
$\Lambda\,(\mathrm{mm})$	2	1.846	1.714	1.6	1.5	1.412
θ	30°	32.8°	35.7°	38.7°	41.8°	45.09°
φ	60°	57.2°	54.3°	51.3°	48.2°	44.91°

steering is possible.

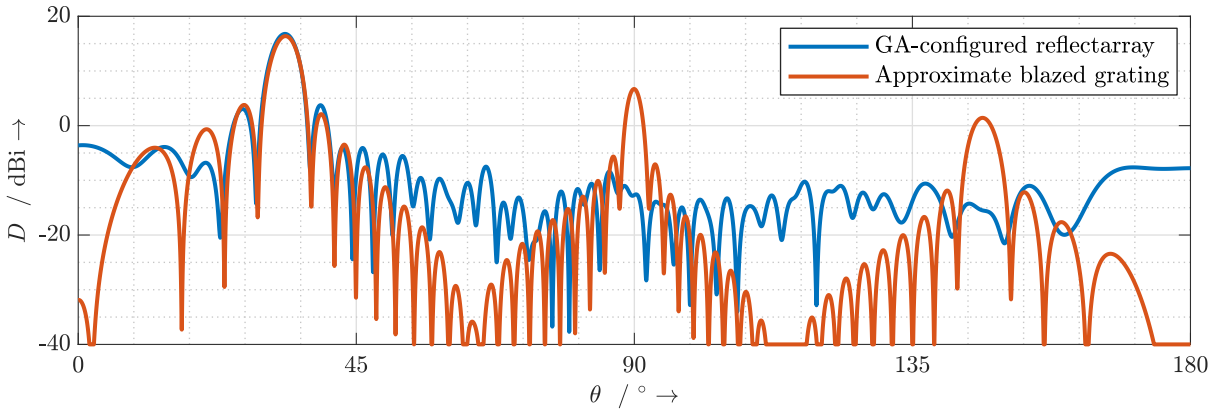

Figure 4.12: Radiation pattern of the GA-configured reflectarray (in blue). The GA aims to maximize the directivity of the reflectarray in the direction of 33.6° at the frequency of 300 GHz. Radiation pattern of the approximate blazed grating (in red), where its main beam is directed toward the angle 33.6° at the frequency of 300 GHz [3].

By analyzing the shape of the reflectarray configured by the GA, we learn that it works similar to a diffraction grating. However, the absence of the grating lobes in its radiation pattern indicates the difference between these two structures. I hereby perform an in-depth comparison. I run the GA with the objective of maximizing the directivity at the angle that can be achieved by the proposed approximate blazed grating, e.g. 33.6°. As shown in Fig. 4.12, both main beams are successfully steered at the target angle and the radiation pattern of the reflectarray configured by the GA has no grating lobes as expected. Fig. 4.13 displays the spatial frequency representations of the height profiles for the GA-configured reflectarray and the approximate blazed grating. The dominant component in the spatial frequency domain of the approximate blazed

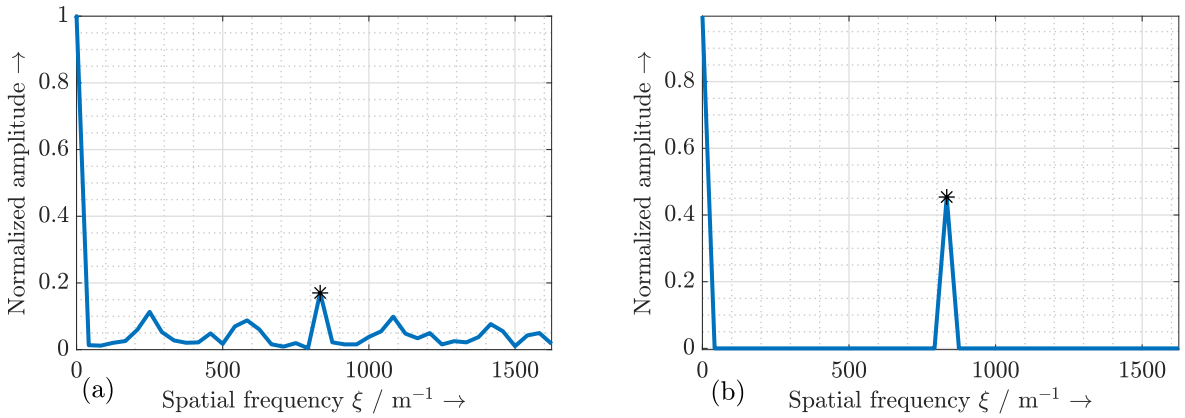

Figure 4.13: Spatial frequency representation of the height profile for (a) the GA-configured reflectarray and (b) the approximate blazed grating.

grating has a much higher amplitude, while the dominant component in the spatial frequency domain of the reflectarray configured by the GA is moderately distinct from other components. This weakened spatial frequency component characteristic makes the grating lobes absent, thus making the reflectarray configured by the GA superior to the conventional diffraction grating.

4.4 Measured radiation characteristics

In order to verify the beam steering capability of the reflectarray optimized by a GA and the absence of the grating lobes in its radiation pattern, we fabricate two reflectarray phantoms whose height profiles are determined by a GA. The photographs of the reflectarray phantoms are shown in Fig. 4.14. These two phantoms are designed to have the same steering angles as the approximate blazed grating phantoms outlined in section 3.4, namely, 56.4° and 41.8° at 300 GHz. The planar and 3D radiation patterns of the reflectarray phantoms are measured using the same measurement setups in section 3.5.2. To facilitate comparison, I show the measured radiation patterns for both the GA-configured reflectarray phantoms and the approximate blazed grating phantoms.

As depicted in Fig. 4.15, the broadband radiation patterns of the reflectarray phantoms configured by the GA and the approximate blazed grating phantoms exhibit similar characteristics. The main beam comes close to the grating' normal vector with increas-

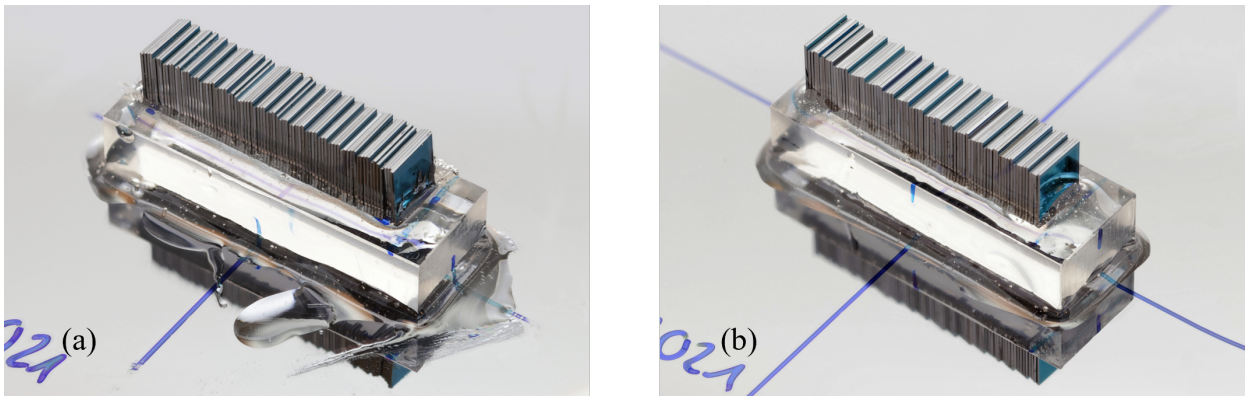

Figure 4.14: (a) Photograph of reflectarray phantom, whose height profile optimized by a GA. The objective of the GA is to maximize the directivity in the direction of 56.4° at 300 GHz. (b) Photograph of reflectarray phantom, whose height profile optimized by a GA. The objective of the GA is to maximize the directivity in the direction of 41.8° at 300 GHz.

ing frequency, verifying that the GA-configured reflectarray works similarly to a grating structure. Observing the radiation patterns at 300 GHz, as depicted in Fig. 4.16, these two GA-configured reflectarray phantoms successfully steer the main beam to the target angles, demonstrating their beam steering capability. Furthermore, the 3D radiation patterns in Fig. 4.17 clearly show that the GA-optimized reflectarray phantoms have no grating lobes, which is a result of the weakened periodicity that eliminates the grating lobes, making them superior to conventional diffraction gratings.

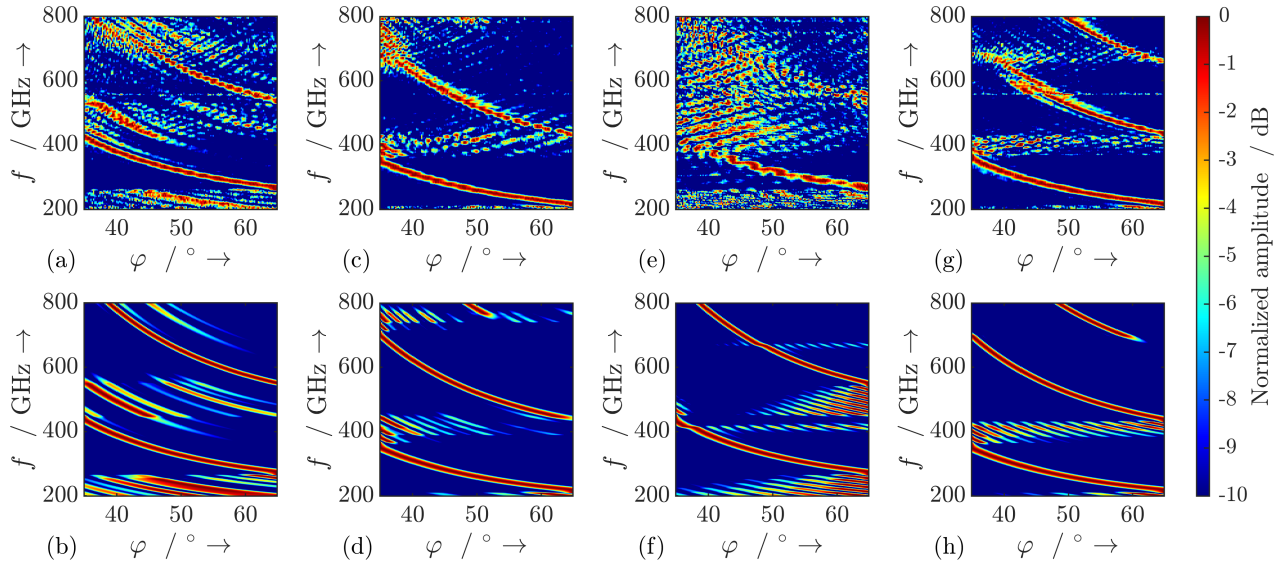

Figure 4.15: (a) Measured and (b) calculated radiation pattern of the reflectarray obtained by a GA phantom 1 for the frequencies between 200 GHz and 800 GHz at the angles between 35° and 65°. (c) Measured and (d) calculated radiation pattern of the reflectarray obtained by a GA phantom 2 for the frequencies between 200 GHz and 800 GHz at the angles between 35° and 65°. (e) Measured and (f) calculated radiation pattern of the approximate blazed grating phantom 1 for the frequencies between 200 GHz and 800 GHz at the angles between 35° and 65°. (g) Measured and (h) calculated radiation pattern of the approximate blazed grating phantom 2 for the frequencies between 200 GHz and 800 GHz at the angles between 35° and 65°.

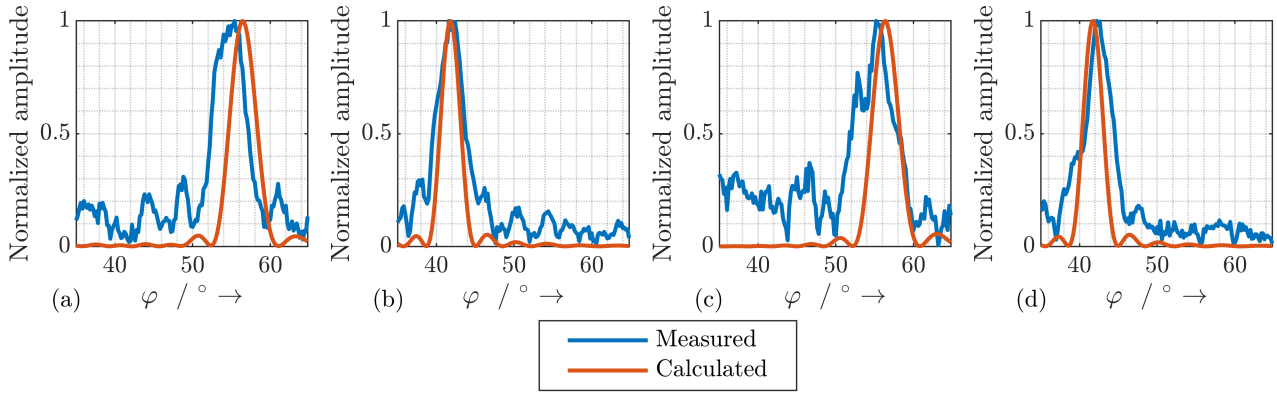

Figure 4.16: Measured radiation pattern (in blue) and calculated radiation pattern (in red) at 300 GHz of (a) the reflectarray obtained by a GA phantom 1, (b) the reflectarray obtained by a GA phantom 2, (c) the approximate blazed grating 1, and (d) the approximate blazed grating 2.

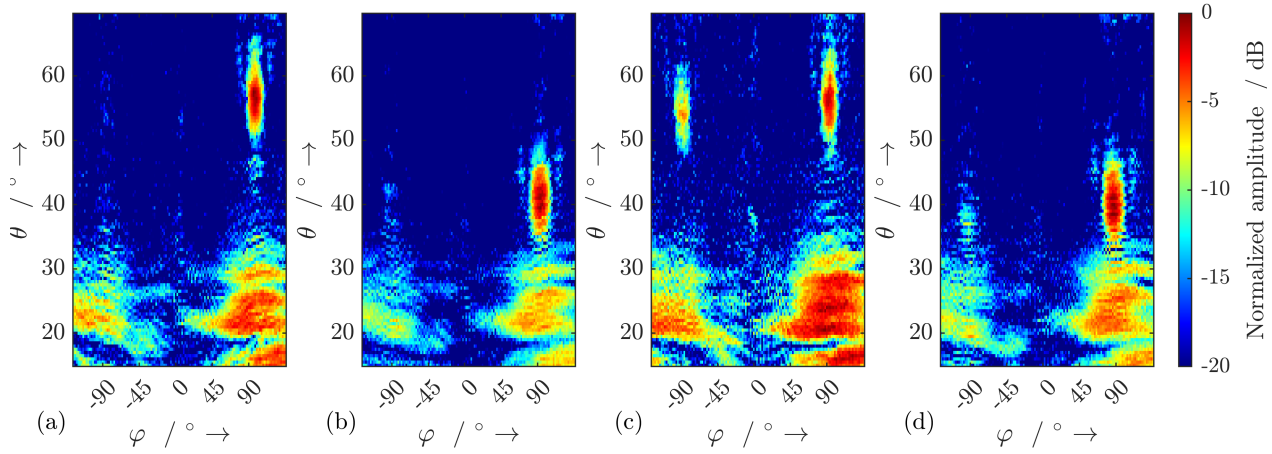

Figure 4.17: Measured 3D radiation pattern at the design frequency of 300 GHz of (a) the reflectarray obtained by a GA phantom 1, (b) the reflectarray obtained by a GA phantom 2, (c) the approximate blazed grating phantom 1, and (d) the approximate blazed grating phantom 2 for the elevation range between 15° and 65° and azimuth range between −130° and 130°.

CHAPTER

FIVE

ANALYSIS OF THE PERFORMANCE OF THE REFLECTARRAY IN BROADBAND APPLICATIONS

The reflected angle from the approximate blazed grating and the GA-generated structure that exhibits non-perfect periodicity, varies with changes in frequency as predicted by the grating equation. This phenomenon is commonly referred to as beam squint. To obtain broadband information at one spatial location, it is necessary to adaptively adjust the reflectarray as the frequency sweeps. However, those structures are not suitable for applications that require simultaneous bandwidth coverage, such as communications. In this section, I will examine the bandwidth limitations of the reflectarray and explore potential configurations that can enhance their bandwidth.

To comprehend the bandwidth limitation of the reflectarray, it is necessary to have a understanding of the phase shift mechanism employed by the reflective elements present in the array. The position of the reflective element can be adjusted vertically, causing a local change in the travel distance of the incident wave before it is reflected, resulting in a corresponding phase shift.

To steer the beam away from the reflectarray normal by an angle of α_0, the most straightforward configuration is to arrange the reflectarray in such a way that it approximates a large mirror with a tilting angle of $\frac{\alpha_0}{2}$, as dictated by the law of reflection.

This can also be justified from the array's perspective, as illustrated in Fig. 5.1. The phase reference point P_0 is chosen where the reflected wave, just about to leave P_0, possesses a phase of 0, represented by the phasor notation e^{j0}. Consider an arbitrary point P_1 on the reflectarray's surface positioned at a height h above the reference point P_0. The phase of the reflected wave at P_1 leads that of the reflected wave at the reference point P_0 by hk_0, where k_0 is the wave number in free space. Its phasor can be expressed as $e^{j \cdot hk_0}$. Let P_2 denote the intersection of the wavenumber vector of the reflected beam across the point P_1 and the wave front of the reflected beam across P_0. As the reflected wave travels from point P_1 to P_2, it undergoes a phase retardation of lk_0, resulting in a phasor of $e^{j \cdot (hk_0 - lk_0)}$ at P_2. Based on the geometric configuration, it is evident that $h = l$, implying that the P_2 shares the same phase as P_0.

This mirror configuration is equivalent to an array employing true time delays, which enables the reflectarray to exhibit broadband performance by maintaining a constant angle of reflection regardless of the frequency of the incident wave.

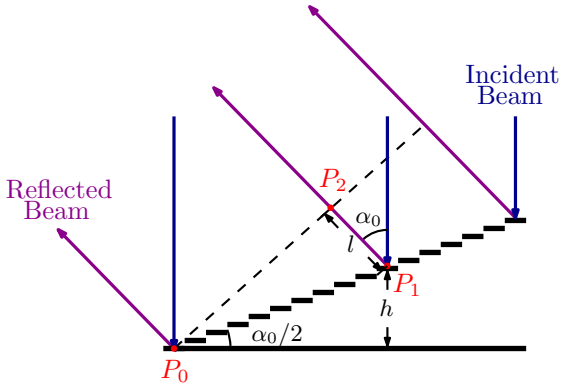

Figure 5.1: Geometry for a plane wave incident normally on the surface of the reflectarray approximating a large mirror.

Consider the reflectarray discussed in this work. Within the reflectarray, the maximum phase shift $\varphi_{\max}$ that is required to reflect the beam away from the reflectarray normal by an angle of α_0, is determined by the two reflective elements positioned at the opposite ends, separated by the reflectarray length of 24 mm. Mathematically, this can be expressed as: $\varphi_{\max} = 24\,\text{mm} \cdot \tan\left(\frac{\alpha_0}{2}\right) \cdot k_0$. As depicted in Fig. 5.2, the required maximum phase shift $\varphi_{\max}$ rapidly exceeds 2π as α_0 increases, and at $\alpha_0 = 90°$, it approaches nearly 25π. The MEMS actuator offers a maximum vertical displacement of 600 μm, equivalent to a phase shift of 1.2π at 300 GHz. It is obvious that for most values

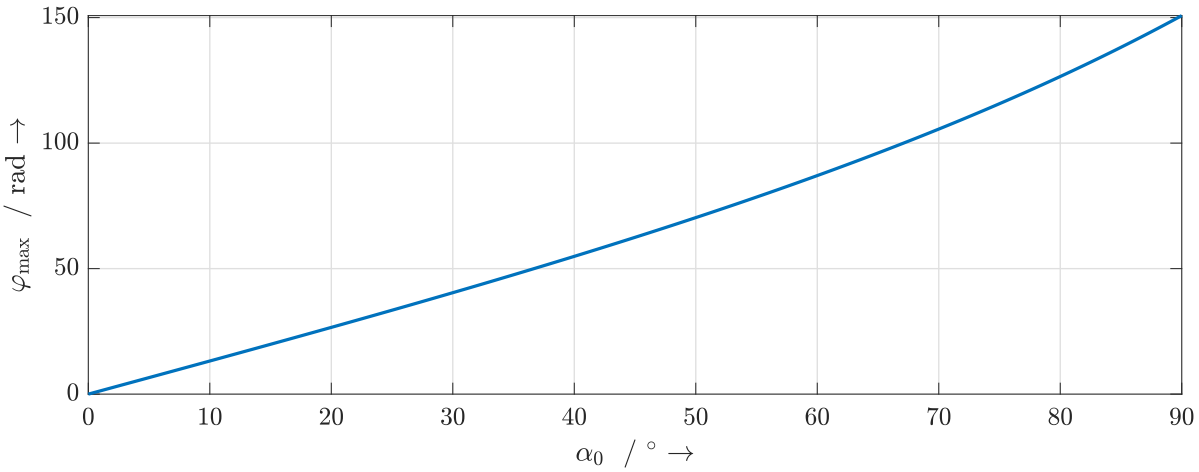

Figure 5.2: Maximum required phase shift $\varphi_{\max}(\alpha_0)$ within the reflectarray as a function of the variable angle α_0. The length of the reflectarray is 24 mm. A normally incident plane wave at the frequency of 300 GHz is considered.

of α_0, the required phase shift surpasses the capability of the MEMS actuation system. However, we can leverage the periodicity of phase for harmonic waves to overcome this limitation. Instead of relying on the time delay to steer the beam, a phase shift

$$\varphi = \mathrm{mod}\,(lk_0, 2\pi) \tag{5.1}$$

can be created within a confined 2π range. Using $\varphi = hk_0$ gives

$$hk_0 = \mathrm{mod}\,(lk_0, 2\pi)\,, \tag{5.2}$$

which can be rewritten as

$$lk_0 = N \cdot 2\pi + hk_0, N \in \mathbb{N}. \tag{5.3}$$

When $N = 0$, Eq. 5.3 reduces to $l = h$. This represents the true time delay scenario discussed earlier. Notably, the frequency-dependent variable k_0 is absent in the equation, reaffirming the inherent broadband nature of this configuration.

For fixed non-zero values of N, l, and h, Eq. 5.3 is valid only for a specific frequency $f_0 = \dfrac{k_0 c_0}{2\pi}$ with wavelength $\lambda_0 = \dfrac{2\pi}{k_0}$. As we tune the frequency by Δf, corresponding to a change in wavelength of $\Delta\lambda$, the left-hand side of Eq. 5.3 is increased by

$$l \cdot \frac{2\pi}{\lambda_0 - \Delta\lambda} - l \cdot \frac{2\pi}{\lambda_0} = l \cdot 2\pi \cdot \frac{\Delta\lambda}{\lambda_0 \cdot (\lambda_0 - \Delta\lambda)}, \tag{5.4}$$

while the right hand side of the equation is increased by

$$h \cdot \frac{2\pi}{\lambda_0 - \Delta\lambda} - h \cdot \frac{2\pi}{\lambda_0} = h \cdot 2\pi \cdot \frac{\Delta\lambda}{\lambda_0 \cdot (\lambda_0 - \Delta\lambda)}. \tag{5.5}$$

This introduce a phase error φ_{err} of

$$\varphi_{\text{err}} = (l - h) \cdot 2\pi \cdot \frac{\Delta\lambda}{\lambda_0 \cdot (\lambda_0 - \Delta\lambda)}, \tag{5.6}$$

resulting in beam squint.

To demonstrate the impact of phase errors caused by changes in frequency, let us consider a broadband signal with a bandwidth of 20 GHz centered at 300 GHz. Fig. 5.3(a) illustrates the required maximum phase shifts φ_{max} for the center frequency of 300 GHz and end frequencies of 290 GHz and 310 GHz. With an increase in the steering angle α_0, the required phase shifts for different frequencies exhibit a more pronounced distinction. Fig. 5.3(b) presents the same phase shifts as in Fig. 5.3(a), but wrapped within a range of 2π. I now utilize the wrapped phase at 300 GHz to derive a corresponding height profile $h|_{f=300\,\text{GHz}}$ of the reflective elements, employing the relationship $h|_{f=300\,\text{GHz}} = \frac{\text{mod}\ \left(\varphi_{\text{max}}|_{f=300\,\text{GHz}}, 2\pi\right)}{k_0|_{f=300\,\text{GHz}}}$. The representation of the height profile $h|_{f=300\,\text{GHz}}$ is depicted in Fig. 5.3(c). Fig. 5.3(d) showcases the resulting phase shifts $\varphi_{\text{resulting}} = k_0 \cdot h|_{f=300\,\text{GHz}}$ obtained from the height profile $h|_{f=300\,\text{GHz}}$ for the three different frequencies. An evident disparity is observed between the expected phase shifts in Fig. 5.3(b) and the resulting phase shifts $\varphi_{\text{resulting}}$ obtained from the height profile displayed in Fig. 5.3(d). This discrepancy represents the phase error, which exhibits an increasing trend as the angle α_0 becomes larger.

In the preceding chapter, it is established that the GA-configured reflectarray operates as a concealed diffraction grating. Its height profile induces a wrapped phase pattern upon the incident wave. Consequently, the presence of the phase error φ_{err} is anticipated to affect the radiation pattern of the GA-configured reflectarray. To confirm this hypothesis, I exam two specific steering angles, namely 10° and 70°. For each angle, I utilize the reflectarray obtained through the GA optimization process discussed in the previous chapter. The reflectarrays are optimized to maximize the directivity at 300 GHz at 10° and 70°, respectively. I then analyze the radiation patterns at the frequencies 290 GHz, 300 GHz, and 310 GHz. As anticipated, when the main beam is

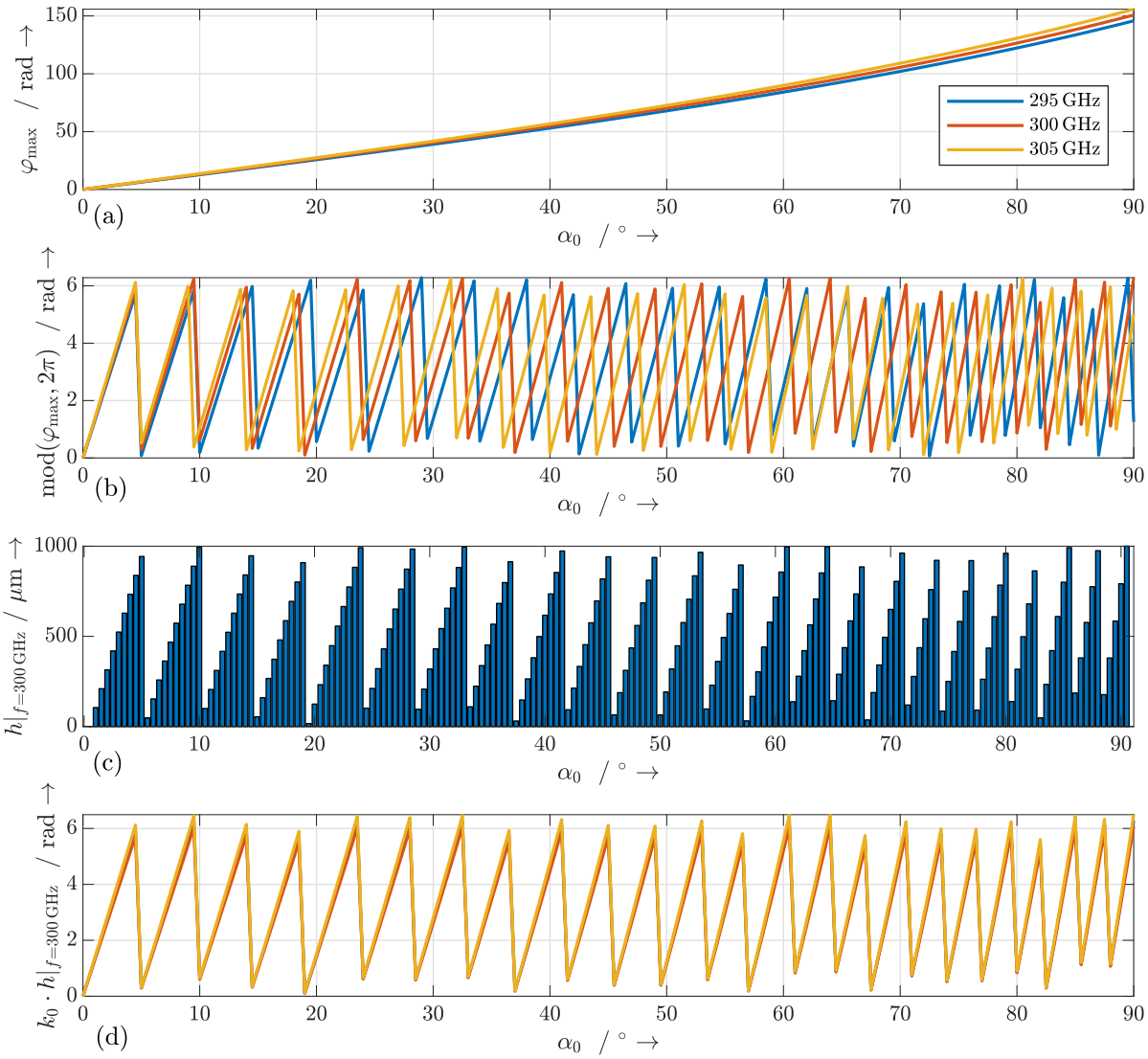

Figure 5.3: (a) Maximum required phase shift $\varphi_{\max}(\alpha_0)$ within the reflectarray as a function of the variable angle α_0. The length of the reflectarray is 24 mm. A normally incident plane wave at three different frequencies of 290 GHz (in blue), 300 GHz (in red), and 310 GHz (in yellow) is considered. (b)Wrapped phase of the maximum required phase shift $\varphi_{\max}(\alpha_0)$ within the reflectarray, that is depicted in Fig. 5.3(a), as a function of the variable angle α_0. (c) Height profile $h|_{f=300\,\mathrm{GHz}} = \dfrac{\mathrm{mod}\ (\varphi_{\max}|_{f=300\,\mathrm{GHz}}, 2\pi)}{k_0|_{f=300\,\mathrm{GHz}}}$ derived by the wrapped phase at 300 GHz. (d) Resulting maximum phase shift $\varphi_{\mathrm{resulting}} = k_0 \cdot h|_{f=300\,\mathrm{GHz}}$ obtained from the height profile for the frequencies 290 GHz (in blue), 300 GHz (in red), and 310 GHz (in yellow).

steered towards 10° at 300 GHz, the radiation patterns of the reflectarray at the three different frequencies exhibit a consistent main beam direction as depicted in Fig. 5.4(a). In contrast, at the steering angle of 70° shown in Fig. 5.4(b), we observe a distinct beam squint: a variation in the main beam direction as the frequency changes.

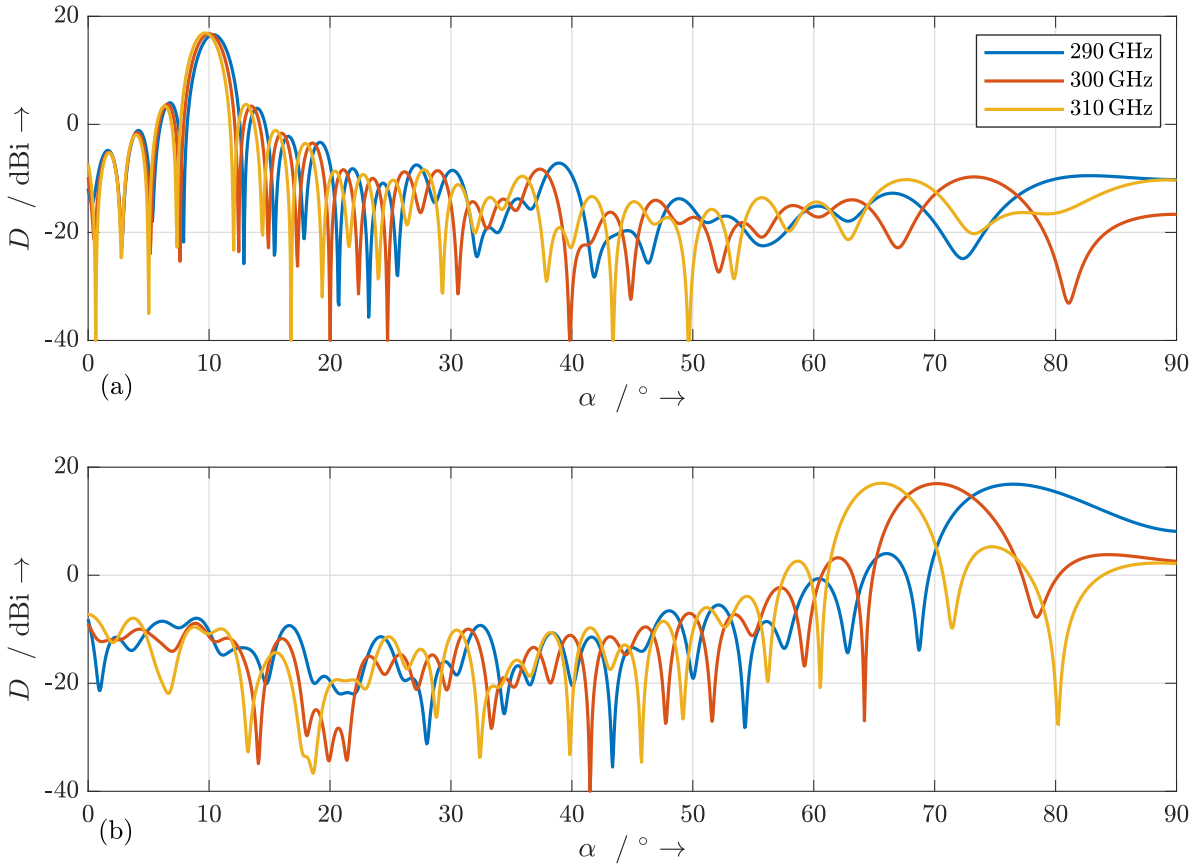

Figure 5.4: (a) Radiation patterns of the reflectarray at three different frequencies of 290 GHz (in blue), 300 GHz (in red), and 310 GHz (in yellow). The reflectarray is optimized using a GA for the maximum directivity in the direction of 10°, primarily at the frequency of 300 GHz. (b) Radiation patterns of the reflectarray at three different frequencies of 290 GHz (in blue), 300 GHz (in red), and 310 GHz (in yellow). The reflectarray is optimized using a GA for the maximum directivity in the direction of 70°, primarily at the frequency of 300 GHz.

To further analysis the performance of the designed reflectarray in broadband applications, I calculate the resulting reflectarray's beam squint, denoted as $\Delta\alpha$, and the directivity variation in the target direction over the whole bandwidth, denoted as ΔD,

considering a broadband signal with a bandwidth of 20 GHz centered at 300 GHz. The results in Fig. 5.5 demonstrate that for a 3 dB gain bandwidth of 20 GHz, the main beam can be steered within $\pm 30^\circ$ around the reflectarray normal. This represents a relatively large steering range for a reflectarray. As the bandwidth decreases, for example, to 10 GHz, the gain variation remains below 3 dB for nearly the entire elevation coverage. Thus, there exists a trade-off between the steering range and the 3 dB gain bandwidth of the reflectarray, which must be carefully considered based on the specific application scenario.

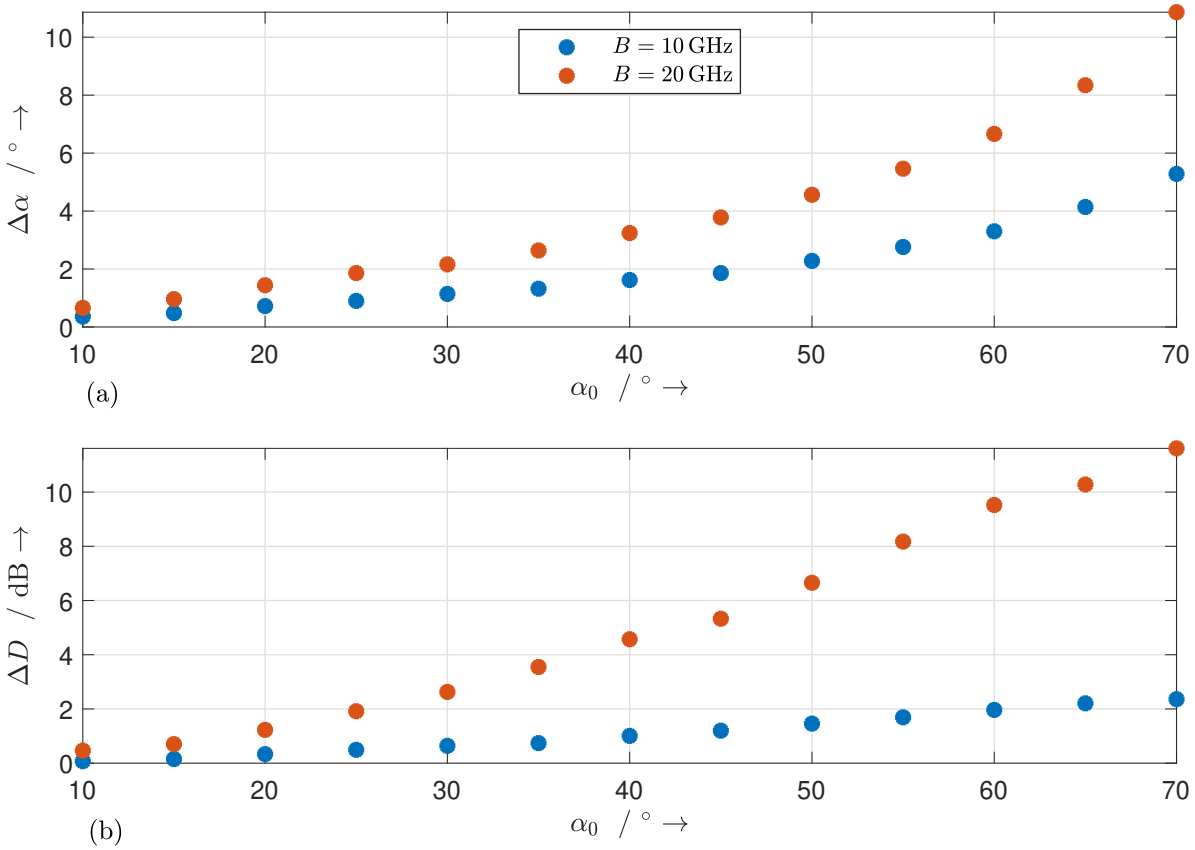

Figure 5.5: Resulting (a) beam squint $\Delta\alpha$ and (b) directivity variation ΔD in the target direction as a function of the variable angle α_0. A broadband signal with a bandwidth $B = 10\,\mathrm{GHz}$ (in blue) and $B = 20\,\mathrm{GHz}$ (in red) centered at 300 GHz is considered here.

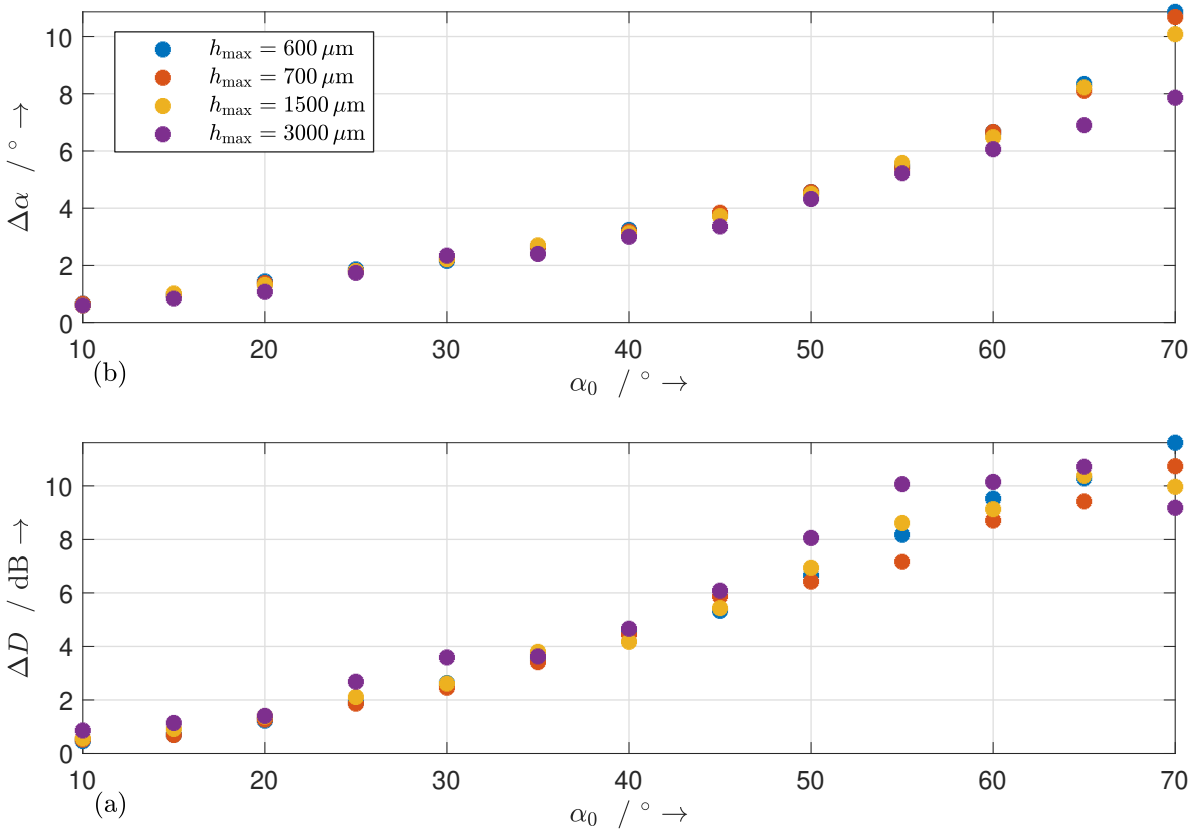

Figure 5.6: Resulting (a) beam squint $\Delta\alpha$ and (b) directivity variation in the target direction ΔD as a function of the variable angle α_0 for 4 different maximum actuation displacements. A broadband signal with a bandwidth of 20 GHz centered at 300 GHz is considered here.

Based on Eq. 5.6, the phase error is directly proportional to the difference between the travel length in free space l and the vertical displacement h of the reflective element. In order to reduce the phase error and enhance the bandwidth, one straightforward approach is to increase the vertical displacement h of the MEMS reflective element. Without considering the technological feasibility of the MEMS reflective element at this stage, I demonstrate this improvement through numerical analysis. Specifically, I employ a GA to evaluate three additional maximum actuation displacements of the reflective element apart from 600 μm: 700 μm, 1500 μm, and 3000 μm.

The resulting beam squint $\Delta\alpha$ and directivity variation ΔD in Fig. 5.6, do not decrease with the increasing maximum actuation displacement, contrary to expectations. To understand this observation, I show one resulting height profile of the reflectarray with

the maximum actuation displacement $h = 3000\,\mu$m. The travel length l in free space exhibits a linear increase (or decrease) across the array, whereas the height profile of the reflectarray depicted in Fig. 5.7 displays discontinuities that introduce disruptions in the continuous phase profile, leading to consequent phase errors.

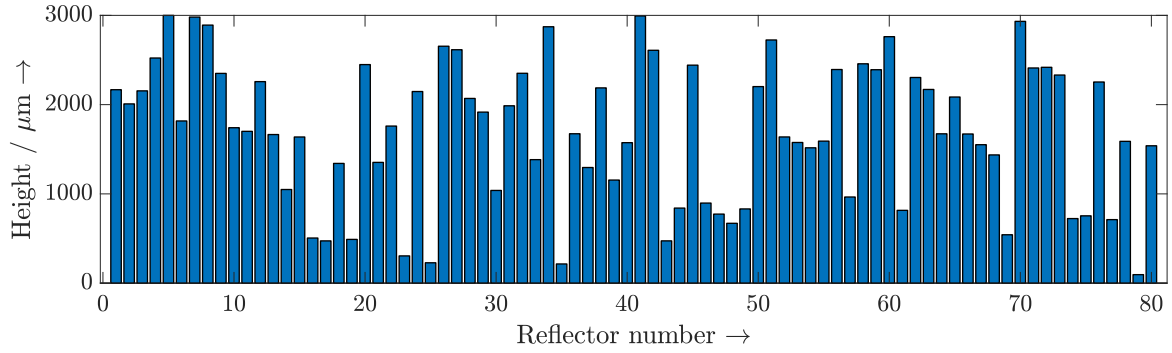

Figure 5.7: Height profile of the reflectarray optimized using a GA with an objective of maximizing the directivity 15°. A maximum actuation displacement of 3000 μm is considered here.

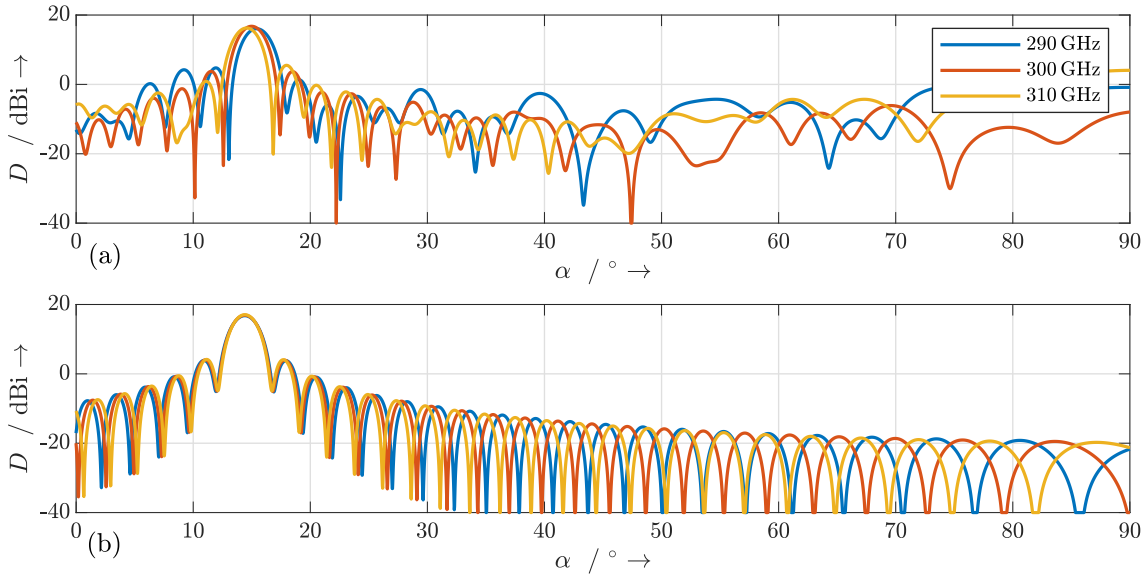

Figure 5.8: (a) Radiation patterns of the reflectarray. The reflectarray is optimized using a GA for the maximum directivity in the direction of 15°, primarily at the frequency of 300 GHz. (b) Radiation patterns of the reflectarray that configured to approximate a mirror. For both reflectarrays, a maximum actuation displacement of 3000 μm is considered.

For large actuation displacement to contribute to bandwidth enhancement, it is crucial for the height profile to demonstrate a continuous increase (or decrease) across the array. This consistent variation creates a mirror configuration, aligning with the concept mentioned earlier in this chapter: a mirror is analogous to a true time delay phased array, providing a broad bandwidth and mitigating the beam squint effect. To validate this, I compare the radiation pattern of the reflectarray with the height profile shown in Fig. 5.7 to that of the reflectarray approximating a large mirror. It is evident that the mirror configuration completely eliminates beam squint that is observed in the reflectarray with discontinuities in its height profile.

CHAPTER

SIX

CONCLUSION AND OUTLOOK

6.1 Conclusion

In this work, I have provided a comprehensive overview of five different terahertz beam steering and beamforming techniques, along with their state-of-the-art implementations. Among these techniques, the terahertz phased array stands out as a promising approach to achieve a compact and lightweight beam steering system, as it is allows for monolithic integration of the beam steering network at both the transmitter and receiver sides. A major challenge lies in the lack of efficient terahertz phase shifters, leading to the current realization of the beam steering network in the RF and infrared domain, where conversion efficiency remains a significant concern. On the other hand, the leaky wave antenna presents an attractive feature of not requiring phase shifters. It operates by leveraging the progressive phase change along a waveguide or transmission line. Nevertheless, beam steering using this technique relies on frequency tuning, resulting in bandwidth limitations that make it unsuitable for applications involving spectroscopy and broadband communication.

The remaining three terahertz beam steering and beamforming techniques require rather bulky and discrete systems. The beam steering technique accomplished by tilting the laser source, which illuminates the non-linear crystal for terahertz generation,

is limited to its implementation in a free-space optoelectronic terahertz system. On the other hand, the terahertz free space-coupled terahertz beam steering and beam-forming devices offer greater flexibility as they can be employed in any terahertz free space path, regardless of the terahertz generation methods. Additionally, their ease of fabrication makes them highly accessible to use. However, it is worth noting that beam steering techniques using these devices often results in discrete steering angles and slower beam steering speed due to the involvement of mechanical movement. In contrast, the terahertz reflectarray exhibits the advantage of being employable in any terahertz free space path, along with a fast and continuous beam steering capability due to its nature as an array.

In my thesis, I presented a design for a reconfigurable 1D terahertz reflectarray. The reflectarray comprises 80 reflective elements, each with dimensions of $300\,\mu\text{m} \times 5000\,\mu\text{m}$. The reflective elements are arranged next to each other on their longer side. These reflective elements are individually driven by 5-bit MEMS actuators, allowing for a maximum vertical displacement of $600\,\mu\text{m}$. The function of the MEMS driven reflective elements is to spatially modulate the phase of the local terahertz wave. As the conventional array factor cannot be applied to calculate the radiation pattern of the reflectarray, a novel mathematical model based on the Huygens-Fresnel principle is proposed.

To enable beam steering, the reflectarray is initially configured to approximate a blazed grating. The beam steering capability of this configuration is evaluated across a frequency range of 0.3 THz to 1 THz and verified through consistent results obtained from EM simulations and the proposed mathematical model. At the lower frequency of 0.3 THz, a maximum steering angle of $\pm 56.4^\circ$ from the grating normal is achieved. However, the steering range decreases with increasing frequency, reaching a maximum steering range of only $\pm 11.5^\circ$ from the grating normal at 1 THz. Despite the decreasing steering range, the approximate blazed grating maintains a high grating efficiency above 0.8 for most of the achievable steering angles. This allows the reflectarray to achieve a directivity comparable to an equivalent uniform linear array of isotropic radiators of the same length as the reflectarray. The numerical analysis also reveals some limitations of the approximate blazed grating, such as discrete achievable steering angles and the appearance of grating lobes due to poor grating efficiency caused by the finite steps of the actuators.

In order to overcome these limitations and enhance the beam steering performance of the reflectarray, I used a GA to customize and tailor its radiation pattern. The GA successfully optimized three key features in the radiation pattern of the reflectarray, as demonstrated by both EM simulations and calculations. Firstly, the GA can maximize the directivity at a specific angle, resulting in an impressive directivity of 16.82 dBi at 0.3 THz, slightly surpassing the directivity of an equivalent uniform linear array of isotropic radiators with the same array length. Secondly, the GA can minimize the sidelobe level, achieving a sidelobe level of -18.4 dB, which is 5 dB lower than the innermost sidelobe level of -13.5 dB achieved by a linear array with a linearly increasing phase profile. Thirdly, the GA can insert nulls at specific angles in the radiation pattern while maintaining the main beam direction, allowing the reflectarray to mitigate an interferer. Furthermore, a trade-off behaviour between the objective of maximizing directivity and the objective of minimizing sidelobe levels is observed. A multi-objective GA is therefore employed to identify a set of optimal solutions, known as the Pareto front. An analysis of the reflectarray optimized by the GA through Fourier-transforming its height profile reveals that it exhibits as a quasi-grating with non-perfect periodicity, resulting in the absence of grating lobes in the radiation pattern.

Four different reflectarray phantoms, all without MEMS actuation systems, are fabricated, and their planar and 3D radiation patterns are measured. Among these four, two are designed as approximate blazed grating with diffraction angle of 56.4° and 41.8° at 0.3 THz, respectively. The other two reflectarrays are optimized by the GA to have the same main beam direction as the two approximate blazed gratings. The measured radiation patterns of the all four reflectarray phantoms closely align with the predictions of the mathematical model, showing a maximum deviation of only 2° in terms of the main beam direction. This validation strongly emphasizes the accuracy and reliability of the proposed mathematical model. The measured 3D radiation pattern of the reflectarray phantoms optimized by the GA demonstrates the absence of grating lobes, while the approximate blazed grating phantoms exhibit grating lobes. This observation aligns with the analysis, indicating that the non-perfect periodicity within the GA-optimized reflectarray effectively eliminates grating lobes.

Both the proposed configuration, namely the approximate blazed grating and the GA-optimized reflectarray, exhibit potential for specific broadband applications, such as frequency domain spectroscopy involving frequency sweeps. In these applications, it

is essential to adjust the height profile of the reflectarray to maintain the main beam in a fixed direction as the frequency changes. However, for applications requiring simultaneous bandwidth coverage, such as broadband communication, a phenomenon known as beam squint occurs, where different components are steered in varying directions. The bandwidth performance of the reflectarray is limited by the achievable throw of the reflective elements. In this study, a maximum throw of 600 μm is considered, corresponding to a phase shift of 1.2π at 300 GHz. This implies that terahertz wave can only be phase shifted by the reflective element, rather than true time delayed, which typically allows for phase shifting over multiples of 2π. For a 3 dB gain bandwidth of 10 GHz, the reflectarray can be utilized for an entire elevation coverage. However, as the gain bandwidth is increased to 20 GHz, the usable range of the reflectarray is reduced to $\pm 30^\circ$ around the reflectarray normal. When configuring the reflectarray for particular applications that demand simultaneous bandwidth, like communication, this limitation should be thoroughly considered in the design process.

6.2 Outlook

The MEMS-based reflectarray, complemented by the proposed mathematical model and GA, exhibits potential for developing highly versatile radiation patterns. The reflectarray can achieve sophisticated radiation patterns, including multiple beams and flat top profile. These features empower the reflectarray to be utilized in a diverse range of applications. Moreover, the reflectarray offers the capability of not only beam steering but also beamforming, allowing it to to focus and collimate the terahertz wave.

The optimization method and fitness functions proposed in this work can be readily adapted for designing other types of terahertz reflectarray that employ diverse phase shifting mechanisms. Additionally, they can be applied to terahertz antenna arrays to optimize their geometrical arrangement, as well as phase and amplitude distributions for improved performance.

Despite the highly promising results obtained through the GA optimization in this work, one significant drawback remains in the form of the lengthy optimization time. To achieve real-time beam steering, a pre-emptive execution of the GA followed by loading all configurations corresponding to different frequencies and directions into a look-up table is necessary, resulting in considerable computational effort. An alterna-

tive approach to address this issue is to explore the use of artificial neural networks. By training an artificial neural network to output the reflectarray configuration based on the desired angle and frequency inputs, the need for a look-up table can be eliminated. This has the potential to enable real-time configuration of the reflectarray, offering a more efficient and practical solution for rapid beam steering.

APPENDIX

A1

LIST OF ABBREVIATIONS

cw	continuous wave
DAC	digital-to-analog converter
EM	electromagnetic
FDS	frequency-domain spectroscopy
FDTD	finite-difference time-domain
GA	genetic algorithm
MEMS	micro-electromechanical systems
NSGA-II	non-dominated sorting genetic algorithm II
ODU	optical delay unit
RF	radio frequency
Rx	receiver
TDS	time-domain spectroscopy
TPX	polymethylpentene

Tx	transmitter

APPENDIX

A2

LIST OF PUBLICATIONS OF THE AUTHOR

Journal publications (first author)

[1] **X. Liu**, L. Samfaß, K. Kolpatzeck, L. Häring, J. C. Balzer, M. Hoffmann, and A. Czylwik, "Terahertz beam steering concept based on a mems-reconfigurable reflection grating," *Sensors*, vol. 20, 2020. doi: 10.3390/s20102874

[2] **X. Liu**, K. Kolpatzeck, L. Häring, J. C. Balzer, and A. Czylwik, "Wideband beam steering concept for terahertz time-domain spectroscopy: Theoretical considerations," *Sensors*, vol. 20, 2020. doi: 10.3390/s20195568 *(shared first authorship)*

[3] **X. Liu**, L. Schmitt, B. Sievert, J. Lipka, C. Geng, K. Kolpatzeck, D. Erni, A. Rennings, J. C. Balzer, M. Hoffmann, and A. Czylwik, "Terahertz Beam Steering Using a MEMS-Based Reflectarray Configured by a Genetic Algorithm," *IEEE Access*, vol. 10, pp. 84458-84472, 2022, doi: 10.1109/ACCESS.2022.3197202

Conference publications (first author)

[4] **X. Liu**, K. Kolpatzeck, L. Häring, and A. Czylwik, "Experimental validation of a phase control concept for photonically steered terahertz phased array transmitters

at microwave frequencies," in *2018 First International Workshop on Mobile Terahertz Systems (IWMTS)*, 2018. doi: 10.1109/IWMTS.2018.8454685

[5] **X. Liu**, K. Kolpatzeck, A. Öztürk, B. Friederich, D. Damyanov, L. Häring, T. Schultze, J. C. Balzer, and A. Czylwik, "Wideband characterization of 3d printed thz rectangular dielectric waveguides by thz frequency-domain spectroscopy," in *2019 Second International Workshop on Mobile Terahertz Systems (IWMTS)*, 2019. doi: 10.1109/IWMTS.2019.8823720

[6] **X. Liu**, K. Kolpatzeck, B. Friederich, D. Damyanov, L. Häring, T. Schultze, J. C. Balzer, and A. Czylwik, "Spectroscopic characterization of 3d printed thz rectangular polymer waveguides," in *2019 44th International Conference on Infrared, Millimeter, and Terahertz Waves (IRMMW-THz)*, 2019. doi: 10.1109/IRMMW-THz.2019.8873855

[7] **X. Liu**, C. Geng, X. Guo, K. Kolpatzeck, L. Häring, J. C. Balzer, and A. Czylwik, "Design and characterization of 3d printed polymer terahertz multimode interference couplers," in *2020 45th International Conference on Infrared, Millimeter, and Terahertz Waves (IRMMW-THz)*, 2020. doi: 10.1109/IRMMW-THz46771.2020.9370927

[8] **X. Liu**, L. Schmitt, K. Kolpatzeck, M. Hoffmann, J. C. Balzer, and A. Czylwik, "Configuration of a mems-based terahertz reflectarray using a genetic algorithm," in *2021 46th International Conference on Infrared, Millimeter and Terahertz Waves (IRMMW-THz)*, 2021. doi: 10.1109/IRMMW-THz50926.2021.9567102

[9] **X. Liu**, K. Kolpatzeck, L. Häring, J. C. Balzer, and A. Czylwik, "Beam steering for terahertz time-domain spectroscopy using optical ring resonators," in *2021 46th International Conference on Infrared, Millimeter and Terahertz Waves (IRMMW-THz)*, 2021. doi: 10.1109/IRMMW-THz50926.2021.9567221

[10] **X. Liu**, L. Schmitt, J. Lipka, K. Kolpatzeck, J. C. Balzer, M. Hoffmann, and A. Czylwik, "Optimizing the Radiation Pattern of a MEMS-Based Reflectarray Using a Genetic Algorithm for Beam Steering Applications," *2022 47th International Conference on Infrared, Millimeter and Terahertz Waves (IRMMW-THz)*, 2022. doi: 10.1109/IRMMW-THz50927.2022.9895897

Journal publications (co-author)

[11] D. Damyanov, B. Friederich, M. Yahyapour, N. Vieweg, A. Deninger, K. Kolpatzeck, **X. Liu**, A. Czylwik, T. Schultze, I. Willms, and J. C. Balzer, "High resolution lensless terahertz imaging and ranging," *IEEE Access*, vol. 7, pp. 147 704–147 712, 2019. doi: 10.1109/ACCESS.2019.2934582

[12] K. Kolpatzeck, **X. Liu**, K.-H. Tybussek, L. Häring, M. Zander, W. Rehbein, M. Moehrle, A. Czylwik, and J. C. Balzer, "System-theoretical modeling of terahertz time-domain spectroscopy with ultra-high repetition rate mode-locked lasers," *Opt. Express*, vol. 28, pp. 16 935–16 950, May 2020. doi: 10.1364/OE.389632

[13] K. Kolpatzeck, **X. Liu**, L. Häring, J. C. Balzer, and A. Czylwik, "Ultra-high repetition rate terahertz time-domain spectroscopy for micrometer layer thickness measurement," *Sensors*, vol. 21, 2021. doi: 10.3390/s21165389

[14] Y. Zhao, K. Vora, **X. Liu**,G. Bögel, K. Seidl, and J. C. Balzer "Photonic Crystal Resonator in the Millimeter/Terahertz Range as a Thin Film Sensor for Future Biosensor Applications," *Journal of Infrared, Millimeter, and Terahertz Waves*, vol. 43, pp. 426 - 444, doi:10.1007/s10762-022-00859-1

[15] Y. Zhao, J. Buchholz, T. Grenter, **X. Liu**, G. Bögel, K. Seidl, and J. C. Balzer "Sensitive and Robust Millimeter-Wave/Terahertz Photonic Crystal Chip for Biosensing Applications," *IEEE Access*, vol. 10, pp. 92237-92248, 2022, doi: 10.1109/ACCESS.2022.3202537

[16] L. Schmitt, **X. Liu**, P. Schmitt, A. Czylwik and M. Hoffmann, "Large Displacement Actuators With Multi-Point Stability for a MEMS-Driven THz Beam Steering Concept," *Journal of Microelectromechanical Systems*, vol. 32, no. 2, pp. 195-207, April 2023, doi: 10.1109/JMEMS.2023.3236145

Conference publications (co-author)

[17] K. Kolpatzeck, **X. Liu**, L. Häring, and A. Czylwik, "System-theoretical modeling and analysis of phase control in a photonically steered terahertz phased array transmitter," in *2018 First International Workshop on Mobile Terahertz Systems (IWMTS)*, 2018. doi: 10.1109/IWMTS.2018.8454691

[18] K. Kolpatzeck, **X. Liu**, B. Friederich, D. Damyanov, L. Häring, T. Schultze, J. C. Balzer, and A. Czylwik, "Wideband radiation pattern measurement of terahertz antenna-integrated photodiodes by frequency-domain spectroscopy," in *2019 Second International Workshop on Mobile Terahertz Systems (IWMTS)*, 2019. doi: 10.1109/IWMTS.2019.8823782

[19] K. Kolpatzeck, S. Tonder, **X. Liu**, A. Czylwik, and J. C. Balzer, "Characterization and application of a commercially available laser diode in a thz system," in *2019 IEEE MTT-S International Microwave Workshop Series on Advanced Materials and Processes for RF and THz Applications (IMWS-AMP)*, 2019. doi: 10.1109/IMWS-AMP.2019.8880071

[20] K. Kolpatzeck, **X. Liu**, S. Nellen, B. Friederich, D. Damyanov, L. Häring, T. Schultze, B. Globisch, J. C. Balzer, and A. Czylwik, "Wideband radiation pattern simulation and measurement of a photodiode-based continuous-wave thz emitter," in *2019 44th International Conference on Infrared, Millimeter, and Terahertz Waves (IRMMW-THz)*, 2019. doi: 10.1109/IRMMW-THz.2019.8874041

[21] K. Kolpatzeck, M. Dedic, P. Krämer, **X. Liu**, V. Cherniak, K.-H. Tybussek, M. Zander, L. Häring, J. C. Balzer, and A. Czylwik, "Enhancement of terahertz spectra by model-driven spectral shaping of a mode-locked laser diode in a terahertz time-domain spectroscopy system," in *2020 45th International Conference on Infrared, Millimeter, and Terahertz Waves (IRMMW-THz)*, 2020. doi: 10.1109/IRMMW-THz46771.2020.9370728

[22] K. Kolpatzeck, **X. Liu**, K.-H. Tybussek, L. Häring, M. Zander, W. Rehbein, M. Moehrle, A. Czylwik, and J. C. Balzer, "Analytical modeling of terahertz time-domain spectroscopy with monolithic mode-locked laser diodes," in *2020 45th International Conference on Infrared, Millimeter, and Terahertz Waves (IRMMW-THz)*, 2020. doi: 10.1109/IRMMW-THz46771.2020.9370745

[23] K. Kolpatzeck, P. Krämer, **X. Liu**, T. Kubiczek, J. C. Balzer, and A. Czylwik, "Interferometric time synchronization of a terahertz time-domain spectroscopy system driven by a mode-locked laser diode," in *2021 46th International Conference on Infrared, Millimeter and Terahertz Waves (IRMMW-THz)*, 2021. doi: 10.1109/IRMMW-THz50926.2021.9566956

[24] K. Kolpatzeck, D. Damyanov, **X. Liu**, T. Schultze, J. C. Balzer, and A. Czylwik, "Imaging with an ultra-high repetition rate terahertz time-domain spectroscopy system driven by a mode-locked laser diode," in *2021 46th International Conference on Infrared, Millimeter and Terahertz Waves (IRMMW-THz)*, 2021. doi: 10.1109/IRMMW-THz50926.2021.9566909

[25] B. Friederich, K. Kolpatzeck, **X. Liu**, T. Schultze, J. C. Balzer, A. Czylwik, and I. Willms, "Preprocessing for robust estimation of material parameters by continuous wave thz spectroscopy," in *2018 43rd International Conference on Infrared, Millimeter, and Terahertz Waves (IRMMW-THz)*, 2018. doi: 10.1109/IRMMW-THz.2018.8510417

[26] D. Damyanov, B. Friederich, J. Kohl, **X. Liu**, K. Kolpatzeck, T. Schultze, A. Czylwik, J. C. Balzer, and I. Willms, "Super-resolution restoration of low-resolution thz camera images," in *2019 Second International Workshop on Mobile Terahertz Systems (IWMTS)*, 2019. doi: 10.1109/IWMTS.2019.8823667

[27] S. C. Tonder, K. Kolpatzeck, **X. Liu**, S. Rumpza, A. Czylwik, and J. C. Balzer, "A compact thz quasi tds system for mobile scenarios," in *2019 Second International Workshop on Mobile Terahertz Systems (IWMTS)*, 2019. doi: 10.1109/IWMTS.2019.8823786

[28] D. Damyanov, B. Friederich, K. Kolpatzeck, **X. Liu**, M. Yahyapour, N. Vieweg, A. Deninger, T. Schultze, I. Willms, and J. C. Balzer, "High resolution lensless thz imaging with an ultrafast tds system," in *2019 44th International Conference on Infrared, Millimeter, and Terahertz Waves (IRMMW-THz)*, 2019. doi: 10.1109/IRMMW-THz.2019.8873898

[29] B. Friederich, D. Damyanov, J. Kohl, K. Kolpatzeck, **X. Liu**, T. Schultze, A. Czylwik, J. C. Balzer, and I. Willms, "High resolution image processing technique for the detection of metal entrapments based on a terahertz camera," in *2019 44th International Conference on Infrared, Millimeter, and Terahertz Waves (IRMMW-THz)*, 2019. doi: 10.1109/IRMMW-THz.2019.8874437

[30] L. Schmitt, P. Schmitt, **X. Liu**, A. Czylwik, and M. Hoffmann, "Micromechanical Reflect-Array for THz Radar Beam Steering based on a Mechanical D/A Con-

verter and a Mechanical Amplifier," *2020 Third International Workshop on Mobile Terahertz Systems (IWMTS)*, 2020. doi: 10.1109/IWMTS49292.2020.9166235.

[31] D. Damyanov, B. Friederich, K. Kolpatzeck, **X. Liu**, A. Czylwik, T. Schultze, I. Willms, and J. C. Balzer, "A novel approach for lensless high-resolution terahertz imaging (Conference Presentation)," in *Terahertz Photonics*, M. Jarrahi, S. Preu, and D. Turchinovich, Eds., vol. 11348, International Society for Optics and Photonics. SPIE, 2020. doi: 10.1117/12.2554007

[32] D. Damyanov, A. Batra, B. Friederich, K. Kolpatzeck, **X. Liu**, T. Kaiser, T. Schultze, and J. C. Balzer, "High resolution vna thz imaging for large distances," in *2020 45th International Conference on Infrared, Millimeter, and Terahertz Waves (IRMMW-THz)*, 2020. doi: 10.1109/IRMMW-THz46771.2020.9370443

[33] L. Schmitt, **X. Liu**, A. Czylwik, and M. Hoffmann, "Design and Fabrication of MEMS Reflectors for THz Reflect-Arrays," *2021 Fourth International Workshop on Mobile Terahertz Systems (IWMTS)*, 2021. doi: 10.1109/IWMTS51331.2021.9486804.

[34] V. Cherniak, K. Kolpatzeck, **X. Liu**, K. Tybussek, D. Damyanov, T. Schultze, A. Czylwik, and J. C. Balzer, "Compact and inexpensive terahertz system driven by monolithically integrated commercial light sources," in *2021 46th International Conference on Infrared, Millimeter and Terahertz Waves (IRMMW-THz)*, 2021. doi: 10.1109/IRMMW-THz50926.2021.9567637

[35] T. Kubiczek, **X. Liu**, J. C. Balzer, X. Guo, M. Sakaki, Y. Zhao, and N. Benson, "3D Printed Passive Beam-Guiding and Manipulating Devices for the Terahertz Frequency Range," *2022 IEEE 12th International Conference on RFID Technology and Applications (RFID-TA)*, 2022. doi: 10.1109/RFID-TA54958.2022.9923966

[36] Y. Zhao, T. Kubiczek, **X. Liu**, M. Sakaki, N. Benson, and J. C. Balzer, "A 3-D printed Platform for a Photonic Terahertz Spectrometer to Measure a Photonic Crystal Waveguide," *2022 47th International Conference on Infrared, Millimeter and Terahertz Waves (IRMMW-THz)*, 2022. doi: 10.1109/IRMMW-THz50927.2022.9896115

[37] K. Kolpatzeck, P. Krämer, V. Cherniak, T. Kubiczek, **X. Liu**, J. C. Balzer, and A. Czylwik, "Interferometric Correction of Delay Errors in an Ultra-High Repetition Rate Terahertz Time-Domain Spectroscopy System," *2022 47th International*

Conference on Infrared, Millimeter and Terahertz Waves (IRMMW-THz), 2022. doi: 10.1109/IRMMW-THz50927.2022.9895728

APPENDIX

A3

REFERENCES

References

[38] B. B. Hu and M. C. Nuss, "Imaging with terahertz waves," *Opt. Lett.*, vol. 20, no. 16, pp. 1716-1718, 1995. 10.1364/OL.20.001716

[39] W. L. Chan, J. Deibel, and D. M. Mittleman, "Imaging with terahertz radiation," *Reports on Progress in Physics*, vol. 70, no. 8, pp. 1325, 2007. 10.1088/0034-4885/70/8/R02

[40] P. Jepsen, D. Cooke, and M. Koch, "Terahertz spectroscopy and imaging – modern techniques and applications," *Laser & Photonics Reviews*, vol. 5, no. 1, pp. 124–166, 2011. doi: 10.1002/lpor.201000011

[41] D. M. Mittleman, "Twenty years of terahertz imaging [Invited]," *Opt. Express*, vol. 26, no. 8, pp. 9417–9431, 2018. doi: 10.1364/OE.26.009417

[42] I.E. Gordon, L.S. Rothman, R.J. Hargreaves, R. Hashemi, E.V. Karlovets, F.M. Skinner, E.K. Conway, C. Hill, R.V. Kochanov, Y. Tan, P. Wcisło, A.A. Finenko, K. Nelson, P.F. Bernath, M. Birk, V. Boudon, A. Campargue, K.V. Chance, A. Coustenis, B.J. Drouin, J.–M. Flaud, R.R. Gamache, J.T. Hodges, D. Jacquemart, E.J. Mlawer, A.V. Nikitin, V.I. Perevalov, M. Rotger, J. Tennyson, G.C. Toon, H.

Tran, V.G. Tyuterev, E.M. Adkins, A. Baker, A. Barbe, E. Canè, A.G. Császár, A. Dudaryonok, O. Egorov, A.J. Fleisher, H. Fleurbaey, A. Foltynowicz, T. Furtenbacher, J.J. Harrison, J.–M. Hartmann, V.–M. Horneman, X. Huang, T. Karman, J. Karns, S. Kassi, I. Kleiner, V. Kofman, F. Kwabia–Tchana, N.N. Lavrentieva, T.J. Lee, D.A. Long, A.A. Lukashevskaya, O.M. Lyulin, V.Yu. Makhnev, W. Matt, S.T. Massie, M. Melosso, S.N. Mikhailenko, D. Mondelain, H.S.P. Müller, O.V. Naumenko, A. Perrin, O.L. Polyansky, E. Raddaoui,P.L. Raston, Z.D. Reed, M. Rey, C. Richard, R. Tóbiás, I. Sadiek, D.W. Schwenke, E. Starikova, K. Sung, F. Tamassia, S.A. Tashkun, J. Vander Auwera, I.A. Vasilenko, A.A. Vigasin, G.L. Villanueva, B. Vispoel, G. Wagner, A. Yachmenev, and S.N. Yurchenko vol. 277, pp. 107949, 2022. doi: 10.1016/j.jqsrt.2021.107949

[43] D. H. Auston, K. P. Cheung, and P. R. Smith, "Picosecond photoconducting hertzian dipoles," *Applied Physics Letters*, vol. 45, no. 3, pp. 284–286, 1984. doi: 10.1063/1.95174

[44] D. H. Auston and M. C. Nuss, "Electrooptical generation and detection of femtosecond electrical transients," *IEEE Journal of Quantum Electronics*, vol. 24, no. 2, pp. 184-197, Feb. 1988, doi: 10.1109/3.114

[45] M. Naftaly and R. E. Miles, "Terahertz Time-Domain Spectroscopy for Material Characterization," *Proceedings of the IEEE*, vol. 95, no. 8, pp. 1658-1665, 2007, doi: 10.1109/JPROC.2007.898835

[46] I. Pupeza, R. Wilk, M. Koch, 'Highly accurate optical material parameter determination with THz time-domain spectroscopy," *Opt. Express*, vol. 15, no. 7, pp. 4335-4350, 2007, doi: 10.1364/OE.15.004335

[47] M. V. Exter, C. Fattinger, and D. Grischkowsky, "Terahertz time-domain spectroscopy of water vapor," *Opt. Lett.*, vol. 14, no. 20, pp. 1128–1130, 1989. doi: 10.1364/OL.14.001128

[48] H. Harde, N. Katzenellenbogen, and D. Grischkowsky, "Terahertz coherent transients from methyl chloride vapor," *Opt. Soc. Am. B*, vol. 11, no. 6, pp. 1018–1030, 1994. doi: 10.1364/JOSAB.11.001018

[49] R. Damari, O. Weinberg, D. Krotkov, N. Demina, K. Akulov, A. Golombek, T. Schwartz, and S. Fleischer, "Strong coupling of collective intermolecular vi-

brations in organic materials at terahertz frequencies," *Nature Communications*, vol. 10, no. 1, 2019. doi: 10.1038/s41467-019-11130-y

[50] L. Yang, T. Guo, X. Zhang, S. Cao, and X. Ding, "Toxic chemical compound detection by terahertz spectroscopy: a review," *Reviews in Analytical Chemistry*, vol. 37, no. 3, 2018. doi: 10.1515/revac-2017-0021

[51] L. Ho, M. Pepper, and P. Taday "Signatures and fingerprints," *Nature Photonics*, vol. 2, no. 9, pp. 541–543, 2008. doi: 10.1038/nphoton.2008.174

[52] S. R. Murrill, E. L. Jacobs, S. K. Moyer, C. E. Halford, S. T. Griffin, F. C. De Lucia, D. T. Petkie, and C. C. Franck, "Terahertz imaging system performance model for concealed-weapon identificatio," *Appl. Opt.*, vol. 47, no. 9, pp. 1286–1297, 2008. doi: 10.1364/AO.47.001286

[53] F. Rutz, M. Koch, S. Khare, M. Moneke, H. Richter, and U. Ewert, "Terahertz quality control of polymeric products," *International Journal of Infrared and Millimeter Waves*, vol. 27, no. 4, pp. 547–556, 2006. doi: 10.1007/s10762-006-9106-7

[54] F. Ellrich, M. Bauer, N. Schreiner, A. Keil, T. Pfeiffer, J. Klier, S. Weber, J. Jonuscheit, F. Friederich, and D. Molter, "Terahertz Quality Inspection for Automotive and Aviation Industries," *International Journal of Infrared and Millimeter Waves*, vol. 41, no. 4, pp. 470–489, 2020. doi: 10.1007/s10762-019-00639-4

[55] K. Krügener, J. Ornik, L. M. Schneider, A. Jäckel, C. L. Koch-Dandolo, E. Castro-Camus, N. Riedl-Siedow, M. Koch, and W. Vlöl, "Terahertz Inspection of Buildings and Architectural Art," *Applied Sciences*, vol. 10, no. 15, 2020. doi: 10.3390/app10155166

[56] R. Gente and M. Koch, "Monitoring leaf water content with THz and sub-THz waves," *Plant Methods*, vol. 11, no. 1, 2015. doi: 10.1186/s13007-015-0057-7

[57] Y. Liu, H. Liu, M. Tang, J. Huang, W. Liu, J. Dong, X. Chen, W. Fu, Y. Zhang, "The medical application of terahertz technology in non-invasive detection of cells and tissues: opportunities and challenges," *RSC Adv.*, vol. 9, no. 17, 2019. pp. 9354–9363, doi: 10.1039/C8RA10605C

[58] C. Yu, S. Fan, Y. Sun, E. Pickwell-Macpherson, "The potential of terahertz imaging for cancer diagnosis: A review of investigations to date," *Quantitative imag-*

ing in medicine and surgery, vol. 2, no. 1, 2012. pp. 33–45, doi: 10.3978/j.issn.2223-4292.2012.01.04

[59] Z. D. Taylor, R. S. Singh, M. O. Culjat, J. Suen, W. S. Grundfest, H. Lee, and E. Brown, "Reflective terahertz imaging of porcine skin burns," *Optics letters*, vol. 33, 2008. doi: 1258-60. 10.1364/OL.33.001258

[60] G. G. Hernandez-Cardoso, S. C. Rojas-Landeros, M. Alfaro-Gomez, A. I. Hernandez-Serrano, I. Salas-Gutierrez, E. Lemus-Bedolla, A. R. Castillo-Guzman, H. L. Lopez-Lemus, and E. Castro-Camus, "Terahertz imaging for early screening of diabetic foot syndrome: A proof of concept," *Scientific Reports*, vol. 7, no. 1, 2017. doi: https://doi.org/10.1038/srep42124

[61] R. S. Singh, P. Tewari, J. L. Bourges, J. P. Hubschman, D. B. Bennett, Z. D. Taylor, H. Lee, E. R. B, W. S. Grundfest, and M. O. Culjat, "Terahertz sensing of corneal hydration," 2010 Annual International Conference of the IEEE Engineering in Medicine and Biology, Buenos Aires, Argentina, 2010, pp. 3021-3024, doi: 10.1109/IEMBS.2010.5626146.

[62] L. Wu, D. Xu, Y. Wang, B. Liao, Z. Jiang, L. Zhao, Z. Sun, N. Wu, T. Chen, H. Feng, and J. Yao, "Study of in vivo brain glioma in a mouse model using continuous-wave terahertz reflection imaging," *Biomed Opt Express*, vol. 10, no. 8, 2019. pp. 3953-3962, doi: 10.1364/BOE.10.003953

[63] P. H. Siegel, "Terahertz technology in biology and medicine," *IEEE Transactions on Microwave Theory and Techniques*, vol. 52, no. 10, pp. 2438-2447, 2004. doi: 10.1109/TMTT.2004.835916

[64] W. Liu, Y. Liu, J. Huang, G. Huang, Y. Zhang, W. Fu, "Application of terahertz spectroscopy in biomolecule detection," *Frontiers in Laboratory Medicine*, vol. 2, no. 4, 127–133, 2018. pp. doi: 10.1016/j.flm.2019.05.001

[65] A. G. Markelz, D. M. Mittleman, "Perspective on Terahertz Applications in Bioscience and Biotechnology," *ACS Photonics*, vol. 9, no. 4, 2022. pp. 1117–1126, doi: 10.1021/acsphotonics.2c00228

[66] T. S. Rappaport, Y. Xing, O. Kanhere, S. Ju, A. Madanayake, S. Mandal, A. Alkhateeb, and G. C. Trichopoulos "Wireless Communications and Applications Above

100 GHz: Opportunities and Challenges for 6G and Beyond," *IEEE Access*, vol. 7, pp. 78729-78757, 2019, doi: 10.1109/ACCESS.2019.2921522

[67] K. C. Huang and Z. Wang, "Terahertz Terabit Wireless Communication," *IEEE Microwave Magazine*, vol. 12, no. 4, pp. 108-116, June 2011, doi: 10.1109/MMM.2011.940596.

[68] J. Ma, R. Shrestha, J. Adelberg, C. Y. Yeh, Z. Hossain, E. Knightly, J. M. Jornet, D. M. Mittleman "Security and eavesdropping in terahertz wireless links," *Nature*, vol. 563, pp. 89-93, 2018, doi: 10.1038/s41586-018-0609-x

[69] K. Su, L. Moeller, R. B. Barat, and J. F.Federici, "Experimental comparison of terahertz and infrared data signal attenuation in dust clouds," *J. Opt. Soc. Am. A*, vol. 29, no. 11, pp. 2360-2366, 2012, doi: 10.1364/JOSAA.29.002360

[70] D. Headland, Y. Monnai, D. Abbott, C. Fumeaux, and W. Withayachumnankul, "Tutorial: Terahertz beamforming, from concepts to realizations," *APL Photon.*, vol. 3, no. 5, 2018. doi:10.1063/1.5011063

[71] X. J. Fu, F. Yang, C. X. Liu, X. J. Wu, and T. J. Cui, "Terahertz Beam Steering Technologies: From Phased Arrays to Field-Programmable Metasurfaces," *Adv. Opt. Mater.*, vol. 8, no. 3, 2020. doi:10.1002/adom.201900628

[72] Y. Monnai, X. Lu, and K. Sengupta, "Terahertz Beam Steering: from Fundamentals to Applications," *Journal of Infrared, Millimeter, and Terahertz Waves*, vol. 44, no. 3, 2023. doi: 10.1007/s10762-022-00902-1

[73] A. J. Fenn, D. H. Temme, W. P. Delaney, and W. E. Courtney, "The development of phased-array radar technology," *Lincoln Lab. J.*, vol. 12, 2000.

[74] K. Sengupta and A. Hajimiri, "A 0.28 THz Power-Generation and Beam-Steering Array in CMOS Based on Distributed Active Radiators," *IEEE Journal of Solid-State Circuits*, vol. 47, no. 12, pp. 3013-3031, Dec. 2012, doi: 10.1109/JSSC.2012.2217831

[75] Y. Tousi and E. Afshari, "A scalable THz 2D phased array with +17dBm of EIRP at 338GHz in 65nm bulk CMOS," *2014 IEEE International Solid-State Circuits Conference Digest of Technical Papers (ISSCC)*, San Francisco, CA, USA, 2014, pp. 258-259, doi: 10.1109/ISSCC.2014.6757425

[76] K. Sengupta and A. Hajimiri, "Mutual Synchronization for Power Generation and Beam-Steering in CMOS With On-Chip Sense Antennas Near 200 GHz," *IEEE Transactions on Microwave Theory and Techniques*, vol. 63, no. 9, pp. 2867-2876, Sept. 2015, doi: 10.1109/TMTT.2015.2457902

[77] M. Che, Y. Matsuo, H. Kanaya, H. Ito, T. Ishibashi and K. Kato, "Optoelectronic THz-Wave Beam Steering by Arrayed Photomixers With Integrated Antennas," *IEEE Photonics Technology Letters*, vol. 32, no. 16, pp. 979-982, 15 Aug.15, 2020, doi: 10.1109/LPT.2020.3007415

[78] T. Saito and K. Kato, "Novel Terahertz-Wave Beam Steering Method by Photomixing with Chromatic Dispersion of Optical Fibers," *2020 International Topical Meeting on Microwave Photonics (MWP)*, Matsue, Japan, 2020, pp. 245-248, doi: 10.23919/MWP48676.2020.9314593

[79] L. O. Goldstone and A. A. Oliner, "Leaky-wave Antennas-Part I: Rectangular Waveguides," *IRE Trans. Antenna Propagat*, vol. 7, no. 4, pp. 307-319, 1959, doi: 10.1109/TAP.1959.1144702

[80] K. Sarabandi, A. Jam, M. Vahidpour and J. East, "A Novel Frequency Beam-Steering Antenna Array for Submillimeter-Wave Applications," *IEEE Transactions on Terahertz Science and Technology*, vol. 8, no. 6, pp. 654-665, Nov. 2018, doi: 10.1109/TTHZ.2018.2866019

[81] L. Ranzani, D. Kuester, K. J. Vanhille, A. Boryssenko, E. Grossman and Z. Popović, "G-Band Micro-Fabricated Frequency-Steered Arrays With 2°/GHz Beam Steering," *IEEE Transactions on Terahertz Science and Technology*, vol. 3, no. 5, pp. 566-573, Sept. 2013, doi: 10.1109/TTHZ.2013.2271381

[82] A. A. Oliner and D. R. Jackson, "Leaky-wave Antennas," Chap. 11, in J. L. Volakis(ed.), *Antenna Engineering Handbook*, 4th Ed.(New York: McGraw-Hill, 2007)

[83] K. Murano, I. Watanabe, A. Kasamatsu, S. Suzuki, M. Asada, W. Withayachumnankul, T. Tanaka, and Y. Monnai, "Low-Profile Terahertz Radar Based on Broadband Leaky-Wave Beam Steering," *IEEE Transactions on Terahertz Science and Technology*, vol. 7, no. 1, pp. 60-69, Jan. 2017, doi: 10.1109/TTHZ.2016.2624514

[84] P. Lu, T. Haddad, B. Sievert, B. Khani, S. Makhlouf, S. Dülme, J. Estévez, A. Rennings, D. Erni, U. Pfeiffer, and A. Stöhr, "InP-Based THz Beam Steering Leaky-Wave Antenna," *IEEE Transactions on Terahertz Science and Technology*, vol. 11, no. 2, pp. 218-230, March 2021, doi: 10.1109/TTHZ.2020.3039460

[85] K. I. Maki and C. Otani, "Terahertz beam steering and frequency tuning by using the spatial dispersion of ultrafast laser pulses," *Opt. Express* vol. 16, no. 14, pp. 10158-10169, 2008, doi: 10.1364/OE.16.010158

[86] K. Uematsu, K. I. Maki, and C. Otani, "Terahertz beam steering using interference of femtosecond optical pulses," *Opt. Express*, vol. 20, no. 20, pp. 22914-22921, 2012, doi: 10.1364/OE.20.022914

[87] S. F. Busch, B. Scherger, M. Scheller, and M. Koch, "Optically controlled terahertz beam steering and imaging," *Opt. Lett.*, vol. 37, no. 8, 1391-1393, 2012. doi: 10.1364/OL.37.001391

[88] T. P. Steinbusch, H. K. Tyagi, M. C. Schaafsma, G. Georgiou, and J. Gómez Rivas, "Active terahertz beam steering by photo-generated graded index gratings in thin semiconductor films," *Opt. Express* vol. 22, no. 22, pp. 26559-26571, 2014. doi: 10.1364/OE.22.026559

[89] A. Kannegulla, M. I. Shams, L. Liu, L. J. Cheng, "Photo-induced spatial modulation of THz waves: opportunities and limitations." *Optics express*, vol. 23, no. 25, pp. 32098-112, 2015. doi: 10.1364/OE.23.032098

[90] M. Young, "Zone Plates and Their Aberrations," *J. Opt. Soc. Am.*, vol. 62, no. 8, pp. 972-976, 1972. doi: 10.1364/JOSA.62.000972

[91] A. Petosa, S. Thirakoune and A. Ittipiboon, "Reconfigurable Fresnel-Zone-Plate-Shutter Antenna with Beam-Steering Capability," *IEEE Antennas and Propagation Magazine*, vol. 49, no. 5, pp. 42-51, Oct. 2007. doi: 10.1109/MAP.2007.4395294

[92] M. I. B. Shams, Z. Jiang, J. Qayyum, S. Rahman, P. Fay and L. Liu, "A terahertz reconfigurable photo-induced fresnel-zone-plate antenna for dynamic two-dimensional beam steering and forming," *2015 IEEE MTT-S International Microwave Symposium*, Phoenix, AZ, USA, 2015. pp. 1-4, doi: 10.1109/MWSYM.2015.7167052

[93] S. P. Morgan, "General Solution of the Luneberg Lens Problem," *Journal of Applied Physics*, vol. 29, no. 9, pp. 1358–1368, 1958. doi: 10.1063/1.1723441

[94] D. Headland, W. Withayachumnankul, R. Yamada, M. Fujita, and T. Nagatsuma, "Terahertz multi-beam antenna using photonic crystal waveguide and Luneburg lens," *APL Photonics*, vol. 3, no. 12, 2018. doi: 10.1063/1.5060631

[95] K. Sato and Y. Monnai, "Terahertz Beam Steering Based on Trajectory Deflection in Dielectric-Free Luneburg Lens," *IEEE Transactions on Terahertz Science and Technology*, vol. 10, no. 3, pp. 229-236, May 2020. doi: 10.1109/TTHZ.2020.2983915.

[96] D. Berry, R. Malech and W. Kennedy, "The reflectarray antenna," IEEE Transactions on Antennas and Propagation, vol. 11, no. 6, pp. 645-651, November 1963. doi: 10.1109/TAP.1963.1138112

[97] P. Nayeri, F. Yang and A. Z. Elsherbeni, "Beam-Scanning Reflectarray Antennas: A technical overview and state of the art," *IEEE Antennas and Propagation Magazine*, vol. 57, no. 4, pp. 32-47, Aug. 2015. doi: 10.1109/MAP.2015.2453883

[98] T. Niu, W. Withayachumnankul, B. S.-Y. Ung, H. Menekse, M. Bhaskaran, S. Sriram, and C. Fumeaux, "Experimental demonstration of reflectarray antennas at terahertz frequencies," *Opt. Express* vol. 21, no. 3, pp. 2875-2889, 2013. doi: 10.1364/OE.21.002875

[99] T. Niu, W. Withayachumnankul, A. Upadhyay, P. Gutruf, D. Abbott, M. Bhaskaran, S. Sriram, and C. Fumeaux, "Terahertz reflectarray as a polarizing beam splitter," *Opt. Express*, vol. 22, no. 13, pp. 16148-16160, 2014. doi: 10.1364/OE.22.016148

[100] X. You, R. T. Ako, W. Lee, M. Low, M. Bhaskaran, S. Sriram, C. Fumeaux, and W. Withayachumnankul, "Terahertz Reflectarray with Enhanced Bandwidth," *Advanced Optical Materials*, vol. 7, 2019. doi: 10.1002/adom.201900791

[101] D. Headland, T. Niu, E. Carrasco, D. Abbott, S. Sriram, M. Bhaskaran, C. Fumeaux, and W. Withayachumnankul, 'Terahertz Reflectarrays and Nonuniform Metasurfaces," *IEEE Journal of Selected Topics in Quantum Electronics*, vol. 23, 2017. doi: 10.1109/JSTQE.2016.2640452

[102] E. Carrasco and J. Perruisseau-Carrier, "Reflectarray Antenna at Terahertz Using Graphene," *IEEE Antennas and Wireless Propagation Letters*, vol. 12, pp. 253-256, 2013. doi: 10.1109/LAWP.2013.2247557

[103] Z. Chang, B. You, L. -S. Wu, M. Tang, Y. -P. Zhang and J. -F. Mao, "A Reconfigurable Graphene Reflectarray for Generation of Vortex THz Waves," *IEEE Antennas and Wireless Propagation Letters*, vol. 15, pp. 1537-1540, 2016. doi: 10.1109/LAWP.2016.2519545

[104] Y. Monnai, K. Altmann, C. Jansen, H. Hillmer, M. Koch, and H. Shinoda, "Terahertz beam steering and variable focusing using programmable diffraction gratings," *Opt. Express*, vol. 21, no. 2, pp. 2347-2354, 2013. doi: 10.1364/OE.21.002347

[105] F. Hu, W. Wang, and J. Yao, "An electrostatic MEMS spring actuator with large stroke and out-of-plane actuation," *Journal of Micromechanics and Microengineering*, vol. 21, no. 11, 2011. doi: 10.1088/0960-1317/21/11/115029

[106] M. Sakata, Y. Komura, T. Seki, K. Kobayashi, K. Sano and S. Horiike, "Micromachined relay which utilizes single crystal silicon electrostatic actuator," *Technical Digest. IEEE International MEMS 99 Conference. Twelfth IEEE International Conference on Micro Electro Mechanical Systems (Cat. No.99CH36291)*, Orlando, FL, USA, 1999, pp. 21-24, doi: 10.1109/MEMSYS.1999.746745

[107] P. Schmitt and M. Hoffmann, "Engineering a Compliant Mechanical Amplifier for MEMS Sensor Applications," *Journal of Microelectromechanical Systems*, vol. 29, no. 2, pp. 214-227, April 2020. doi: 10.1109/JMEMS.2020.2965260

[108] P. Schmitt and M. Hoffmann, "A force-compensated compliant MEMS-amplifier with electrostatic anti-springs," *Microsystems & Nanoengineering*, vol. 9, no. 1, 2023. doi: 10.1038/s41378-023-00557-5

[109] A. Sheikholeslami and Z. Atlasbaf, "Novel phase distributions for large electronically beam-scanning reflectarrays," *Scientific Reports*, vol. 11, no. 1, p. 21877, Nov 2021. doi: 10.1038/s41598-021-00883-6

[110] K. Deb, A. Pratap, S. Agarwal and T. Meyarivan, "A fast and elitist multiobjective genetic algorithm: NSGA-II," *IEEE Transactions on Evolutionary Computation*, vol. 6, no. 2, pp. 182-197, April 2002, doi: 10.1109/4235.996017